On nonlinear Fourier transform-based fibre-optic communication systems for periodic signals

Morteza Kamalian Kopae

Department of Engineering and Applied Science

Aston University

This dissertation is submitted for the degree of

Doctor of Philosophy

July 2018

©Morteza Kamalian Kopae, 2018

Aston University

On nonlinear Fourier transform-based fibre-optic communication systems for periodic signals

Morteza Kamalian Kopae

Doctor of Philosophy, August 2018

As the demand for information rate grows on a daily basis, new ways of improving the efficiency of fibre-optic communication systems, the backbone of the global data network, are highly anticipated. Nonlinear Fourier transform (NFT) is one of the newly emerged techniques showing promising results in recent studies both in simulation and experiment. Along this path, this method has shown its potential to overcome some difficulties of the fibre-optic communication regarding nonlinear distortions, especially the crosstalk between the user's bands in wavelength division multiplexing (WDM) systems.

NFT-based systems, however, in the conventional, widely considered case of vanishing boundary signals, have exhibited some drawbacks related to the computational complexity and spectral efficiency. Both problems are the direct consequences of large signal duration ensued from the vanishing boundary condition. Considering periodic solutions to the nonlinear Schrödinger equation is among attempts to solve this problem. It helps to decrease the processing window at the receiver and gives full control over the communication-related parameters of the signal. Periodic NFT (PNFT) can also be implemented through fast numerical methods which makes it yet more appealing.

In this thesis, a general framework to implement PNFT in fibre-optic communication systems is proposed. As the most challenging part of such a system, the inverse transformation stage is particularly taken attention to, and a few ways to perform it are put forward. From the simplest signals with analytically known nonlinear spectrum to a complete periodic solution with arbitrary, finite number of degrees of freedom, several system configurations are conferred and evaluated in terms of their performance. Common measures such as bit error rate, quality factor and mutual information are considered in scrutinising the systems. Based on simulation results, we conclude that the PNFT can, in fact, improve the mutual information by overcoming some shortcomings of the vanishing boundary NFT.

Keywords: Optical communications, Nonlinear Fourier transform, Riemann-Hilbert problem, Periodic nonlinear Fourier transform

To Azi

Acknowledgements

I would like to thank my supervisor Professor Sergei Turitsyn for everything.

This work is the result of his encouragement and personal support, insightful discussions, brilliant suggestions and ideas, and in cases, detailed calculations. The environment he has made for me was by no means what I expected and had seen. What I have learnt from him is beyond science and engineering.

I would also like to thank my associate supervisor and friend, Dr Yaroslav Prilepsky. He is involved in all the details of all works in this thesis and more. His constant support and suggestions made this work possible.

I would also want to thank all my friends and colleagues at Aston University and Aston Institute of Photonic Technologies who make studying enjoyable.

Some parts of Chapter 2 and Chapter 4 is done in collaboration with Yaroslav Prilepsky, Dmitry Shepelsky and Anastasiia Vasylchenkova and I am grateful to them.

Table of contents

Nomenclature

Acronyms / Abbreviations

2D	Two-dimensional
ASE	Amplified spontaneous emission
AWGN	Additive white Gaussian noise
B2B	Back-to-back
BER	Bit error rate
DBP	Digital back-propagation
DCT	Discrete cosine transform
DSP	Digital signal processing
EDFA	Erbium-doped fibre amplifier
EVM	Error vector magnitude
FWM	Four-wave mixing
Gbps	Billions of bits per second
GLME	Gelfand-Levitan-Marchenko equation
IM/DD	Intensity modulated/direct detection
ISI	Inter-symbol interference
IST	Inverse scattering transform
KdV	Korteweg-de Vries

LMMSE   Linear minimum mean-square estimator

LO   Local oscillator

MI   Mutual information

NFT   Nonlinear Fourier transform

NIS   Nonlinear inverse synthesis

NLSE   Nonlinear Schrödinger equation

NPDE   nonlinear partial differential equations

NS   Nonlinear spectrum

OFDM   Orthogonal frequency-division multiplexing

OLDE   Ordinary linear differential equation

OPC   Optical phase conjugation

PDF   Probability density function

PDM   Polarisation-division multiplexing

PMD   Polarisation-mode dispersion

QAM   Quadrature amplitude modulation

QPSK   Quadrature Phase Shift Keying

RHP   Riemann-Hilbert problem

SDM   Space-division multiplexing

SMF   Single-mode fibre

SNR   Signal to noise ratio

SPM   Self-phase modulation

WDM   Wavelength-division multiplexed

XPM   Cross-phase modulation

ZSS   Zakharov-Shabat system

PNFT   Periodic nonlinear Fourier transform

List of figures

Chapter 1

Introduction

1.1 Fibre-optic communication

Fibre-optic communication is the backbone of the global communication network. A reliable fibre-optic communication capable of meeting the daily increasing demand for a higher data rate is necessary. Since its early days in the 1970s, and despite its impressive service, once in a while, a new technology supersedes the previous ones, promising better quality and data rates. With each new technology, new opportunities emerge for ideas and plans which were perceived as impossible or far-fetched. In the early years of fibre-optic communication, the fibre loss was a major constraint for data rate and reach. The invention of erbium-doped fibre amplifier (EDFA) [2] to compensate the loss, made it possible to have transpacific optical links at a much reduced cost. Making use of the five available dimensions to multiplex data; time, space, wavelength, polarisation and quadrature, new systems emerged with higher and higher information rate in the 1990s. The wavelength-division multiplexed (WDM) system with intensity modulated/direct detection (IM/DD) configuration equipped with novel codes, dispersion managed links and polarisation-division multiplexing (PDM) [3] could manage to deliver up to 1 Tb/s communication in a laboratory demonstration [1, 4, 5]. The first commercial WDM system with two wavelengths, each at 1.7 Gb/s, was made available in 1989. But a significant improvement in data-rate was only realised when instead of using standard SMF, a dispersion managed link was deployed which rendered a data-rate up to 20 Gb/s. By 1999 commercial systems could carry 40 wavelengths at 10 Gb/s amounting to an overall data-rate of 400 Gb/s.

Although an IM/DD communication system can provide a high data rate [6], the appearance of the coherent receivers can be considered as a great leap to the future of the modern fibre-optic communication. It made it possible to revisit the ways light was treated at the receiver and opened the door to countless solutions to the problems of the fibre coming from
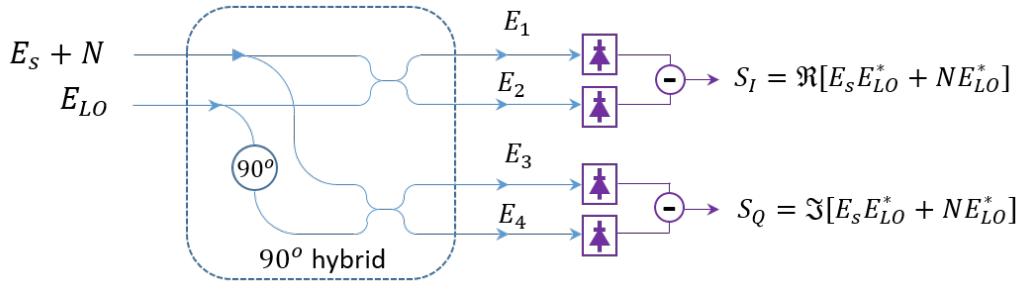
Fig. 1.1 A schematic of a coherent receiver whre E_s is the received signal and N is the additive noise.

other branches of linear communications. Digital coherent receivers combine the benefits of the simplicity of the analogue heterodyne receiver with the small required bandwidth of homodyne receivers. With the use of a local oscillator, the signal is brought down to near baseband. In a coherent communication, both amplitude and phase information of the received signal is used to retrieve the transmitted data. As is shown in Fig. 1.1, the noisy signal is passed through an optical 90-degree hybrid which mixes the signal with a local oscillator (LO). The four optical outputs of the hybrid is then detected by two pairs of balanced photodetectors. The electrical outputs of the square-law detection is then used to find the in-phase and quadrature components of the received signal, see Fig. 1.1 and the signal labels and relations in it. The noise term $N(t)$ is mainly the ASE noise added by the amplifier whose power depends on the type of amplifier. Implementing coherent receivers, quadratic modulation and PDM were enabled. On top of that, now it is possible to use digital signal processing (DSP) to compensate some chromatic dispersion, PMD, nonlinear effects, etc. This new possibility led to the emergence of the first commercial transponder with 100 Gb/s data-rate on a single wavelength [5].

Since the available bandwidth cannot be increased any more due to the amplifier limitations and the low-loss window of fibre, the next step to increase the throughput of the link is to implement space-division multiplexing (SDM) [7]. In an SDM system, parallelism in space is taken to be the solution to increase the fibre utility where different spatial paths are used. These spatial paths can be through different fibres in a bundle, cores in a multi-core fibre or modes in a multi-mode enabled fibre. A superchannel can be made by putting together many spatial channels which combined with the spectral superchannel can provide a hybrid one. This hybrid supperchannel makes a WDM $\times$ SDM matrix in which each cell represents one spatial path at one wavelength transmission. The spatial channel is already available in submarine cables and data centre connections where up to thousands of fibres are deployed in a single cable installation. Of course, integration is one of the most

crucial requirements of modern fibre-optic systems in form of array subsystems such as amplifier arrays, transponder arrays, optical switch arrays, etc. A more compact integration of parallel paths can be achieved through implementing multi-core fibre [8] and few-mode fibres [9]. Spectral superchannels have some benefits such as closer subcarrier spacing in optically routed networks and possibility of nonlinear crosstalk compensation by means of DSP. However, its requirement for accurate tuning of the frequency comb and gain-flattened amplification pose some implementation challenges for such a system. On the other hand, in a spatial superchannel, only a single laser is needed and also it is possible to overcome linear crosstalk ensued from densely integrated paths can be reduced through multiple input-multiple output (MIMO) DSP [5]. The latest research experimental transmission with WDM $\times$ SDM utilised a $6-$mode, $19-$core fibre on C+L bands with the overall 84246 channels which amounts to a 10 Petab/s rate [10]. An essential aspect of the above-mentioned systems is still the array integration of optical components which still seems a big challenge regarding implementation. Available reconfigurable optical add-drop multiplexers (ROADM) are more beneficial in terrestrial networks with spectral superchannels rather than the spatial ones [5].

Using the available cells in the WDM $\times$ SDM matrix, another solution for improving the throughput is to increase the spectral efficiency. This increase entails more sophisticated DSP to overcome some fibre impairments such as chromatic dispersion and various nonlinear distortions. Most of the available DSP techniques which are adopted in the fibre-optic communication are designed for linear channels such as wireless and twisted cooper with Additive white Gaussian noise (AWGN). As opposed to these linear media, increasing signal power does not lead to a larger error-free data rate in an optical fibre communication. This nonlinearity adds to the Amplified spontaneous emission (ASE) an interference proportional to the signal power which dominates the system performance at high signal powers [11, 12]. The main challenge in the fibre-optic communication seems to be the nonlinear signal-noise interaction. Therefore, there has been a great amount of research carried out on mitigating the nonlinear effects of fibre.

The nonlinear interference in fibre can be mainly divided into two categories; signal-noise and signal-signal interaction. Since the signal-signal nonlinear interference is more significant that the signal-noise one, most proposed algorithms are dedicated to overcome this kind of distortion. This interference can be further split into two classes; in-band which is the self-phase modulation (SPM) and out-of-band interference containing cross-phase modulation (XPM) and four-wave mixing (FWM) which are particularly problematic in WDM systems. The master model governing the light propagation in a single-mode fibre is

the nonlinear Schrödinger equation (NLSE):

$$iq_z - \frac{\beta_2}{2}q_{tt} + \gamma|q|^2 q = -\frac{i\alpha}{2}q, \tag{1.1}$$

where q is the slow varying amplitude of the signal envelope, β_2, γ and α are the chromatic dispersion, Kerr nonlinearity and attenuation parameter of the fibre, respectively. This, (1.1), is a valid model for a single mode fibre (SMF) as long as the nonlinearity can be treated as a perturbation and also the signal bandwidth is small enough to ignore higher order linear dispersions and nonlinear effects such as Raman scattering [13]. The chromatic dispersion with parameter β acts as a linear filter when nonlinearity is negligible. Assume Eq. (1.1) with $\alpha = 0$ and $\gamma = 0$, i.e. only with chromatic dispersion:

$$iq_z = \frac{\beta_2}{2}q_{tt}. \tag{1.2}$$

Taking a Fourier transform from both side yields:

$$Q_z(\omega,z) = i\omega^2 \frac{\beta_2}{2}Q(\omega,z) \quad \rightarrow \quad Q(\omega,z) = Q(\omega,0)e^{i\omega^2 \frac{\beta_2}{2}z}, \tag{1.3}$$

where $Q(\omega,z)$ is the Fourier transform of $q(t,z)$ with respect to t and the boundary condition $Q(\omega,0)$. This solution shows that chromatic dispersion changes the spectral components of the signal depending on the frequency and distance and acts like an all-pass filter with the impulse response of $H(\omega) = e^{i\omega^2 \frac{\beta_2}{2}z}$. This effect can be compensated at the receiver by passing the signal through a filter with an inverse impulse response $H_c(\omega) = H^{-1}(\omega)$. The Kerr nonlinearity (or the instantaneous nonlinearity) is a reflection of the nonlinear dependence of the susceptibility tensor of the fibre to the incident electromagnetic field. This nonlinear (mainly third order) susceptibility leads to an induced polarisation, nonlinear with the electromagnetic field which shows itself in an intensity-dependent refractive index, $n(\omega) = n_0(\omega) + n_2|q|^2$, where n_0 is the linear term and n_2 is the nonlinear index coefficient [13]. To see the impact of the Kerr nonlinearity on the signal, let us ignore loss and dispersion terms to arrive at:

$$q_z = i\gamma|q|^2 q. \tag{1.4}$$

The invariance of power implies that the signal phase is the only parameter to change as

$$\phi(z) = \phi(0) - \gamma|q(0)|^2 z, \tag{1.5}$$

where the signal power-dependent phase change is called the SPM. The time-dependent nature of this phase also leads to a frequency shift and spectral broadening. While SPM is

an in-band interference, the term XPM is referred to the interference from any other field with different characteristics which make it out-of-band such as polarisation, wavelength, or direction. Assume a field with two frequency components ω_1 and ω_2:

$$q = q_1 e^{-i\omega_1 t} + q_2 e^{-i\omega_2 t} + \{\text{complex conjugate term}\}. \tag{1.6}$$

The phase shift induced at the field with frequency ω_1 is

$$\Delta\phi = \frac{2\pi}{\lambda} n_2 z \left(|q_1|^2 + 2|q_2|^2 \right), \tag{1.7}$$

where λ is the wavelength and the second term in the RHS of Eq. (1.7) is called the XPM. This effect is twice as large as the SPM and is responsible for the asymmetric spectral broadening of the signal. Another important nonlinear interference is the FWM. In a quantum mechanic framework, the FWM can be explained as the annihilation of one or two photons and creation of new ones with the energy and momentum conserved. Different configurations are possible when three photons transfer they energy into a new one or when two photons give rise to two other ones with different frequencies. For FWM to take place a phase match condition between these fields should be met which is not always easy to satisfy. FWM and XPM are of great influence in wideband communication such as WDM where different channel on different parts of the spectrum can carry other users data. While SPM can partly or entirely eliminate with some DSP algorithms at the receiver, it is often difficult to mitigate the distortion caused by FWM and XPM [14].

One of the most widely suggested methods of dealing with the nonlinear interference of fibre is the digital back-propagation (DBP) [14]. DBP can be implemented at the transmitter or receiver and can numerically take place by means of split-step method or on a perturbation base approach in the time domain [13, 15]. The split-step approach in particular is studied extensively and experimental demonstrations have shown its potential[14]. In this approach, the received signal is taken as the boundary condition of a NLSE with the same dispersion and nonlinear parameters as the fibre but with the opposite signs. This NLSE is then solved numerically to find the back-propagated signal. An important limit to the performance of a DBP system is the signal-noise interaction. In a perturbation framework in which an approximate time-domain solution of the NLSE with a Gaussian signal as the boundary condition is calculated, one can study the impact of different fibre parameters on the signal. Assuming an equal average transmission power across all frequency channels and with a first-order perturbation analysis, the received SNR after one span can be read as [16]

$$SNR_{DBP} = \frac{P}{P_{ASE} + P^3 P_S + P^2 P_{S-ASE}}, \tag{1.8}$$
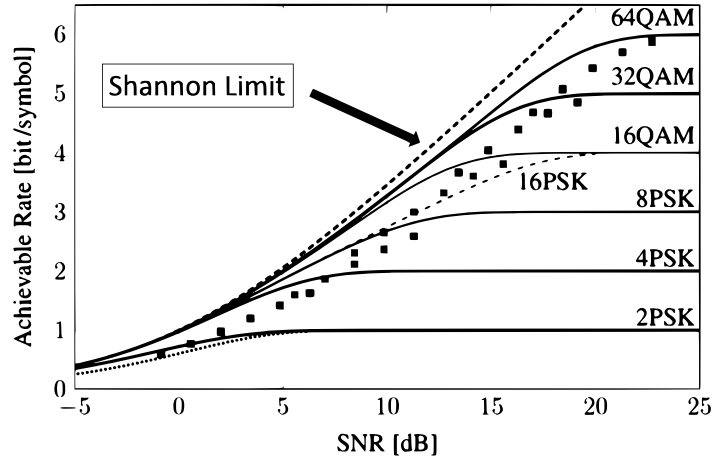
Fig. 1.2 Theoretically achievable data rate in an AWGN channel and a comparison between different modulation formats in a nonlinear medium against SNR [1].

where P is the signal power in the channel of interest, P_{ASE} is the accumulated ASE noise power. In Eq. (1.8), P_S is the residual signal-signal nonlinear interference power as a function of the signal bandwidth and the number of channels considered in the back-propagation calculations, and P_{S-ASE} is the signal-noise interaction nonlinear factor. The effective SNR at the receiver (1.8) can explain the achievable information rate in fibre communication in compared to the Shannon limit for linear channels, see Fig. 1.2. In this figure, the analytical Shannon limit for a linear communication can only be approached in low SNR. As the signal power increases, the impact of the nonlinear effects such as the residual signal-signal nonlinear interference (P_s) or signal noise nonlinear interaction (P_{S-ASE}) dominates the noise and limits the achievable data rate [1, 12].

In Eq. (1.8), the exact dependency of P_s on system parameters vary based on the adopted model. The GN model, in which the signal is treated as a Gaussian noise [17], can provide a closed-form expression for P_s but other models considering the modulation format can predict the performance more accurately. DBP can only reduce P_S and leaves the other terms intact [14, 16]. In a noiseless link, DBP can mitigate all the linear and nonlinear fibre impacts, however, particularly in a wideband system such as WDM, it is required to have the whole signal as the input. That means, processing a huge number of samples in a multi-channel communication system which leads to a considerable computational complexity. This implies considering only a few channels in a sub-optimum settings. It has been shown that the gain can significantly improve by increasing the number of back-propagated channels. For example, in [16] is reported that while back-propagating a single channel in a 31×32 Gbaud 16QAM system over a 40×80 km link delivers a maximum performance of 13 dB SNR, a 31 channel DBP can achieve a 20 dB SNR.

Despite these limitations, DBP is still one of the most widely used approach in eliminating the nonlinear impacts of the fibre, a 2.4 dB improvement in the system Q-factor in a 0.5 Tb/s transmission over a 2890 link is of the bests experimentally demonstrated results of this method [18]. Another nonlinear compensation method is the optical phase conjugation (OPC) where the back-propagation is carried out by means of conjugating the signal and sending it into a similar fibre link. This method also suffers from the interference coming ensued by the signal-noise interaction but, as opposed to the DBP, is implemented in the optical domain, therefore there is no bandwidth and computational complexity limitations. OPC can significantly improve the system performance especially is a multiple OPC configuration [19], although with a smaller compensation efficiency. Although a symmetric link is one of the requirements of an effective OPC system, it has been shown that much improvement can be achieved, for example, an enhancement of 24% for a WDM system with a 8×112 Gb/s signal in a link with discrete amplification is reported in [19]. Also, a 5.3 dB improvement in the system Q-factor is experimentally demonstrated in a 0.8 Tb/s transmission over a 2000 link using 12 OPCs [20].

Another nonlinear compensation scheme is to use a Volterra series model for the fibre and invert its effects. In this model, the NLSE is solved in the frequency domain in which a set of nonlinear transfer functions represent the evolution of signal in fibre. By estimating these nonlinear functions, one can reduce the nonlinear impacts up to a decided order of the transfer functions. It is shown that in a low sampling frequency regime, a 3rd order Volterra nonlinear compensator can outperform a split-step DBP one. The high computational complexity of a Volterra series-based nonlinear compensation scheme is its major drawback [16, 21].

Combined with other novel DSP algorithms such as advanced modulation and coding schemes, nonlinear compensation can provide high information rates in transoceanic links. A 70.4 Tb/s transmission over 7600 km in a wideband system is an example of a recent high speed system [22].

As projected by considering the ever-increasing demand and the pace at which new technology is emerging, there is a capacity crunch in sight where the installed fibres are used at capacity [23]. There are a few routes to increase the information rate all with their limits, one of which is to increase the spectral efficiency of the communication systems. New algorithms and settings to increase the efficiency of the channel make small steps towards the right direction to avoid the crunch as much as possible. Using nonlinear Fourier transform is an attempt along this direction in which the fibre is considered with a new insight. In this view, linear and nonlinear distortions are not detrimental impacts of the channel but some characteristics of the medium which can be used. The idea is not new; it was around in the form of soliton communication. A soliton is a waveform which retains or periodically

recovers its shape as it propagates through the fibre due to a balance between the chromatic dispersion and Kerr nonlinearity (or any other nonlinear phenomenon for that matter).

In general, in a communication system, there is a library of signals, from which one is drawn according to the random data to be transmitted. The selected signal is then sent to the channel and reaches the receiver where the same look-up table is used to recognise the transmitted random data. In a high capacity communication system, the size of this library is large, therefore, this process of choosing signals and checking the look-up table is usually replaced by parametrising a general signal with a set of parameters. This set of parameters will be modulated by the random data and the resulting signal is sent to the channel. In a fibre-optic communication, this general signal needs to be a solution to the NLSE. A solution to the NLSE is a two-dimensional function dependent on two free variables t and z. Any cross-section (i.e $z = constant$) of this solution which is a function of time, t, uniquely determines this solution. So, at the receiver, when the signal is received (hence, one cross-section of the solution to the NLSE is known), the drawn solution from the above-mentioned library of solutions is recognised and the random data is retrieved. In order to recognise the solution to the NLSE from one cross-section (a boundary condition), one needs to solve the NLSE which is a difficult task. This is where a soliton can be useful.

What is special about solitons? A soliton is a known solution to the NLSE, Eq. (1.1) with a trivial dependence to z. This means, it is easy to know any cross-section of this two-dimensional solution at a fixed distance z as a function of time, t. If one knows the value of a cross-section at a distance z, given this trivial evolution along z, it is possible to find any cross-section at any other distance. If it is known that the transmitted signal is a soliton, there are a few parameters to check at the receiver to fully determine the signal. For a fundamental soliton there is one parameter, for higher order solitons there are more. In this way, the communication is actually turned into a system in which these parameters carry the random data from the transmitter to receiver; at the transmitter, the set of parameters are modulated by the random data and the solution to the NLSE with these particular values for the parameters is made. At the receiver, using the signal, the values of the parameters is calculated and the random data is understood. Since the received signal is a cross-section of the solution at an arbitrary distance, it is helpful if the dependence of this set of parameters to z is trivial.

The main issue with this communication scheme is to come up with a set of parameters with trivial evolution in z which uniquely determine a general solution to the NLSE. Nonlinear Fourier transform (NFT) is a tool which projects a solution of the NLSE to a set of such parameters, called *nonlinear spectrum* (NS). This representation for a solution of the NLSE makes a one-to-one relation between the NS and the signal which can be used to solve the

NLSE. Working with the solution of the NLSE means that the communication system is particularly designed for the channel in use which is the fibre. This is the main advantage of a communication system based on NFT. As opposed to other systems in which the nonlinearity is avoided by means of various sub-optimum methods, in an NFT-based system, the fibre channel is considered with its nonlinear characteristic. On top of that, the evolution of the NS as the signal propagates through the fibre is linear which turns the nonlinear channel into a familiar, linear one. In this linear channel, it is possible to have "nonlinear frequency" division multiplexing which unlike the original signal in the time domain, does not encounter cross-talk [24]. This absence of cross-talk in the multiplexing space leads to better performance compared with conventional multiplexing systems such as WDM [25].

As long as the NLSE is a suitable model for the fibre (or any other integrable partial differential equation for that matter), NFT helps to design the communication system matching the characteristics and traits of the medium. Basically, NFT decomposes the solution of the NLSE into the invariant (solitonic) and dynamic (dispersive) components. No matter what the fibre parameters are, there are elements of the signal for which the fibre distortions balance each other out leading to a persistent waveform. Other elements, although changing as propagate through the fibre, have some hidden linearity. This linearity shows itself in the NS, see Fig. 1.3. This gives rise to another potential advantage of an NFT-based system which is its tolerance to one of the most limiting characteristics of fibre; Kerr nonlinearity. As the signal power increases, the system performance is expected to improve for the effective SNR increases. But the nonlinear effects of fibre as shown in Eq. (1.8) start to dominate the ASE noise to the extent that adding more power has a detrimental effect. On the other hand, nonlinearity in an integrable system is merely another characteristic of the dynamics of that system which, in theory, does not influence the quality of the signal in the nonlinear Fourier domain. These potentials need to be investigated through simulations and experimental demonstrations.

The process of going from the time domain to the nonlinear Fourier domain, i.e. calculating the NS is called the *direct transform* and the one taking the NS from the nonlinear Fourier domain back to the time domain is called the *inverse transform*.

A soliton communication is a simple case of a system based on NFT in which the set of parameters, i.e the NS, only consists of a few invariant complex numbers. In its original form, a soliton is susceptible to the fibre loss or any other effect that distorts this balance. However, the concept of a guiding centre soliton, which instead of being a solution to the NLSE is a solution to an average model of it, can rectify this problem to a great extent [26]. Soliton communication suffers from some challenges such as timing jitter and Gordon-Haus effect, and soliton interactions. These challenges make the spectral efficiency of the system
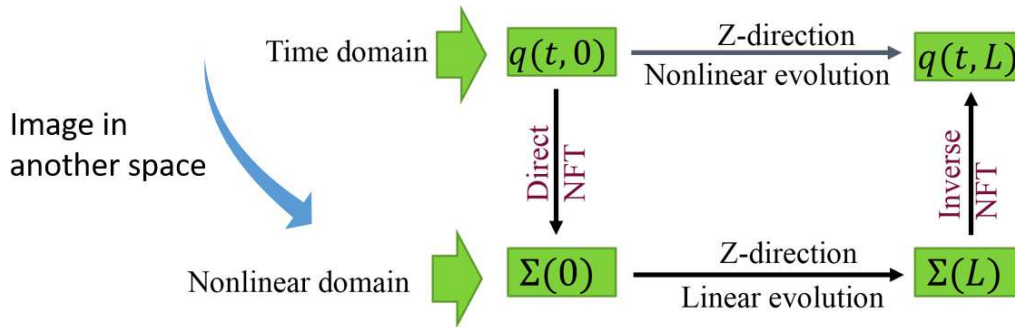
Fig. 1.3 A schematic of the NFT. The nonlinear signal evolution in the time domain is mapped into a linear evolution of the nonlinear spectrum in the nonlinear Fourier domain.

quite limited [26, 27]. A more general NFT, on the other hand, takes full advantage of the physics behind the NLSE and the nonlinear dynamics of light in the fibre.

The basics of NFT is as follows. For integrable nonlinear partial differential equations (NPDE) such as the NLSE, there is an associate ordinary linear differential equation (OLDE) with the solution to the NPDE playing the role of potential. The interesting bit is where the spectrum of the OLDE shows some invariance (or linear evolution) as its potential, i.e. the solution to the NPDE, evolves. This means that, while the evolution of a solution to the NPDE involves complicated, nonlinear dynamics, the spectrum of the associate OLDE has a linear behaviour, more details in Chapter 2 and [28].

Of course, NFT is not the only approach to solve the NLSE. There are several ways to numerically solve the NLSE among which the most widely used are the split-step Fourier and finite element methods [13]. There are also several models for the fibre each with their merits and constraints. These models usually contain some approximations for the nonlinear impacts of the fibre [11, 29]. The numerical approximation is inevitable but a realistic model with discrete components is computationally expensive and in all cases ignores some effects.

To be the solution to the capacity crunch, NFT needs to provide better spectral efficiency. Compared to the best, even commercial fibre-optic communication systems, NFT still has a long way to go. However, recent progress and experimentally demonstrated capabilities and potential of an NFT-based system, put NFT among the promising ideas for the future fibre-optic communication [30].

In solving the NLSE through the NFT in communication applications, the signal is usually assumed to decay fast as time grows. Most of the studies on NFT-based communication revolve around this assumption which although show promising performance, portray some inherent limitations. To satisfy the fast decay criteria, the signal length is usually large which leads to high computational complexity and small spectral efficiency. In this thesis, we argue that using periodic signals can help resolve some of these problems. Periodic signals

have been investigated in the concept of IST for years now [31, 32]. It has been suggested that periodic signals can describe better the dynamics of some nonlinear systems such as in multi-mode fibres [33], deep-water gravity waves [34], etc. Applications of periodic signals in predicting oceanic rogue wave [35–37] and also optical nonlinear media [38] have been explored. As will be shown in the following chapters, particularly in fibre-optic communication application, using periodic signals is beneficial in terms of the computational complexity of the transmitter and the size of the processing window at the receiver.

1.2 Contributions of the thesis

For several years now, the conventional NFT-based communication system is a system where the NS of a signal with vanishing boundary condition is modulated. Although there are some promising results, both in numerical simulations and experimental demonstrations, showing the NFT's potential as a framework to transfer data, we argue that using periodic signals has some advantages. In this thesis, for the first time in the fibre-optic community, we propose a mathematical paradigm in which a periodic signal can be constructed from a NS suitable for a fibre-optic communication. The requirements of a communication system is having control over the signal duration, its power and having enough degrees of freedom to transfer data.

The mathematics of constructing a periodic signal is in general more complicated and demanding than the one for vanishing boundary signals, therefore, a step-by-step approach to performing the inverse transformation is provided. The computational complexity of two main algorithms to carry out the inverse transformation is discussed and compared for the first time. Simulation results of the proposed communication systems with exact inverse transformation stages are reported and the achievable mutual information of such systems are shown.

The contribution of this thesis in investigating the potentials of a fibre-optic communication system based on the PNFT can be summarised as follows:

- The mathematical foundation of the inverse transformation for a finite-gap solution to the NLSE in an Algebro-geometric approach is explained in a detailed and step-by-step manner,

- Several solutions to construct a periodic signal from a given main spectrum to replace the inverse transformation stage is proposed. At first, a simple system made up by a signal with analytically known NS is suggested. This system provides only a one-dimensional constellation, and thus, has somewhat limited performance. Further, this system is developed into a more advanced case when a two-dimensional constellation is

available. This system involves a perturbation of a plane wave and renders one complex degree of freedom for modulation. However, it has also revealed some limitations related to the size of the constellation, bandwidth, and signal power,

- A reduced Algebro-geometric approach to construct a periodic signal with one free complex number in its main spectrum to modulate is proposed. This approach leads to a decrease in the computational complexity of the inverse transformation stage by avoiding numerical evaluation of the Riemann theta function. This system delivers a mutual information of $MI = 7.1$ bits/symbol up to 700 km,

- A general Riemann-Hilbert problem-based approach to perform the inverse transformation is adopted to circumvent numerical evaluation of the Riemann theta function. For an example of a 2-cut spectrum, this system delivers a mutual information of $MI = 7.6$ bits/symbol up to 700 km. This method is not only an alternative to the previous reduced Algebro-geometric approach but also can be generalised to signals with a higher order main spectrum,

- Numerical routines of calculating the NS of a periodic signal are compared regarding their accuracy and runtime,

- Simulation results have been carried out to investigate the efficiency and performance of the proposed communication systems and find their achievable mutual information by implementing some known algorithms in linear communication systems.

The following publication are the results of the current research and directly or indirectly relate to different chapters of this thesis:

[MK1]   M. Kamalian, J. Prilepsky, S. Derevyanko, S. Le, and S. Turitsyn. Nonlinear Fourier based spectral filtering. In *Lasers and Electro-Optics (CLEO), Conference on.* IEEE, 2017.

[MK2]   M. Kamalian, J. Prilepsky, S. Derevyanko, S. Le, and S. Turitsyn. Out-of-band nonlinear spectral filtering for nonlinear Fourier inverse synthesis communication. In *Progress in Electromagnetics Research Symposium (PIERS).* IEEE, 2017.

[MK3]   M. Kamalian, A. Vasylchenkova, J. Prilepsky, D. Shepelsky, and S. Turitsyn. Communication system based on periodic nonlinear Fourier transform with exact inverse transformation. In *ECOC 2018; 44nd European Conference on Optical Communication; Proceedings of.* page Tu3A.2, 2018.

[MK4]   M. Kamalian, J. Prilepsky, S. Le, and S. Turitsyn. Optical communication based on the periodic nonlinear Fourier transform signal processing. In *Photonics (ICP), 2016 IEEE 6th International Conference on.* pages 1–3. IEEE, 2016.

[MK5]   M. Kamalian, J. Prilepsky, S. Le, and S. Turitsyn. Periodic nonlinear Fourier transform for fibre-optic communications, part i: theory and numerical methods. In *Optics express,* 24(16):18353–18369, 2016.

[MK6]   M. Kamalian, J. Prilepsky, S. Le, and S. Turitsyn. Spectral efficiency estimation in periodic nonlinear Fourier transform based communication systems. In *Optical Fiber Communications Conference and Exhibition (OFC)*, pages 1–3. IEEE, 2017.

[MK7]   M. Kamalian, J. Prilepsky, S. Le, and S. Turitsyn. Periodic nonlinear Fourier transform for fibre-optic communications, part ii: eigenvalue communication. *Optics express*, 24 (16):18370–18381, 2016.

[MK8]   M. Kamalian, D. Shepelsky, A. Vasylchenkova, J. Prilepsky, and S. Turitsyn. Communication system using periodic nonlinear Fourier transform based on Riemann-Hilbert problem. *ECOC 2018; 44nd European Conference on Optical Communication; Proceedings of*, page Tu3A.3, Rome, 2018.

[MK9]   M. Kamalian, A. Vasylchenkova, D. Shepelsky, J. Prilepsky, and S. Turitsyn. Periodic nonlinear Fourier transform communication solving the Riemann-Hilbert problem. *Accepted to the Journal of Lightwave Technology*, 2018.

[MK10]   M. Kamalian, J. Prilepsky, S. Le, and S. Turitsyn. On the design of NFT-based communication systems with lumped amplification. *Journal of Lightwave Technology*, 35(24):5464–5472, 2017.

[MK11]   M. Kamalian, S. Le, J. Prilepsky, and S. Turitsyn. Statistical analysis of a communication system based on the periodic nonlinear Fourier transform. *Australian Conference on Optical Fibre Technology*, pages ATh1C–4, 2017.

[MK12]   M. Kamalian, S. Le, J. Prilepsky, and S. Turitsyn. Periodic Nonlinear Fourier Transform Based Transmissions with High Order QAM Formats. *ECOC 2016; 42nd European Conference on Optical Communication; Proceedings of*, Dusseldorf, 2016.

[MK13]   M. Kamalian, S. Le, J. Prilepsky, and S. Turitsyn. Periodic nonlinear Fourier transform based optical communication systems in a band-limited regime. *Optical Sensors Conference*, page JTu4A. 34, Vancouver, 2016.

[MK14]   M. Kamalian, S. Le, J. Prilepsky, and S. Turitsyn. Optimal Launch and Detection Points for the NFT-based Communication System with Lumped Amplification. *ECOC 2017; 43nd European Conference on Optical Communication; Proceedings of*, Gothenburg, 2017.

[MK15]   M. Kamalian, J. Prilepsky, S. Derevyanko, S. Le, S. Turitsyn. Energy based transmission optimisation in nonlinear Fourier domain. *CLEO/Europe-EQEC, 2017 Conference on)*, Munich, 2017.

1.3 Organisation of the thesis

This thesis is organised as follows.

- In Chapter 3, a brief introduction to the NFT-based communication is presented. Different proposed systems are mentioned, and a review of what has been achieved in vanishing boundary NFT is given. This chapter also includes a discussion on the capacity analysis of such a system in the literature. Then, we discuss some advantages of the periodic NFT (PNFT) over the vanishing boundary NFT. Having introduced the basics of utilising NFT in communication, we propose a simple system based on the PNFT in which a signal with analytically known NS is used and discuss its drawbacks and limitations. We further this proposed system to a more general one in which a plane wave is perturbed by an appropriate function. This gives rise to a communication system with more degrees of freedom than the previous one. However, the latter system still suffers from inaccuracy in high power/high bandwidth regimes.

  Therefore, a third system is conferred. Since the procedure of constructing a periodic signal, in general, is explained in some length later, we briefly explain how a simple system with enough number of degrees of freedom can be constructed in an algebro-geometric paradigm. We explain that due to some numerical difficulties it is better to modify the calculations and restrict the NS to a particular form, which in turn, puts a cap on the achievable performance.

  We replace the system mentioned above with yet more general system based on solving a Riemann-Hilbert problem (RHP). We explain the system in a few words and leave a full description to the following chapters. Finally, a natural generalisation of this system is also proposed which since we do not present any simulation results for it, it is mentioned briefly and only as a suggestion for future works.

- Chapter 2 presents a general description of the NFT to find a finite-gap solution to the NLSE. We introduce the NS and a standard way to construct finite-gap solutions for the NLSE. As an alternative, we also put forward a numerically more favourable method to construct such a signal, namely, the RHP approach. We explain these two approaches to some details but leave more technical calculations and discussions to the appendices.

  In this chapter also, a quick argument on how to arrive at a vanishing signal from the definitions of a finite-gap analysis is given.

- The two proposed systems of Chapter 2 are scrutinised through some simulations in terms of their quality factor, BER and mutual information for different transmission distance, signal power, constellation sizes, etc. in Chapter 4. The numerical accuracy of the calculations are also shown, and a discussion on the optimum operating points is made.

- The thesis concludes with some discussions and suggested future works in Chapter 5.

- This work contains some essential appendices. Appendix A depicts the steps to reduce the mentioned algebro-geometric approach into a simple one for a particular case of Section 4.2. Appendix B makes a discussion on the computational complexity of evaluating the Riemann theta function. We show that the complexity of the available algorithms to evaluate the Riemann theta function is higher than what is appropriate for the current application; this is the main reason to resort to the RHP approach. Appendix C explains the used Ablowitz-Ladik routine of calculating the NS. Finally, since the claim is that the finite-gap approach is the most general way of looking at the solutions of the NLSE, appendix D illustrates the steps to get a multi-soliton solution to the NLSE from a finite-gap one.

Chapter 2

Nonlinear Fourier transform

The notion of NFT (or in a historical context, IST) is entangled with solitons; signals which retain their shapes as they propagate through a nonlinear medium. It was only until 1960s when an analytical approach to describe solitons was proposed and a method to solve the Korteweg-de Vries (KdV) equation was discovered [39]. This discovery was further generalised to a framework to solve some nonlinear differential equations with very important physical relevance in the seminal work of Lax [40]. This was just a beginning to many nonlinear systems discovered to be solvable by means of the IST. At the heart of the IST is the notion of integrability; defined and investigated from many points of views since the IST was born.

In this chapter, NFT is briefly introduced. The concept of NS and how to calculate it, and also, transition between the time domain and the nonlinear Fourier domain is reviewed. A discussion on the numerical methods to carry out these calculations is also presented.

2.1   Integrable NPDE

So far there is no general way available to solve a nonlinear partial differential equation (NPDE). However, for some particular NPDEs such as KdV, sine-Gordon, and Nonlinear Schrödinger equation (NLSE)., one can find the solutions by means of the inverse IST. For some particular cases, this might even yield the solution in terms of elementary functions. A very interesting aspect of the IST is that it explains the special solutions to such NPDEs, i.e. solitons. However, there is more to IST than only the solitons; it provides a complete transformation from the time-domain into the nonlinear Fourier domain in which the evolution of the image of the solution is linear. This, in fact, is the base on which a communication system can be built.

The IST formalism in a nutshell is as follows; for an integrable NPDE, there is a linear ordinary differential equation LODE (or system of equations) with a spectral parameter, λ, in which, while the solution to the NPDE plays the role of potential, λ is invariant. In fact, the NPDE can be seen as a compatibility condition between two LODEs, called Lax pair (see the following).

2.2 Lax pair for NLSE

Our main attention in this thesis is to the integrable cubic self-focusing nonlinear Schrödinger equation known to govern many important nonlinear phenomena from deep-water gravity waves to light propagation in optical fibres. We consider a normalised NLSE as follows:

$$iq_z + q_{tt} + 2|q|^2 q = 0, \tag{2.1}$$

which is Eq. (1.1) with normalised parameters

$$t \to \frac{t}{T_s}, \quad z \to \frac{z}{Z_s}, \quad q \to \frac{q}{Q_s}, \tag{2.2}$$

where, if the NLSE governs the light propagation in a fibre, one of the parameters, T_s, Q_s, or Z_s are free to choose. If T_s is chosen we have

$$Z_s = \frac{T_s^2}{|\beta_2|}, \quad Q_s = \frac{2\gamma}{Z_s}. \tag{2.3}$$

Therefore, in (2.1), t represents the normalised retarded time and z is the normalised distance in fibre. The fibre parameters are chosen to be $\beta_2 = -20$ ps^2/km, $\alpha = 0.2$ dB/Km, and $\gamma = 1.3$ W^{-1}Km^{-1}. For Eq. (2.1) as the NPDE in Section 2.1, it has been shown that the Lax pair is [41]

$$\Phi_z = V(\lambda, t, z)\Phi, \quad \text{and} \quad \Phi_t = U(\lambda, t, z)\Phi \tag{2.4}$$

where

$$V(\lambda, t, z) = -2i\lambda^2 \sigma_3 + 2zQ + Q^{(0)}, \quad \text{and} \quad U(\lambda, t, z) = Q - i\lambda \sigma_3 \tag{2.5}$$

with

$$Q = \begin{bmatrix} 0 & q(t,z) \\ -q^*(t,z) & 0 \end{bmatrix}, \quad Q^{(0)} = -i\left(Q^2 + Q_t\right)\sigma_3, \quad \sigma_3 = \begin{bmatrix} 1 & 0 \\ 0 & -1 \end{bmatrix}. \tag{2.6}$$
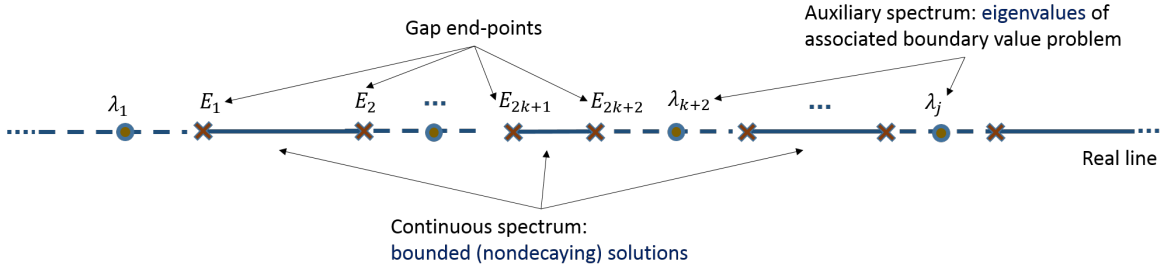
Fig. 2.1 The main spectrum consisting of invariant real numbers E_j and auxiliary spectrum as the dynamic points λ_i of a solution to the KdV equation.

In (2.4), the solution to the NLSE, $q(t,z)$, is a potential. If Φ is a solution to both equations in (2.4) then the compatibility condition, $\Phi_{tz} = \Phi_{zt}$ which is equivalent to the zero-curvature relation, $U_z - V_t + [U,V] = 0$, is only satisfied iff $q(t,z)$ satisfies the NLSE where $[U,V] = UV - VU$ is the matrix commutator. In this case, $\lambda_z = 0$. IST is involved with the spectral analysis of the Dirichlet problem of Eq. (2.4). Since the operator U is a bounded one, its spectrum consists of two parts: places where

- $U - \lambda I$ fails to be invertible, or

- $U - \lambda I$ is not bijective.

Hereafter, the spectrum mentioned above and/or other quantities equivalent to them, which come from the spectral analysis of the operator in Eq. (2.4), are considered to be defined in a domain called the *nonlinear Fourier domain*. Since a vast amount of work has been done in the IST formalism for fast decaying solutions to the NLSE, to understand the concept of IST and definitions of terms, in this section, we sometimes address this kind of signals. The next chapter is entirely dedicated to the IST producing different types of solution.

2.3   Nonlinear spectrum

To understand the concept of the NS of a finite-gap solution, let us start from the KdV equation which historically is of a great importance. For KdV, the auxiliary equation (Lax equation) is the linear Schrödinger equation whose spectrum plays the leading role in an NFT analysis. This spectrum consists of real line with some gaps, see Fig. 2.1. In addition to these gaps, there are some eigenvalues lying in the gaps which move as the signal propagates through the medium. These eigenvalues, collectively called the *auxiliary spectrum*, are considered as the dynamic part of the NS and the invariant end-points of the gaps, called
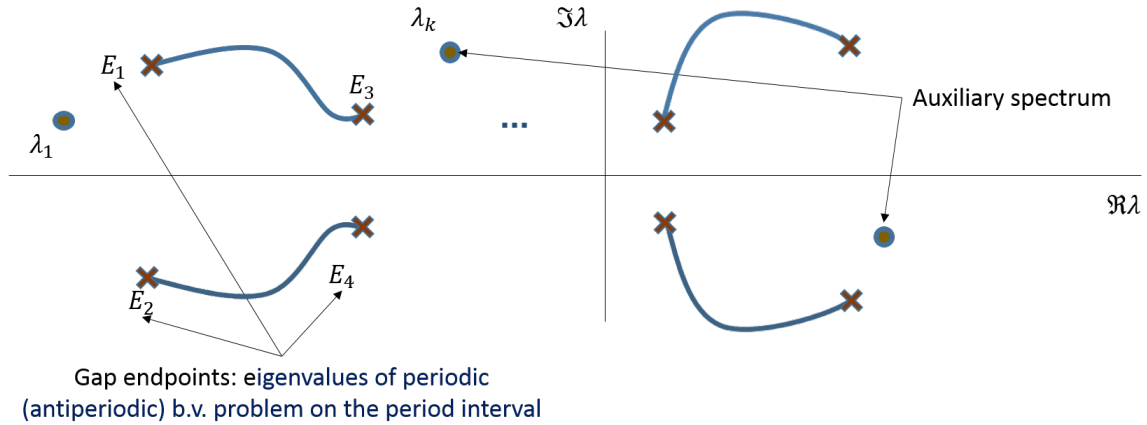
Fig. 2.2 The main spectrum consisting of invariant real numbers E_j and auxiliary spectrum as the dynamic points λ_i of a solution to the NLSE.

main spectrum, are the static part of it. If there is a finite number of these gaps, the associate solution to the KdV is called a finite-gap solution.

For the NLSE on the other hand, the auxiliary equation is the Zakharov-Shabat system of differential equations Eq. (2.4). As opposed to the spectrum of the linear Schrödinger equation, the spectrum of the ZSS can contain complex numbers so the spectrum consists of some curves on the continuous spectrum. Like KdV, here the end-points of these curves are invariant and there are some eigenvalues (the auxiliary spectrum) moving around on the complex plane as the signal evolves along the propagation dimension, see Fig. 2.2. As before, if there is a finite number of these curves, the associate solution to the NLSE is called a finite-gap solution. To make up a finite-gap solution, one needs to start from a set of auxiliary and main spectrum points and construct the solutions to the ZSS, called *Bloch functions*, and use these functions to form a solution.

To see the relation between the NS as a solution, we start by solving the Dirichlet boundary condition problem in (2.4) to find normalised Jost solutions Φ with boundary condition $\Phi^\pm = \Phi^0$ as $t \to \pm\infty$ where $\Phi^0 = e^{-(i\lambda t + 2i\lambda^2 z)\sigma_3}$ is the solution associated to the zero background [42]. From this solution, one can find Q, hence, the solution to the NLSE via $Q = i[\sigma_3, \Phi_1]$, and

$$\Phi^\pm(t,z;\lambda) = \left(\mathbb{I} + \frac{\Phi_1(t,z)}{\lambda} + \cdots\right)\Phi^0(t,z;\lambda), \quad \text{as} \quad t \to \pm\infty. \tag{2.7}$$

Since $\Phi^\pm(t,z;\lambda)$ are bounded at $\lambda \in \mathbb{R}$, the real axis is a part of the spectrum. For other members of the spectrum defined as below:

$$\sigma_c \equiv \{\lambda \in \mathbb{C} | \Phi \text{ is bounded for } \forall t\}, \tag{2.8}$$

$\Phi^{\pm}(t,z;\lambda)$ being independent solutions of the Lax pair, it is possible to form a problem as below

$$\Phi^{-}(t,z;\lambda) = \Phi^{+}(t,z;\lambda)S(\lambda), \quad \lambda \in \sigma_c, \tag{2.9}$$

In this regard, to find a solution to the NLSE given a boundary condition $q(t,0)$, one can calculate $\Phi^{\pm}(t,0;\lambda)$ and find the time and space-independent scattering matrix $S(\lambda)$ from (2.9). For any z, this $S(\lambda)$ can be used, and the associated RHP (2.9) can be solved to find $\Phi^{\pm}(t,z;\lambda)$ from which $q(t,z)$ is retrieved. Hereafter, we assume $q(t,0) = q(t+T,0)$ for some period T. Let solve (2.4) and form the fundamental matrix for a boundary condition [43]:

$$\Phi(t_0,t_0;\lambda) = \begin{bmatrix} 1 & 0 \\ 0 & 1 \end{bmatrix}, \text{ at a base point } t_0. \tag{2.10}$$

This fundamental matrix evaluated at one period after the base point is called the monodromy matrix, $\mathcal{M} = \Phi(t_0,t_0+T;\lambda)$ with $\det\mathcal{M} = 1$ and the trace $\Delta(\lambda) = \text{Tr}\mathcal{M}$, called the discriminant, independent of the base point. In the Floquet theory for the Zakharov-Shabat operator with periodic coefficients, its solution ψ, called the *Bloch function*, is determined as an eigenfunction of the operator of shift by the period [43]:

$$\psi(t+T;\lambda) = m(\lambda)\psi(t;\lambda), \tag{2.11}$$

where $m(\lambda)$ is called the Floquet multiplier. Clearly, ψ is bounded on the whole line for those λ for which $|m(\lambda)| = 1$. On the one hand, being a solution of the ZSS, ψ is a combination of columns of Φ, Φ^1 and Φ^2, at any time:

$$\psi(t_0+T;\lambda) = A \times \Phi^1(t_0,t_0+T;\lambda) + B \times \Phi^2(t_0,t_0+T;\lambda) = \mathcal{M}\begin{bmatrix} A \\ B \end{bmatrix}. \tag{2.12}$$

Combining this with Eq. (2.11), it follows that

$$m(\lambda)\begin{bmatrix} A \\ B \end{bmatrix} = \mathcal{M}\begin{bmatrix} A \\ B \end{bmatrix}, \tag{2.13}$$

i.e., $m(\lambda)$ is an eigenvalue of the monodromy matrix $\mathcal{M}$. Since $\det\mathcal{M} = 1$, $m(\lambda)$ can be expressed in terms of the discriminant $\Delta(\lambda)$:

$$m_{\pm}(\lambda) = \frac{\Delta(\lambda) \pm \sqrt{\Delta^2(\lambda) - 4}}{2}, \tag{2.14}$$
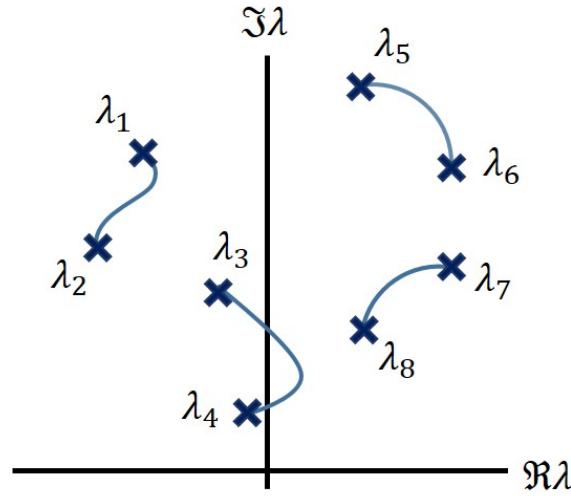
Fig. 2.3 The positive imaginary part of the spectrum of a finite-gap (a 3-gap example here) solution with crosses representing the discrete spectrum connected by curves of continuous spectrum.

from which we can deduce that $\Delta(\lambda) \in \mathbb{R}$ for the solution to be bounded. It follows that the continuous spectrum of the Zakharov-Shabat operator, which is where $|m(\lambda)| = 1$, can be characterized in terms of the discriminant by the inequality $\Delta^2(\lambda) \leq 4$, or $\Delta(\lambda) \in [-2, 2]$. If this is the case, $\psi(t + T; \lambda) = e^{i\mu(\lambda)}\psi(t; \lambda)$, where $\mu \in \mathbb{R}$ is the Floquet exponent. For the end points $\lambda = \lambda_j$ with $\Delta(\lambda_j) = \pm 2$, we have $m(\lambda_j) = 1$ or $m(\lambda_j) = -1$, which, in view of (2.11), correspond to the periodic or anti-periodic solution, respectively. Thus the end points of the spectral arcs (the main spectrum) can be found as the eigenvalues of the periodic or anti-periodic problem posed on the period interval. For the focusing NLSE the main spectrum comes in complex conjugate pairs.

Thanks to the analyticity of $\Delta(\lambda)$, The continuous spectrum, σ_c, consists of two-dimensional curves on the complex plane with endpoints comprising the main spectrum. In this work we consider a finite-gap solution of the NLSE which is a solution with only finitely many of such curves, see Fig. 2.3 [42].

In the light of the above-mentioned definition of the main and auxiliary spectrum, it is possible to rearrange the columns of $\Phi^\pm$ considering their domains of analyticity to arrive at an RHP with $S(\lambda)$ being piece-wise independent of λ on some arcs connecting complex conjugate discrete spectrum points, see Fig. 2.4. The $+$ and $-$ signs in the RHP denote the limit as λ approaches the curve from right and left, respectively.

As mentioned before, constructing a finite-gap solution to the NLSE takes place by starting from finding the spectrum, σ_c of the boundary condition $q(t, 0)$ followed by calculating the $S(\lambda)$ at that point. Changing z and solving the RHP to find the Baker-Akhiezer matrix, Φ,
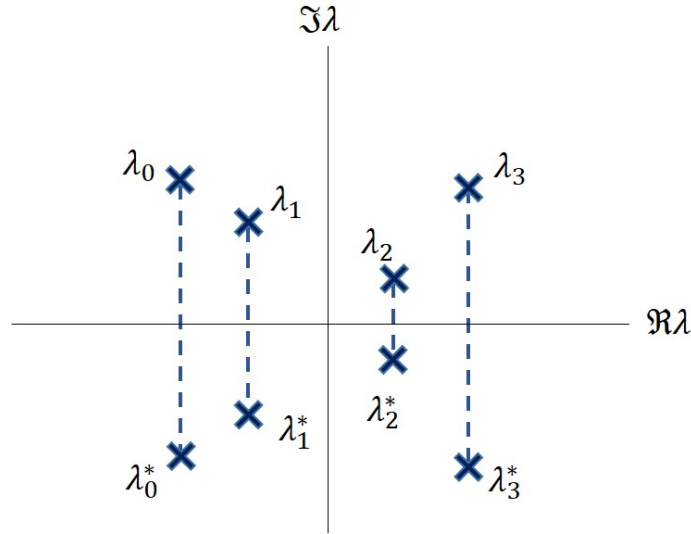
Fig. 2.4 The main spectrum and its cuts after rearranging the elements of the Baker-Akhiezer function to get an RHP with piece-wise constant jumps.

and using it to construct $q(t,z)$ yields a solution to the NLSE in both time and space. Let assume we have found $S(\lambda)$ and the spectrum consisting of $\mathcal{N}+1$ complex conjugate pairs of eigenvalues, $\{\lambda_j, \lambda_j^*\}_{j=0}^{\mathcal{N}}$, with vertical cuts giving shape to, $\Gamma = \cup_{j=0}^{\mathcal{N}} \Gamma_j$. Each Γ_j is a vertical line connecting λ_j and λ_j^*, see Fig 2.4. Here we address two different approaches to find Φ given the spectrum; the standard algebro-geometric and the RHP approach. These two are thoroughly explained in the next chapter.

2.4 Inverse transformation

Inverse transformation is the process of constructing a solution to the NLSE given its NS. In the communication framework, this mean constructing a one-dimensional function as a function of time, at a constant distance which is the location of the transmitter or receiver. That means, while the main spectrum is fixed, the exact value of the auxiliary spectrum needs to be known. The elements of auxiliary spectrum travel all over the complex plane with a complicated dependence to time and distance. Knowing the value of the main and auxiliary spectrum, one can construct the Bloch functions. The nonlinear Schrödinger equation defines the evolution of two complex-valued functions, q and q' [44]:

$$iq_z + q_{tt} - 2|q|^2 q = 0,$$
$$-iq_z' + q_{tt} - 2|q|^2 q' = 0, \tag{2.15}$$

which gives (2.1) where $q' = -q^*$. In such case, another symmetry condition should be realised for the solution of the ZSS, $\Phi(\lambda) = \sigma_2 \bar{\Phi}(\bar{\lambda}) \sigma_2$. The Lax pair for this equation is (2.4). The matrix-valued solution of the Lax equations, Φ, has some important analytical properties mentioned in the following Lemma:

Lemma 2.4.1 *Let* $\Phi(\lambda)$ *be a* 2×2 *matrix function holomorphic in some punctured neighbourhood of infinity on the Riemann sphere, smoothly depending on t and z, with the following asymptotic expansion at infinity:*

$$\Phi(t,z;\lambda) = \left[\mathbb{I} + \sum_{j=1}^{\infty} \Phi_j(t,z)\lambda^{-j} \right] \exp\left(-i\lambda t \sigma_3 - 2i\lambda^2 z \sigma_3 \right) C(\lambda), \tag{2.16}$$

where $C(\lambda)$ *is some invertible matrix. Then, the following holds:*

$$\Phi_t \Phi^{-1} = U(\lambda) + o(\lambda^{-1}), \qquad \Phi_z \Phi^{-1} = V(\lambda) + o(\lambda^{-1}), \quad |\lambda| \to \infty, \tag{2.17}$$

with U and V defined in terms of Φ^j *as*

$$U(\lambda) = -i\lambda\sigma_3 + i[\sigma_3, \Phi_1],$$
$$V(\lambda) = -2i\lambda^2\sigma_3 + 2i\lambda[\sigma_3, \Phi_1] + 2i[\sigma_3, \Phi_2] - 2i[\sigma_3, \Phi_1]\Phi^1, \tag{2.18}$$

with $[\cdot]$ *being the commutator.*

Lemma 2.4.2 *Let* $\Phi(t,z;\lambda)$ *of Lemma 2.4.1 be a solution to the Lax equations (2.4). Then U and V are in the form of (2.5) and the solutions to the Schrödinger system are*

$$q(t,z) = 2(\Phi_1)_{12}, \quad and \quad q'(t,z) = 2(\Phi_1)_{21}. \tag{2.19}$$

The most challenging part of this procedure is to calculate the value of the auxiliary spectrum. However, it is easy to show that they lie on a Riemann surface made up by the main spectrum, hence, fixed [43]. This helps making the calculations simpler.

In this section, two general approaches to construct a finite-gap solution to the NLSE is presented and a discussion on the numerical methods to carry out the calculations is give. The problem is as follows: given a NS of a finite-gap solution to the focusing NLSE, the goal is to construct the signal. For the NLSE, the NS is related to the spectrum of the Zakharov-Shabat operator Eq. (2.4). Therefore, the first step to construct the solution to the NLSE is to find a solution to the Zakharov-Shabat equation, Eq. (2.4). Imposing periodicity as the boundary condition to this equation, the solutions are Bloch functions. A Bloch function can be uniquely determined by means of its poles and behaviour as the spectral parameter, λ

goes to ∞. The poles of the Bloch function, where there is only finitely many of them, are associated to the auxiliary spectrum which is the dynamic part of the NS.

2.4.1   Algebro-geometric approach

Let the matrix-valued function Φ be

$$\Phi(t,z;\lambda) = [\Phi^1\ \Phi^2] = \begin{bmatrix} \Phi_{11} & \Phi_{12} \\ \Phi_{21} & \Phi_{22} \end{bmatrix}. \tag{2.20}$$

with the spectral parameter λ where Φ^1 and Φ^2 are two Bloch eigenfunctions associated to λ satisfying (2.4). We form the periodic squared eigenfunctions as below [43]:

$$f(t,z;\lambda) = -\frac{i}{2}\left(\Phi_{11}\Phi_{22} + \Phi_{21}\Phi_{12}\right),$$

$$g(t,z;\lambda) = \Phi_{11}\Phi_{12},$$

$$h(t,z;\lambda) = -\Phi_{12}\Phi_{22}.$$

Having a finite-gap solution implies that these squared eigenfunctions are finite-order polynomials in λ. Some straightforward calculations yield:

$$f^2 - gh = -\frac{1}{4}W(\Phi^1,\Phi^2)^2 = P(\lambda) = \prod_{j=0}^{\mathcal{N}} \left(\lambda - \lambda_j\right)\left(\lambda - \lambda_j^*\right), \tag{2.21}$$

$$g(t,z;\lambda) = iq(t,z) \times \prod_{j=1}^{\mathcal{N}} \left(\lambda - \mu_j(t,z)\right), \tag{2.22}$$

where $W(\cdot)$ is the Wronskian defined as

$$W(v,u) = \det\begin{pmatrix} v_1 & u_1 \\ v_2 & u_2 \end{pmatrix} = v_1 u_2 - v_2 u_1,$$

and $\mu_j(t,z)$ are called the auxiliary spectrum which represent the evolution of signal as it propagates through the fibre and can be found from the monodromy matrix. To find $\mu_j(t,z)$

at any z and t, one needs to solve a system of differential equations [43]

$$\mu_{jt} = \frac{-2i\kappa_j\sqrt{P(\mu_j)}}{\prod\limits_{l \neq j}(\mu_j - \mu_l)},$$

$$\mu_{jz} = -2\left(\sum_{l \neq j}^{\mathscr{N}}\mu_j - \frac{1}{2}\sum_{j=0}^{\mathscr{N}}(\lambda_j + \lambda_j^*)\right)\mu_{jt}, \quad j = 1, \cdots, \mathscr{N}, \tag{2.23}$$

where μ_{jt} and μ_{jz} are the time and distance derivatives of μ_j, respectively. However, it is easy to show that the auxiliary spectrum lies on a Riemann surface, $\mathscr{X}$, defined by Eq. (2.21) with $\kappa_j \in \{-1, +1\}$ indicating the sheet of the Riemann surface on which μ_j lies. Therefore, instead of solving these complicated interwoven differential equations, one can use an Abel map as a change of variables which maps the auxiliary spectrum from the Riemann surface onto $\mathbb{C}^2$. Let us have a look at the Riemann surface and its properties. Here we briefly note some properties but for a more detailed discussion see Appendix [44].

A hyperelliptic Riemann surface, defined as a subset of $\mathbb{C}^2$, can be made by glueing together two complex planes at the cuts defined by the square root function. The square root function is multi-valued for any non-zero complex number. The branch cut is usually defined as the negative part of the real axis. One can choose different branch cuts, e. g. on the straight lines between the pairs of eigenvalues. When the function under the square root function is $P(\lambda)$ in Eq. (2.21), these cuts can be defined as the straight lines connecting λ_j and λ_j^*. Such rearrangement renders the function

$$\sqrt{P(\lambda)} = w(\lambda) = \sqrt{\prod_{j=0}^{\mathscr{N}}\left(\lambda - \lambda_j\right)\left(\lambda - \lambda_j^*\right)}, \tag{2.24}$$

with the imaginary part as shown in Fig. 2.5 when the branch points are $\{-1+i, -1-i, 2i, -2i, 1+0.5i, 1-0.5i\}$ as an example.

Every compact Riemann surface is holomorphic to a sphere with handles, where the number of handles, $\mathscr{N}$, is called the *genus*. We refer to λ as *points* and as independent variables and (λ, w) as a *place* on the Riemann surface. For each regular point, there are two associated places. Such Riemann surface becomes compact by adding ∞ to it. From now on, to illustrate a Riemann surface we use this presentation an example of which is depicted for a 3-genus surface in Fig. 2.6. The auxiliary points of (2.23) travel on the Riemann surface made by the discrete spectrum [45]. The goal is to, starting from the initial values $\mu_j(t, 0)$ obtained from the monodromy matrix, solve Eqs. (2.23) and find $\mu_j(t, z)$. Integrating over some paths on $\mathscr{X}$ can be simplified by forming a basis for closed paths and a basis
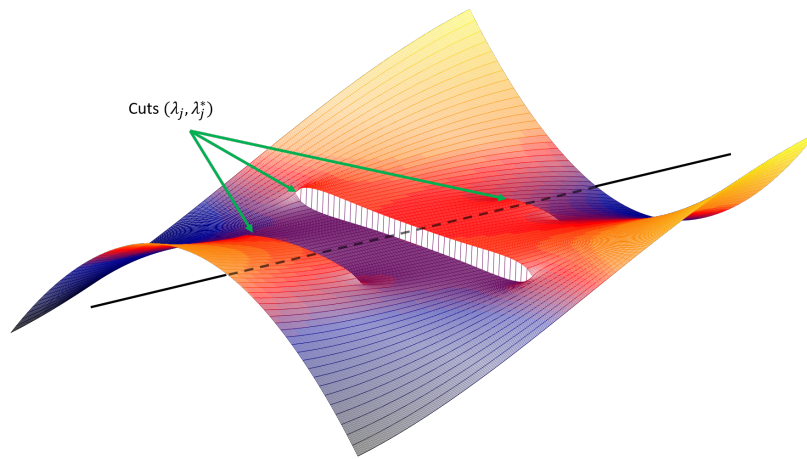
Fig. 2.5 The imaginary part of $\sqrt{P(\lambda)}$ in (2.24).
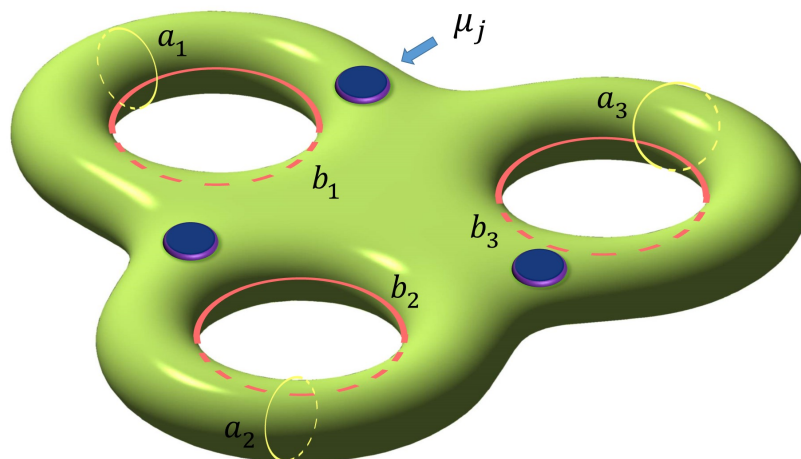
Fig. 2.6 A Riemann surface of genus 3 with three points of auxiliary spectrum.

for differentials on this surface and found the calculations on them. One can investigate these differential equations by considering them as a combination of some independent holomorphic differentials, $\omega_1, \omega_2, \cdots, \omega_{\mathcal{N}}$. To define these differentials properly, we start by a set of non-normalised ones defined as:

$$\tilde{\omega}_j = \frac{\sum\limits_{n+m\leq d+3} c_{n,m} w^n \lambda^m}{F(w)} d\lambda. \tag{2.25}$$

On $\mathscr{X}$, there are also two sets of topologically distinct cycles, a_j cycles and b_j cycles with orientation, see Fig. 2.6. Any closed path over $\mathscr{X}$ can be made using these cycles. A *path* on a Riemann surface is called closed if the start and end points are the same. If such path bounds a part of $\mathscr{X}$, it can be contracted to zero, i.e., it is trivial regarding the integration of analytic functions. A *cycle* is a path which is not contractable to zero. For a genus-$\mathcal{N}$ surface, there is a basis for its first homology consisting of *a*-cycles and *b*-cycles where: 1) *a*-cycles do not cross each other and *b*-cycles do not cross each other, 2) a_j and b_j only intersect once, 3) none of the members of this basis can be continuously deformed into another, see Fig. 2.6 for an example.

From the non-normalised basis of Eq. (2.25), the normalised one, $(\omega_1, \omega_2, \cdots, \omega_{\mathcal{N}})$, called the basis for the cohomology of $\mathscr{X}$, can be obtained considering

$$\oint_{a_l} \omega_j = \delta_{lj}. \tag{2.26}$$

This basis is used to integrate Eqs. (2.23). These definitions of cycles and differential basis is useful for we can decompose differentials over any path over $\mathscr{X}$ into a combination of *a*-cycles and *b*-cycles using this basis. Since all closed integral paths can be considered as a combination of the a-cycles and b-cycles, it is useful to find the integral of the basis for the cohomology on some of these cycles. The Riemann matrix, B is defined as below

$$\mathsf{B} = \left(\mathsf{B}_{lj}\right)_{l,j=1}^{\mathcal{N}}, \quad \mathsf{B}_{lj} = \oint_{b_l} \omega_j. \tag{2.27}$$

Taking into account the integration over a-cycles, the *period* matrix, containing all the information needed about integrating over closed paths is

$$\mathsf{P} = [\mathbb{I}\,\mathsf{B}],$$

where $\mathbb{I}$ is the identity matrix. The columns of P, being linearly independent, form a lattice [46]

$$\Lambda = \{A : A = \mathbb{I}V + \mathsf{B}U; V, U \in \mathbb{C}^{\mathcal{N}}\}.$$

In this way, two vectors are the same if their difference is on this lattice. Therefore, the quotient space $\mathbb{C}/\Lambda$, known as the *Jacobian* of $\mathscr{X}$ is of main importance.

Let take the points in the auxiliary spectrum as some places on the Riemann surface, $P_1, P_2, \cdots, P_{\mathscr{N}}$. With this set of points and their multiplicity, define the *divisor*, $\mathscr{D}$, as:

$$\mathscr{D} = \sum_j p_j P_j,$$

where p_j is the multiplicity of the place P_j. While the motion of the auxiliary spectrum on $\mathscr{X}$ is very complicated, there is a change of variable in a form of an Abel map which turns this evolution into a simple, linear one. The Abel map of a place, P, is defined from $\mathscr{X}$ to its Jacobian as

$$\mathbf{A}(P) = (A_1, A_2, \cdots, A_{\mathscr{N}}) = \left(\int_{P_0}^{P} \omega_1, \int_{P_0}^{P} \omega_2, \cdots, \int_{P_0}^{P} \omega_{\mathscr{N}} \right) = \int_{P_0}^{P} \omega$$

where P_0 is a base point and $\omega = [\omega_1, \cdots, \omega_{\mathscr{N}}]^T$. The Abel map of a divisor also is defined as

$$\mathbf{A}(P_0, \mathscr{D}) = \sum_j p_j \mathbf{A}(P_0, P_j).$$

It is easy to show that the Abel map of the relevant divisor, $\mathscr{D} = \sum P_j$, has linear evolution in t and z in the form [43]

$$\mathbf{A}(P_0, \mathscr{D}) = \mathbf{V}t + \mathbf{U}z + \phi, \tag{2.28}$$

where vectors $\mathbf{V}$ and $\mathbf{U}$ will be defined and vector ϕ is arbitrary (determined by $q(t,0)$). Therefore, instead of solving the complicated equations (2.23), we can find $\mathbf{V}$ and $\mathbf{U}$ (more on this later). Following these lines, changing z, the Abel map of the auxiliary spectrum can be easily found using (2.28). This mapping should be inverted in order to find the auxiliary spectrum.

A meromorphic function f on $\mathscr{X}$ whose zeros, $P_1, \cdots, P_s$, and poles, $Q_1, \cdots, Q_s$, have multiplicities $p_1, \cdots, p_s$ and $q_1, \cdots, q_s$, respectively, defines a *valuation* divisor:

$$(f)_{val} = \sum_j p_j P_j - \sum_j q_j Q_j,$$

which can be considered as the division of two, ω and ω', Abelian differentials. Therefore, ω/ω' is a meromorphic function. This will be used later to invert the Abel map. This means, having the evolved $\mathbf{A}(P_0, \mathscr{D}')$ it is required to find the new places, $P_1', P_2', \cdots, P_{\mathscr{N}}'$. Since the

Abel map is a map from the Riemann surface into its Jacobian, finding its inverse is called the Jacobian inverse problem. To find the divisor whose Abel map is obtained by evaluating Eq. (2.28) at an arbitrary z, one can attribute a meromorphic function to this divisor according to the following theorem.

Theorem 2.4.3 (Abel's theorem) *For any meromorphic function, f, on $\mathscr{X}$ with $(f)_{val} = \mathscr{D}$ we have $\mathbf{A}(P_0, \mathscr{D}) = 0$ and also given zero-degree divisor, $\mathscr{D}$, there exists a meromorphic function f, on $\mathscr{N}$ with $(f)_{val} = \mathscr{D}$.*

This meromorphic function can be seen as the ratio of two meromorphic differentials on the Riemann surface with zeros coinciding with the places of the divisor taking into account the necessary singularities and asymptotic values at infinity. Assume the divisor, $\mathscr{D}$, with its places satisfying

$$\phi(P_j) = \theta(\mathbf{A}(P_j) - \mathbf{Z}) = 0, \quad j = 1, \cdots, \mathscr{N},$$

where $\theta(\cdot)$ is the Riemann theta function defined in (2.30). Then, the vector $\mathbf{Z}$ in the Jacobian is

$$\mathbf{Z} \equiv \mathbf{A}(P_0, \mathscr{D}) + \mathbf{K}(P_0),$$

where the vector of Riemann constants, $\mathbf{K}(P_0)$ is defined by

$$\mathbf{K}(P_0) = (K_1(P_0), K_2(P_0), \cdots, K_{\mathscr{N}}(P_0)), \text{ with } K_j(P_0) = \frac{1 + B_{jj}}{2} - \sum_{l \neq j} \int_{a_l} \omega_l A_j. \quad (2.29)$$

Theorem 2.4.4 *Suppose for the vector $\mathbf{Z_1}$ the function*

$$\phi(P) = \theta(\mathbf{A}(P_0, P) - \mathbf{Z_1} - \mathbf{K}(P_0))$$

is not identically zero on $\mathscr{X}$. Then, ϕ has $\mathscr{N}$ zeros, $P_1, P_2, \cdots, P_{\mathscr{N}}$, with their divisor

$$\mathscr{D} = P_1 + P_2 + \cdots + P_{\mathscr{N}} = \mathbf{Z_1}.$$

Solving this problem involves the Riemann theta function [44]

$$\Theta(u_1, \ldots, u_{\mathscr{N}}; \mathbf{B}) = \sum_{\mathbf{l} \in \mathbb{Z}^{\mathscr{N}}} \exp\{\pi i(\mathbf{Bl}, \mathbf{l}) + 2\pi i(\mathbf{l}, \mathbf{u})\}, \quad (2.30)$$

a multi-dimensional Fourier series where $(\mathbf{l}, \mathbf{u}) = l_1 u_1 + \ldots + l_{\mathscr{N}} u_{\mathscr{N}}$. After finding the divisor at the arbitrary distance z, we can find the attributed matrix Φ and in turn, construct the solution to the NLSE using (2.36).

On a Riemann surface, $\mathscr{X}$ and with the standard projection π which defines $\mathscr{X}$ as a two-sheeted covering of $\mathbb{C}$, there are two places, $P^{\pm}$ where $\pi(P^{\pm}) = \infty \in \mathbb{C}$. Now that we have all the means to invert the Abel map, i.e., we can find the evolved divisor, the remaining task is to construct Φ from this evolved divisor. To have an appropriate Φ, in addition to its divisor of poles to coincide with $\mathscr{D}$, its asymptotic behaviour at $\lambda \to \infty$ (corresponding to two places, P^+ and P^-) should be considered. One can uniquely find the vector-valued Baker-Akhiezer function $\Phi^1(t,z;P)$ with the asymptotic behaviour at infinity as:

$$\Phi^1(P) = \left[\begin{pmatrix} 1 \\ 0 \end{pmatrix} + O(\lambda^{-1}) \right] \exp\left(-i\lambda t - 2i\lambda^2 z\right), \quad P \to P^-, \quad \lambda = \pi(P),$$

$$\Phi^1(P) = \alpha\lambda \left[\begin{pmatrix} 0 \\ 1 \end{pmatrix} + O(\lambda^{-1}) \right] \exp\left(i\lambda t + 2i\lambda^2 z\right), \quad P \to P^+, \quad \lambda = \pi(P), \quad \alpha \in \mathbb{C}.$$

$$(2.31)$$

to be

$$\Phi_1^1(P) = \frac{\theta\left(\int_{\infty^-}^{P} \omega + i\mathbf{V}t + i\mathbf{U}z - \mathscr{D} - \mathbf{K}\right)\theta\left(\mathscr{D} + \mathbf{K}\right)}{\theta\left(\int_{\infty^-}^{P} \omega - \mathscr{D} - \mathbf{K}\right)\theta\left(i\mathbf{V}t + i\mathbf{U}z - \mathscr{D} - \mathbf{K}\right)}$$

$$\times \exp\left(it\Omega_1(P) + iz\Omega_2(P) - \frac{i}{2}Et + \frac{i}{2}N_0 z\right)$$

$$\Phi_2^1(P) = \alpha\sqrt{\omega_0}\frac{\theta\left(\int_{P}^{\infty^+} \omega + i\mathbf{V}t + i\mathbf{U}z - \mathscr{D} - \mathbf{K}\right)\theta\left(\mathscr{D} + \mathbf{K} - \int_{\infty^-}^{\infty^+}\right)}{\theta\left(\int_{\infty^-}^{P} \omega - \mathscr{D} - \mathbf{K}\right)\theta\left(i\mathbf{V}t + i\mathbf{U}z - \mathscr{D} - \mathbf{K}\right)}$$

$$\times \exp\left(it\Omega_1(P) + iz\Omega_2(P) + \frac{i}{2}Et - \frac{i}{2}N_0 z\right), \qquad (2.32)$$

with parameters defined as

$$\mathbf{V} = [V_1, V_2, \cdots, V_{\mathcal{N}}], \quad V_j = \int_{b_j} d\Omega_1,$$

$$\mathbf{U} = [U_1, U_2, \cdots, U_{\mathcal{N}}], \quad U_j = \int_{b_j} d\Omega_2, \qquad (2.33)$$

and E, N_0 and ω_0 are determined by asymptotic expansions of the integrals:

$$
\begin{aligned}
\Omega_1(P) &= \pm (z - E/2 + o(1)), \ p \to \pm\infty, \\
\Omega_2(P) &= \pm \left(2z^2 - N_0/2 + o(1)\right), \ p \to \pm\infty, \\
\Omega_3(P) &= \pm (\log z - \log \omega_0/2 + o(1)), \ p \to \pm\infty,
\end{aligned}
\tag{2.34}
$$

where the Abelian integrals Ω_1 and Ω_2 are of the second kind with their only singularities at ∞ and Ω_3 is an Abelian integral of third kind. At some simple connected neighbourhood of infinity with no branch point, each point, λ, is associated to two places, $P^\pm$, identified by the infinity places. For any place in such neighbourhood, the matrix-valued Baker-Akhiezer function can be defined as

$$
\Phi(t, z; \lambda) = \left[\Phi^1(P^+) \ \Phi^1(P^-)\right],
$$

which satisfies the condition of Lemma 2.4.1 and Lemma 2.4.2. Having Φ_1, we use the results of Lemma 2.4.2 to construct the solution to the Schrödinger system as follows

$$
\begin{aligned}
q &= A_0 \frac{\theta\left(i\mathbf{V}t + i\mathbf{U}z - \mathcal{D} - \mathbf{K} + \mathbf{r}\right)}{\theta\left(i\mathbf{V}t + i\mathbf{U}z - \mathcal{D} - \mathbf{K}\right)} \times \exp\left(-iEt + iN_0 z\right), \\
q' &= \frac{4\omega_0}{A_0} \frac{\theta\left(i\mathbf{V}t + i\mathbf{U}z - \mathcal{D} - \mathbf{K} + \mathbf{r}\right)}{\theta\left(i\mathbf{V}t + i\mathbf{U}z - \mathcal{D} - \mathbf{K}\right)} \times \exp\left(iEt - iN_0 z\right), \\
A_0 &= \frac{2\theta(\mathcal{D} + \mathbf{K})}{\alpha\theta(\mathcal{D} + \mathbf{K} - \mathbf{r})},
\end{aligned}
\tag{2.35}
$$

which for the focusing NLSE becomes

$$
q(t, z) = A_0 \frac{\theta\left(i\mathbf{V}t + i\mathbf{U}z - \mathcal{D} - \mathbf{K} + \mathbf{r}\right)}{\theta\left(i\mathbf{V}t + i\mathbf{U}z - \mathcal{D} - \mathbf{K}\right)} \times \exp\left(-iEt + iN_0 z\right),
\tag{2.36}
$$

with $3\mathcal{N} + 3$ degree of freedom consisting of $2\mathcal{N} + 2$ branch points (discrete spectrum), $\mathcal{N}$ in a form of a divisor (auxiliary spectrum) and a complex number, A_0. Since a phase rotation does not change the solution, A_0 can only add one real degree of freedom.

Evaluating the Riemann theta function (2.30) can be challenging for the time variance of its exponential coefficients and the dimensions of the space that $\mathbf{l}$ is drawn from, see appendix B. If one wants to increase the QAM symbol per signal by increasing the genus of the Riemann surface, the computational complexity of evaluating the Riemann theta function increases drastically, see appendix B. To avoid this problem, it is possible for some special NSs to replace the Riemann theta function with some Jacobi elliptic functions, this is explained in appendix A.

2.4.2   Riemann-Hilbert problem

An alternative to the standard algebro-geometric approach is to construct Φ as a solution to a Riemann-Hilbert problem. Take the path $\Gamma = \cup_{j=0}^{\mathcal{N}} \{\Gamma_j\}$ where Γ_js are straight lines connecting λ_j and λ_j^*, one can assume the following [42]:

$$\Phi(t,z;\lambda) = e^{(if_0t+ig_0z)\sigma_3}\mathbf{M}(t,z;\lambda)e^{-(if(\lambda)t+ig(\lambda)z)\sigma_3}, \tag{2.37}$$

where:

1. $f(\lambda)$ and $g(\lambda)$ are scalar functions analytic in $\mathbb{C}\setminus\Gamma$ satisfying the following conditions:
   (i) $f(\lambda) = \lambda + f_0 + O(1/\lambda)$ and $g(\lambda) = 2\lambda^2 + g_0 + O(1/\lambda)$ as $\lambda \to \infty$, with some constants f_0 and g_0;
   (ii) the limiting values of f and g across Γ are related by

   $$f_+(\lambda) + f_-(\lambda) = C_j^f, \ g_+(\lambda) + g_-(\lambda) = C_j^g, j = 0,\ldots,\mathcal{N}, \tag{2.38}$$

   where $f_-(\lambda)$ (or $g_-(\lambda)$) and $f_+(\lambda)$ (or $g_+(\lambda)$) are the values of $f(\lambda)$ (or $g(\lambda)$) when approach the cuts from left and right, respectively, with some real constants C_j^f and C_j^g for $j = 1,\cdots,\mathcal{N}$. C_0^f and C_0^g can be taken arbitrarily and are set to zero.

2. $\mathbf{M}$ is the solution of the RHP with (i) the jump conditions

   $$\mathbf{M}^-(t,z;\lambda) = \mathbf{M}^+(t,z;\lambda)\mathbf{J}_j(t,z), \quad \lambda \in \Gamma_j, \tag{2.39}$$

   where

   $$\mathbf{J}_j(t,z) = \begin{pmatrix} 0 & ie^{-i(C_j^f t + C_j^g z + \phi_j)} \\ ie^{i(C_j^f t + C_j^g z + \phi_j)} & 0 \end{pmatrix}, \tag{2.40}$$

   where $\mathbf{M}^-(t,z;\lambda)$ and $\mathbf{M}^+(t,z;\lambda)$ are the values of $\mathbf{M}(t,z;\lambda)$ when approach the cuts from left and right, respectively, and (ii) the normalization condition $\mathbf{M} \to I$ as $\lambda \to \infty$.

From $\mathbf{M}$, one can find $Q(t,z)$ using

$$Q(t,z) = i\left[\sigma_3, \ e^{(if_0t+ig_0z)\sigma_3}\mathbf{M}_1(t,z)e^{-(if_0t+ig_0z)\sigma_3}\right], \tag{2.41}$$

where $\mathbf{M}_1(t,z)$ is determined by the asymptotic relations $\mathbf{M}(t,z,\lambda) = I + \frac{\mathbf{M}_1}{\lambda} + O(\lambda^{-2})$ as $\lambda \to \infty$. Notice that the conditions above uniquely determine C_j^f and C_j^g for $j = 1,\ldots,\mathcal{N}$ as

well as f_0 and g_0. Namely, if $\mathscr{N} \geq 3$, then C_j^f and C_j^g are respectively the unique solutions of the systems of linear algebraic equations

$$\sum_{j=1}^{\mathscr{N}} C_j^f \int_{\Gamma_j} \frac{\xi^k d\xi}{w(\xi)} = 0, \qquad k = 0, \ldots, \mathscr{N} - 2,$$

$$\sum_{j=1}^{\mathscr{N}} C_j^f \int_{\Gamma_j} \frac{\xi^{\mathscr{N}-1} d\xi}{w(\xi)} = -2\pi i, \tag{2.42}$$

and

$$\sum_{j=1}^{\mathscr{N}} C_j^g \int_{\Gamma_j} \frac{\xi^k d\xi}{w(\xi)} = 0, \qquad k = 0, \ldots, \mathscr{N} - 3,$$

$$\sum_{j=1}^{\mathscr{N}} C_j^g \int_{\Gamma_j} \frac{\xi^{\mathscr{N}-2} d\xi}{w(\xi)} = -4\pi i,$$

$$\sum_{j=1}^{\mathscr{N}} C_j^g \int_{\Gamma_j} \frac{\xi^{\mathscr{N}-1} d\xi}{w(\xi)} = -2\pi i \sum_{j=0}^{\mathscr{N}} (\lambda_j + \lambda_j^*), \tag{2.43}$$

where $w(z)$ is defined in Eq. (2.24). If $\mathscr{N} = 1$, then C_1^f and C_1^g are determined by the last equation in (2.42) and (2.43); if $\mathscr{N} = 2$, then C_j^f, $j = 1, 2$ are determined by the system in general form (2.42) whereas C_j^g, $j = 1, 2$ are determined by the system of two last equations in (2.43). If we start from the known main spectrum, i.e known Γ_js and $w(\lambda)$, calculating the contour integrals in Eqs. (2.42) can be done accurately with a few integral points and a simple linear system is to solved with the resulting values. Then $f(\lambda)$ is determined, for all $\mathscr{N} \geq 1$, by

$$f(\lambda) = \frac{w(\lambda)}{2\pi i} \sum_{j=1}^{\mathscr{N}} \int_{\Gamma_j} \frac{C_j^f d\xi}{w(\xi)(\xi - \lambda)} \tag{2.44}$$

and $g(\lambda)$ is determined by

$$g(\lambda) = \frac{w(\lambda)}{2\pi i} \sum_{j=1}^{\mathscr{N}} \int_{\Gamma_j} \frac{C_j^g d\xi}{w(\xi)(\xi - \lambda)}$$

for $\mathscr{N} \geq 2$ and by

$$g(\lambda) = 2w(\lambda) + \frac{w(\lambda)}{2\pi i} \int_{\Gamma_1} \frac{C_1^g d\xi}{w(\xi)(\xi - \lambda)}$$

for $\mathcal{N} = 1$. In turn, f_0 and g_0 are determined from the asymptotic relations $f(\lambda) = \lambda + f_0 + O(1/\lambda)$ and $g(\lambda) = 2\lambda^2 + g_0 + O(1/\lambda)$ as $\lambda \to \infty$ of $f(\lambda)$ and $g(\lambda)$.

In the RHP approach it is also possible to have an explicit expression for the solution but numerically solving the RHP suffices for our purpose. Having all the parameters mentioned above, we define the jump matrices and use the `RHSolve`, a package in Mathematica to get the numerical solution to the RHP at each point in time and distance [47]. The first point to note here is the way the computational complexity scales with the number of signal samples in time this is a direct result of independent calculation of each point in time and distance. As pointed out earlier, the `RHSolve` finds the solution to the RHP at each point in time and space, therefore, the complexity scales as $O(N)$ when N is the number of samples in time. The most resource demanding stage of the inverse transformation as described before is solving the RHP, i.e. finding $\mathbf{M}$ in Eq. (2.39) from the jump matrices $\mathbf{J}_j(t,z)$ defined in Eq. (2.40). This can be done by solving an integral equation

$$\boldsymbol{\mu} - \mathscr{C}_{\mathbf{G}}\boldsymbol{\mu} = \boldsymbol{I},$$

where the operator $\mathscr{C}_{\mathbf{G}}$ is defined as follows:

$$(\mathscr{C}_{\mathbf{G}}\boldsymbol{f})(t,z,\xi) := \frac{1}{2\pi i}\int_{\Sigma}\frac{\boldsymbol{f}(s)(\mathbf{G}(t,z,s)-\boldsymbol{I})}{s-\xi^-}ds, \quad \xi \in \Gamma. \tag{2.45}$$

The `RHSolve` can perform this operation in an efficient way in which to solve the Cauchy integral we need to deal with fast discrete cosine transform (DCT) and compute Cauchy integral (2.45) at n Chebyshev points of the second kind, where n is the total number of spectral points on the arcs (directly related to the resolution $\Delta\lambda$ between the adjacent discretisation points). The numerical error is shown to decay spectrally as n grows [48]. Computing (2.45) can be significantly expedited by expanding the solution using the Chebyshev polynomials of the first kind inasmuch as the expressions for the Cauchy integral involving these polynomials are known explicitly. Evaluating the n Chebyshev polynomials can be done using $O(n\log n)$ floating point operations. To facilitate comparison between the complexity of evaluating the Riemann theta function with solving the RHP, keeping the spectral resolution, $\Delta\lambda$ fixed (i.e. $n = n_0\mathcal{N}$ where n_0 is the number of points over each cut), one can find the computational complexity of our proposed method to be

$$O\left(N\mathcal{N}n_0\log(\mathcal{N}n_0) + NM(\mathcal{N}n_0)\right),$$

where $M(n_1)$ is the complexity of solving an $n_1 \times n_1$ linear system. The equation above shows that as opposed to evaluating the Riemann theta, the computational complexity of solving the

RHP does not scale exponentially with the number of cuts which is going to be important when the approach is generalised to a higher symbol per signal communication. This feature is the principle advantage with respect to the alternative approach of the construction of algebro-geometric solutions where the Riemann theta function (2.30) is used [48].

2.4.3   Numerical methods for the periodic NFT

Various algorithms and numerical routines to perform different stages of finding the NS of a periodic solution and constructing a solution from the NS have been proposed over the last few decades. In calculating the NS, constructing the monodromy matrix can be done through different numerical approximations of the differential operator such as *Runge-Kutta*, *forward-Euler*, *Cranck-Nicolson* and *Ablowitz-Ladik* [49, 50, MK5]. In these methods, and other methods of constructing the monodromy matrix by approximating the exponential matrix such as *Boffetta–Osborne* [51, 52], starting from the boundary condition, the Zakharov-Shabat equation is numerically solved to find two bounded solutions and form the fundamental matrix. From the trace of this matrix, one can find the discrete spectrum by looking for the zeros of an analytic function using various methods [52]. Finding the monodromy matrix is followed by a root finding algorithm which in a general case can be a simple Newton-Raphson routine or any approach as such or for the polynomial approximation solving the eigenvalue problem pertinent to the companion matrix of the polynomial. Using the Floquet theory, the spectrum of the Zakharov-Shabat operator can be efficiently found for a periodic signal directly from solving an eigenvalue problem [53, 54]. All these methods are different in accuracy, time and memory consumption from which the Ablowitz-Ladik method is chosen here due to its acceptable accuracy taking into account the speed and low-memory requirement [49, MK5]

The NFT for periodic signals by numerically solving the evolution equations of the auxiliary spectrum is reported in [32] where in [55] a particular case of a one-band signal is considered. To perform the inverse transformation through the now-standard algebro-geometric approach, there has been much effort in providing a generic universal tool covering a wide range of applications on different platforms. Among these works one can point out the `Abelfunctions`, a Python library for computing Abelian functions in Python and Sage [56], and the `algcurves` package for Maple software [57, 58]. Other attempts to evaluate algebro-geometric solutions in Matlab is made in a series of works, for example [59]. In particular, to solve the Jacobi inverse problem, it is necessary to construct the Riemann constant vector (2.29), which can numerically be done to an arbitrary level of accuracy, although still far from what a real-time application such as fibre-optic communication requires [60–62].

Inverse transformation by means of numerically solving an RHP is also explored for different nonlinear equations [63, 64] and a numerical package for Mathematica, `RHPackage`, is available to do so [47]. Since the Riemann theta function (2.30) is a multi-dimensional Fourier series in which the number of contributing terms grows very fast as the intended accuracy increases, numerically calculating it is a challenge. This is, in fact, the main advantage of inverse transformation via solving an RHP over the standard algebro-geometric approach. Appendix B discusses the numerical calculation of the Riemann theta function.

A common scheme to construct some solutions of the NLSE is the Darboux (or dressing) method. In this method, starting from a solution to the NLSE (either constant or periodic in time and space [65, 66]), new eigenvalues are added to the discrete spectrum and the corresponding Jost functions are constructed iteratively [66, 67].

2.5 Vanishing boundary signals

So far, a signal with a finite number of gaps in the spectrum was considered. Since a considerable amount of work has been done on using the vanishing boundary signals where $|q(t,z)| \to 0$ as $t \to \infty$ faster than any polynomial, in fibre-optic communication systems, here we revisit the conventional definition of the NS and other spectral parameters from a finite-gap theory perspective. We can consider such signals as fast-decaying periodic signals with period T where $T \to \infty$. As the signal decays fast, the scattering parameters are meromorphic functions, so the spectrum of the Zakharov-Shabat operator consists of the real axis plus some isolated complex numbers (in complex conjugate pairs for the focusing NLSE). Therefore, in order to construct a solution, the RHP (2.9) has to be solved for a jump on the curve $\Gamma = \mathbb{R}$ where $\Phi^-(t,z;\lambda)$ and $\Phi^+(t,z;\lambda)$ are analytic in the lower and upper half plane, respectively, and with time-invariant S_{ij}s we have

$$\begin{pmatrix} \Phi_1^-(t,z;\lambda) \\ \Phi_2^-(t,z;\lambda) \end{pmatrix} = \begin{bmatrix} S_{11} & S_{12} \\ S_{21} & S_{22} \end{bmatrix} \begin{pmatrix} \Phi_1^+(t,z;\lambda) \\ \Phi_2^+(t,z;\lambda) \end{pmatrix}, \quad \text{as} \quad t \to \infty. \tag{2.46}$$

The equation above can be rearranged into a transfer operator in the time domain. As the solution decays fast as t grows, there exist Jost solutions with the following boundary conditions

$$\lim_{t \to \infty} \Phi_1^+(t,z;\lambda) = \begin{pmatrix} 0 \\ 1 \end{pmatrix} e^{j\lambda t}, \quad \lim_{t \to \infty} \Phi_1^-(t,z;\lambda) = \begin{pmatrix} 1 \\ 0 \end{pmatrix} e^{-j\lambda t},$$

$$\lim_{t \to -\infty} \Phi_2^+(t,z;\lambda) = \begin{pmatrix} 1 \\ 0 \end{pmatrix} e^{-j\lambda t}, \quad \lim_{t \to -\infty} \Phi_2^-(t,z;\lambda) = \begin{pmatrix} 0 \\ 1 \end{pmatrix} e^{j\lambda t},$$

with $\mathscr{W}(\Phi_1^+(t,z;\lambda),\Phi_2^+(t,z;\lambda)) = S_{12}^{-1}$ and $\mathscr{W}(\Phi_1^-(t,z;\lambda),\Phi_2^+(t,z;\lambda)) = -S_{11}S_{12}^{-1}$ where $\mathscr{W}(.)$ is the Wronskian. The representation of the transfer matrix using the Wronskian is apt since $\{\Phi_1^-(t,z;\lambda),\Phi_1^+(t,z;\lambda)\}$ and $\{\Phi_2^-(t,z;\lambda),\Phi_2^+(t,z;\lambda)\}$ are two sets of linearly independent function which can form a basis for all Jost functions. If the ZSS (2.4) has eigenvalues, say λ_j, the sought functions, Φ, need to be meromorphic. In such a case, $S_{12}^{-1} = 0$ and since $\Phi_1^+(t,z;\lambda_j)$ and $\Phi_2^+(t,z;\lambda_j)$ are analytic in the same domain, they are linearly dependent, $\Phi_1^+(t,z;\lambda_j) = \hat{c}_j \Phi_2^+(t,z;\lambda_j)$. That means, to solve the RHP it is necessary to have the residue of S_{11} at these eigenvalues. Together with these residues, the transfer matrix can be used as a data carrier in fibre optic communication. The elements of the transfer matrix which are required to reconstruct a solution at different distances from the transmitter given the transmitted signal are S_{11}, the eigenvalues of the ZSS, λ_j, and the residues of S_{11} at these eigenvalues, c_j. The set of these eigenvalues and the residues are called the discrete spectrum and S_{11} is called the continuous spectrum as a function of the real argument λ. The NS has the following evolution in z:

$$c_j(z) = c_j(0)e^{2i\lambda_j^2 z}, \quad S_{11}(z) = S_{11}(0)e^{2i\lambda^2 z}, \tag{2.47}$$

and λ_js are invariant.

As an important example, a multi-soliton solution can be constructed as a limit at which eigenvalues are degenerate. Following the notations of the previous section, when the discrete spectrum consists of $\mathscr{N}+1$ pairs of complex conjugate eigenvalues $\{\lambda_j,\lambda_j^*\}_{j=0}^{\mathscr{N}}$, take some value $\alpha > 0$ and put [44]

$$\lambda_0 = -\lambda_{\mathscr{N}}^* = -\alpha.$$

Now, let take the limit

$$\lambda_{2j},\lambda_{2(j+1)} \to \zeta_j, \quad \text{for} \quad j = 1,\cdots,\mathscr{N}, \quad \text{where} \quad \zeta_m \neq \zeta_n \text{ if } n \neq m.$$

Furthermore, by letting $\alpha \to 0$ the spectrum becomes a combination of $\mathscr{N}$ eigenvalues ζ_j and $\mathbb{R}$, hence, the discrete and continuous spectrums, respectively. It is possible to show that $|q(t,z)| \to \alpha$ as $t \to \infty$ (see appendix D and [44, section 4.4]).

2.5.1   A few challenges

Aside from the above-mentioned numerical difficulties caused by the Riemann theta function, special consideration should be practised while constructing a periodic signal. One issue is to make sure the solution is periodic. Since the periodicity of the solution is determined by the periodic properties of the Riemann theta function, here we investigate conditions for

periodicity. The Riemann theta function has the following periodicity property

$$\Theta(\mathbf{u}) = \Theta(\mathbf{u} \pm \mathbf{e_j}), \ \mathbf{e_j} = [0, \cdots, 1, \cdots, 0] \quad \text{zero except at the } j\text{-th element.}$$

Since the solution is proportional to (see Eq. (2.36)):

$$h(t, z) = \frac{\Theta(\mathbf{u} + \mathbf{d})}{\Theta(\mathbf{u})},$$

where $\mathbf{u} = \mathbf{V}t + \mathbf{U}z + \mathbf{c}$ for some vectors $\mathbf{c}$ and $\mathbf{d}$, the solution has the same periodicity property as the Riemann theta function. Therefore, to have a periodic signal in time, t, it suffices to have commensurable numbers as the elements of $\mathbf{V}$ defined in Eq. (2.33). The same argument applies for a signal construction through solving an RHP where C_j^fs should be commensurable. This condition can be met by adjusting the places of the eigenvalues in the discrete spectrum. In the following chapters, two examples of periodic signals made through solving an RHP and with the algebro-geometric approach will be presented. In the first example, it is shown that the condition to have a periodic signal only influences the real part of the eigenvalues. In the second, for this 1-genus signal, one of the elements of the two-element vector $\mathbf{V}$ is zero; hence, the periodicity is guaranteed and the period is determined only by the other element of $\mathbf{V}$.

Another point to pay extra attention to in numerically calculating the solution is in integrating on contours close to the singularities of the functions. Notably, in finding C_j^f and C_j^g, paths of integration should be chosen in a way to avoid branch points [68, MK9].

2.6   Numerical methods

Calculating the NS of a function, *direct transformation*, is to find the spectrum of the associated Zakharov-Shabat operator. This can usually be done by numerically integrating this differential equation and find two linearly independent solutions to compute the scattering parameter in (2.9) or (2.13). The main part of the numerically solving the Zakharov-Shabat equation is to replace the differential operator, ∂_t, with a finite-difference approximation which can be Forward-Euler, central-difference, Runge-Kutta, etc. The most widely used routines of this category of algorithms are Boffetta-Osborne [51, 52], Cranck-Nicolson and Ablowitz-Ladik [49, 50]. However, one can use a collocation method to solve an eigenvalue problem, which although consumes a rather considerable memory, delivers fast and for eigenvalues with large enough imaginary parts, the most accurate results, see [50, 53] and [69, section 7.3]. In [MK5] a comparison between three different direct transformation

algorithm regarding their accuracy and runtime is taken place and it is concluded that the Ablowitz-Ladik scheme has the most favourable combination of these two criteria. Appendix C outlines steps of three routine;Ablowitz-Ladik, spectral and layer-peeling in computing the NS of a periodic signal in terms of their numerical accuracy and normalised runtime.

Direct transformation for vanishing and periodic signals are basically the same except for some algebraically trivial operations. The difference, however, emerges when starting from the NS, one intends to construct the signal, *inverse transformation*. For signals with vanishing boundaries, the first and natural way for inverse transformation is to solve the so-called Gelfand-Levitan-Marchenko equation (GLME) for $K_1(t,t')$ [41]:

$$K_2^*(t,t') + \int_t^\infty K_1(t,s)F(s+t')ds = 0,$$

$$K_1(t,t') - \int_t^\infty K_2^*(t,s)F^*(s+t')ds = F^*(t+t'), \tag{2.48}$$

where the kernel is

$$F(t) = \frac{1}{2\pi}\int_{-\infty}^\infty r(s)e^{i\lambda s}d\lambda + i\sum_{j=1}^{2\mathscr{N}+1}\gamma_j e^{i\lambda_j s},$$

where $2\mathscr{N}+1$ is the number of eigenvalues, $r(\cdot)$ is the continuous spectrum and γ_j are the amplitude of the discrete spectrum. Then $q(t,z) = -2K_1(t,t)$ yields the solution. There are a few ways to solve this equation efficiently [70–72]. A fast inverse transformation algorithm for a complete NS consisting of a continuous and a discrete part has been proposed in [73]. In this work, a fast *layer peeling* approach and a fast Darboux transform are combined. For a case with only a continuous spectrum involved, the inverse transformation can be done quite fast and accurately [71]. On the other hand, for a purely solitonic signal, a more popular approach is the Darboux transformation. The inverse transformation can also be formulated as a Riemann-Hilbert problem [28]. This approach would be extensively explained, especially for periodic signals, in the following sections. The main challenges of inverse transformation for periodic signals and different algorithms to carry out the calculations is also studied in the previous chapter.

In this chapter, a brief introduction to the concept of NFT is presented and a general definition for the NS is conferred. The direct and inverse transformation stages for a finite-gap signal is discussed and a brief argument on how to get a particular example of this kind of signals as a vanishing signal is made. More details and some definitions are left for the appendices but a basis to construct a communication system is established.

Chapter 3

NFT-based communication

Using NFT, the linear and nonlinear effects of fibre can be described as a linear evolution of the NS of the signal. This linear evolution paves the way to design new communication systems. It can either be used to carry data from the transmitter to the receiver or can play the role of a digital back propagator to rectify the fibre distortions or a combination of both. The most straightforward communication system using NFT is an eigenvalue communication proposed in the seminal paper of Hasegawa and Nyu in 1993 [74]. In a more general form, this idea is revived in a series of articles in which a detailed mathematical background and description of numerical routines to implement NFT is presented [28, 50, 75].

3.1   A brief review of NFT

Here a short introduction to the concept of NFT and some necessary definitions is presented but a more thorough one will follow in the next chapter. As mentioned in the introduction, NFT parametrises a family of solutions to the NLSE with a set of complex numbers called the nonlinear spectrum (NS). The NS is related to the solution in a non-straightforward way which is explained in the following. For some nonlinear partial differential equations (NPDE) such as the NLSE, there is an auxiliary differential equation with the solution to the NPDE playing the role of a potential. The spectrum of this auxiliary equation has some interesting characteristics such as being partially invariant or having trivial evolution with the propagation of signal along the propagation dimension. Using these traits, it is possible to introduce the NS as a representation of the signal with simple evolution in distance.

In general, this NS consists of two parts: the continuous spectrum and the discrete part, both complex numbers. The discrete part represents the static and the continuous one represents the dynamic part of the NS. The static part is attributed to the solitonic component of the signal while the dynamic part has to do with the dispersive elements. Since
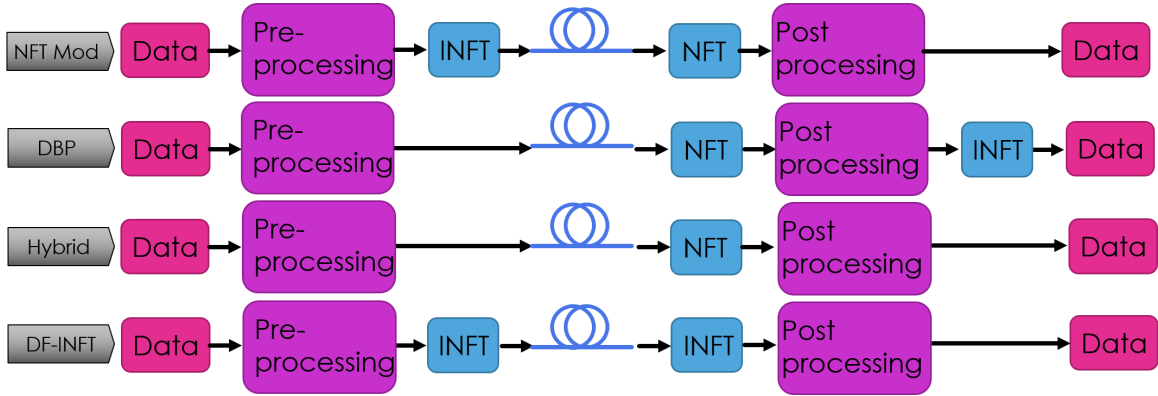
Fig. 3.1 Different scenarios of using NFT in a fibre-optic communication system.

the combination of the discrete and continuous spectrums fully determines the signal, it is necessary to have a full knowledge about the both of them, in order to construct a signal with a particular set of parameters, i.e the NS. The fact that the NS changes in a simple manner as the signal travels from the transmitter to receiver makes the NS a suitable carrier for information. Using the NS to transfer data leads to an NFT-based communication system.

There are four main configurations used in NFT-based communication [76]; 1) NFT modulation in which either the discrete spectrum, the continuous spectrum or both are modulated at the transmitter, 2) digital back-propagation (DBP) in which the DBP is implemented using the NS and implanted as an additional device at the receiver, 3) the hybrid setting in which a signal with known NS (usually the discrete spectrum) is transmitted, and its NS is used to retrieve data at the receiver [77], and 4) a decision-feedback scenario which can be considered as a variant of the NFT modulation scheme but involves performing INFT at the receiver [78], see Fig. 3.1. The overall throughput of these systems may not overtake the best and state-of-the-art fibre-optic techniques but there is ongoing progress in the overall performance. Some comparisons have been made between the available systems and NFT-based ones [25, 79]. Most of the studies on NFT-based communication systems consider solutions to the NLSE with a vanishing boundary condition. As shown in the following chapters, this leads to a particular case of a finite-gap solution. Here we first explain the proposed systems for only vanishing boundary signals and then move on to a more general case of periodic signals.

3.2   Vanishing boundary signals

A signal where, $|q(t)| \to 0$ faster than any polynomial as $t \to \pm\infty$, has an NS of the type shown in Fig. 3.2. The NS consists of some eigenvalues with their spectral amplitudes, called
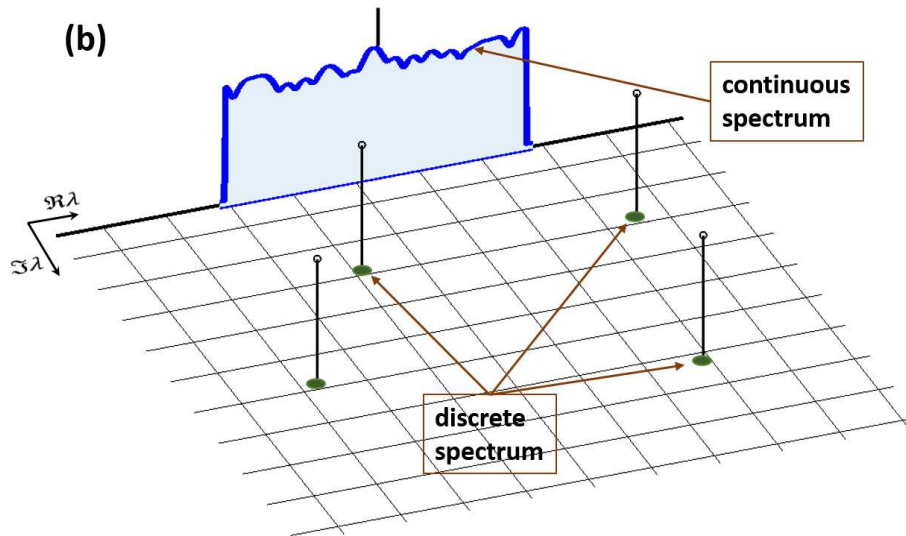
Fig. 3.2 Nonlinear spectrum of a signal with vanishing boundary condition.

the discrete spectrum, plus one continuous spectrum. This continuous spectrum lies on the real axis, for the vanishing behaviour of the signal guarantees the existence of a bounded solution of the Zakharov-Shabat system (ZSS) for real spectral parameters, more on this in Chapter 2. The discrete spectrum depicts the solitonic part of the signal while the remaining part, the radiating components, are described by the continuous spectrum. A soliton, then, can be defined as a signal with only a discrete spectrum as its NS. Both these spectrums can be used as data bearers, and both are necessary, in general, in the DBP scheme [76].

3.2.1 Digital back propagation using NFT

Before anything, NFT (or inverse scattering transform (IST)) is a method to solve the NLSE given a boundary condition. Within the limits of validity of the NLSE, the received signal is a snapshot of a solution to the NLSE. This is regardless of how much the dispersion and Kerr nonlinearity distort the transmitted signal. The received signal may be changed beyond what can be recognised by a receiver that is designed for linear channels. A boundary condition fully determines the solution, and therefore, given the received signal, it is possible to find the input signal to the fibre. This scenario is in fact back propagating the signal to the receiver which is usually done by numerically solving the NLSE using a SSF method [13, 15]. DBP suffers from a high computational complexity and susceptibility to the nonlinear noise-signal interaction [16]. Therefore, other methods like combining linear distortion compensation and nonlinear phase rotation, Volterra equalisation, and optical phase conjugation (OPC) are preferred.

In [80] a back-propagation scheme using NFT is proposed, in which at the receiver, the NS of the received signal is calculated through a direct transformation routine (in this work Ablowitz-Ladik). This NS is then back-propagated in the nonlinear Fourier domain according to the relations mentioned in Section 2.5. This evolved NS is then used in an inverse transformation routine to construct the signal which is supposedly the one that is sent. The reconstructed signal is sent to a conventional receiver. In this application of the NFT, one needs to calculate both the discrete and continuous spectrum and consider them both in the inverse transformation stage. However, in this study, the considered fibre has normal dispersion to avoid the existence of solitons, so the direct and inverse transformations only include the continuous spectrum. For the anomalous dispersion, by assuring that the signal does not have any solitonic component, some simulation results are presented showing a better performance in comparing to a digital back-propagation scheme with 4 steps per span for a 100 Gb/s QPSK OFDM signal up to 4000 km [80].

One of the constraints of this proposed system is the emergence of solitons due to the integrability breaking nature of the inevitable additive amplified spontaneous emission (ASE) noise. Since at the receiver, only the continuous spectrum is taken to account, this energy transfer from the continuous spectrum to the discrete one leads to a loss in the effective SNR [MK1, MK2]. Another problem in such a system is the energy-dependence of the accuracy of the NFT calculations.

3.2.2 Modulating discrete/continuous spectrum

The first example of an NFT-based communication system was a simple eigenvalue communication scheme in which the data is mapped on the eigenvalues of a sech signal [74]. The number of degrees of freedom to carry data is quite limited in this system. The next step to improve the amount of information to be carried by the NS can be the modulation of the so-called spectral amplitude attributed to the eigenvalues [81–84]. In [82] the achievable mutual information (MI) of such a system is studied where a MI of around 10 bits/symbol is achieved over an ideal link of 725 km with for a 64-PSK modulation of the spectral amplitude of two eigenvalues. When working with signals with only the discrete spectrum, we suffer from small spectral efficiency due to a sizeable time-bandwidth product of the signal [85]. The usage of the continuous spectrum can offer a solution to the efficiency problem. The application of nonlinear continuous spectrum (borrowed from some popular linear systems like OFDM or Nyquist) has been studied and experimentally scrutinised in the last few years [79, 86–89]. Another advantage of this system is the possibility of pre-compensating the fibre dispersion which halves the required guard intervals, hence, increases the achievable spectral efficiency [90]. This approach, has helped us to increase the resulting capacity of

NFT-based systems. Moreover, unlike the eigenvalue communication in which the fibre needs to be with anomalous dispersion, this system can perform in a normal dispersion region [91, 92]. A limiting characteristic of NFT-based communication for vanishing boundary signals is the fact that the signal duration is not well controllable, especially when dealing with continuous spectrum. However, it turns out that the signal width is limited to the width of the inverse Fourier transform of the scattering coefficient [93]. Therefore, modulating this function and controlling the duration of its time domain "image" leads to a signal with pre-determined duration. In this method, instead of modulating the continuous spectrum, one can map data on the b function. Another benefit of modulating the b function is that the impact of noise is smaller [94]. This method is experimentally demonstrated and it has been shown that the record high data rate of 100 Gbps can be achieved as a result of the controlled signal duration and also due to the lower noise impact on the data-carrying part of spectrum [94].

The most general case in which a signal is constructed from an arbitrary NS with continuous and discrete spectrums will offer higher data rate and spectral efficiency. A series of papers have studied and experimentally demonstrated the achievable data rate of a system which fully implements the NS to convey data [95–98].

3.2.3   NFT in dual-polarisation systems

By means of the NFT, we can find solutions to the NLSE describing the light propagation in one polarisation. Using NFT attributed to a single polarisation on two polarisations independently, although providing higher data rates, introduces some mismodelling error [91, 99]. However, the formalism of the dual polarisation NFT has been known since the mid of 1970s as well: the Manakov equations govern the evolution of the envelope of the electric field in an SMF (in a leading order approximation) with random birefringence for two polarisations, and it is shown that these equations are integrable through the IST (NFT) [100, 101].

Implementing NFT in a dual-polarisation communication system was studied when the NS consists of only the discrete spectrum [102]. In this work, an error-free transmission up to 370 km is realised. The signal is constructed using the so-called Darboux transformation and the data is mapped on the spectral amplitudes [103]. The continuous spectrum for a dual-polarisation transmission is used in [104] and is stated that even considering the polarisation-mode dispersion (PMD) the overall BER does not deteriorate so much and the data rate doubles compared to a single-polarisation transmission. These results are verified through experiment in [105]. In a recent work, a record spectral efficiency of 7.2 bit/s/Hz in a dual-polarisation NFT-based system with $b-$modulation is reported [106]. A dual

polarisation system with both discrete and continuous spectrum modulated and also using NFT for a multi-mode fibre communication is the next step along this path.

3.2.4 Signal processing tools in the nonlinear spectrum

The most interesting characteristic of NFT and the prominent reason to modulate the NS is the fact that the evolution of the NS is linear as opposed to the signal evolution in the time domain. This means that the highly nonlinear medium, i. e. the fibre, can be transformed into a linear channel, where both nonlinearity and dispersion reduce to a simple phase rotation of input NS. This, in turn, makes it possible to implement a rich collection of algorithms borrowed from the conventional linear communication. Of course, the linear evolution of the NS has some conditions and constraints such as the impact of noise, higher order dispersions, fibre loss, etc.; however, some previously defined approaches of the linear communication are still effective.

One of the challenges attributed to an NFT communication system design is that the numerical errors coming from the NFT processing computation have a considerable dependence on the signal power. Signal power, in turn, is determined by the NS of the signal; hence, the numerical errors highly depend on the location of eigenvalues that defines the resulting signal power. A natural way to deal with such a problem, especially in one symbol per signal communication, is the constellation shaping in which the configuration of the transmitted symbols depends on the contribution of different points in the overall system performance. In a similar approach–the probabilistic shaping– the symbols with the highest contribution to the overall noise would be chosen less frequently [107] and [MK3].

Another problem is the specific impact of noise in a nonlinear inverse synthesis (NIS) system [79, 86] in which no solitonic component is present: the noise can induce new elements in the discrete spectrum. This phenomenon leads to an energy partition between the spurious NS part and the data carrying continuous spectrum, hence, reducing the effective SNR. This problem can be alleviated by introducing filtering in the NS domain where the unwanted solitonic components of the NS are removed. These spurious elements can further lead to an "absorption" of more energy from the continuous spectrum. Removing these components, although decreases the signal power, can improve the overall system performance [MK1,MK2]. One explanation for this phenomenon is the impact of additive ASE noise which not only influence the integrability of the underlying system, but also, when aggregated, can evolve into some solitonic components. To fully understand this effect and other impacts of noise in an NFT-based system more investigation should be carried out.

An intriguing possibility in the NS domain is implementing a linear equaliser in addition to the simple phase rotation at the receiver. For instance, it has been shown that the

noise-induced shift of different (complex) frequency components in the NS domain in a communication system based on the eigenvalues are correlated [83]. This means that one can use the information carried by all elements of the NS to rectify some distortions in this domain [83]. In [83], a simple linear minimum mean-square estimator (LMMSE) has been introduced in the NS domain and a noticeable improvement is achieved.

3.2.5 Capacity of an NFT-based system

From the information theory point of view, the capacity of the fibre does not depend on how we approach the channel model, i.e. the NLSE in our case. This means, we can implement the IST formalism (i.e. the NFT-based approach) to evaluate the capacity of the fibre, as long as there is a one-to-one relation between the signal in time domain and its NS. Thus, we can evaluate the MI quantities from the NS. However, the projection of the additive white Gaussian noise (AWGN) onto the NS modes results in a different effective noise affecting the dynamics inside the nonlinear Fourier domain. Therefore, to study and compare the achievable data rate of an NFT-based communication system with a conventional one, it is necessary to model the noise in the nonlinear Fourier domain.

The AWGN ASE noise emerges as an additive random process in the potential of the ZSS. In the numerical study of the NFT, in order to calculate the scattering data, we can iteratively find the consecutive values of the eigenfunctions in time. This system can be perceived as a linear dynamical model based on which a Kalman filter can be designed. Thus, statistical analysis of ZSS and scattering coefficient in the presence of this noise term can be rendered up to the second order characteristics. This is done for a vanishing boundary NFT with continuous and discrete spectrums [108].

In another view, a perturbative analysis is applied to model the noise in the nonlinear Fourier domain for an NIS system [24]. In that work, the autocorrelation function of the noise in the nonlinear domain is estimated. For that, based on a perturbation analysis, the evolution of the continuous spectrum perturbed by noise is used. In this evolution, the projection of noise on the elements of the Jost solutions to the ZSS plays the role of noise. The Jost functions are calculated for the unperturbed system (noiseless) and then used to find the power of the projected noise. A lower bound for the capacity of an OFDM and a Nyquist system in the large distance limit is derived. It is also made evident that the NFT-based communication system can be considered as a crosstalk-free communication in the leading approximation. It is finally shown that there is a lower bound for the capacity per symbol of 10.7 bits per symbol in a 500 GHz communication over a 2000 km link [24]. Other works have also utilised a perturbation approach to calculate the statistical characteristics of a discrete spectrum transmission [75, 109], capacity of a soliton communication [110, 111],

and the capacity of a continuous spectrum communication [89] and [25]. In the latter, a long-haul approximation model for a similarity solution to the NLSE is considered. It has been shown that the achievable data rate of an NFT-based system can surpass the one for a WDM system for a given signal power and bandwidth where an upper bound of 10.5 bits/s/Hz for the spectral efficiency is predicted [25]. This predicted upper bound has not been realised, in fact, the demonstrated spectral efficiency is as low as 1.54 bits/s/Hz which makes an NFT-based communication not spectrally efficient in the current form [25]. Spectral efficiency shows the amount of information per the total degrees of freedom $T \times B$a where T and B are the time duration and signal bandwidth, respectively, while the channel capacity for a band-limited signal shows the achievable error-free information rate using a particular bandwidth.

An entirely different approach in the statistical analysis of the NS is taken in [112, 113]. In these works, the concept of density of states (or density of eigenvalues) as a descriptor of the statistical characteristics of the eigenvalues of the ZSS is considered. The Fokker-Planck equation is solved for the probability distribution of the scattering parameters in the stationary state and the density of eigenvalues is obtained using the Lyapunov exponent in the generalised Thouless formula. Results for a random Gaussian input is reported.

3.3 Comparing vanishing boundary and periodic NFT

Both kinds of solutions to the NLSE; finite-gap and decaying, are determined by a family of parameters called the NS (see Figs. 3.2 and 3.3) which provides them with the same number of degrees of freedom. Their communication characteristics, however, can make a considerable difference in terms of performance, computational complexity of the numerical routines, etc. Although the vanishing boundary NFT has been more widely studied and implemented, it has some drawbacks which suggest resorting to the more mathematically demanding PNFT. Here we explain some advantages of the PNFT over the conventional one;

- A periodic signal is confined in time in its period, unlike a vanishing signal where to have acceptable level of accuracy a significant number of samples need to be gathered at the decaying wings. This in fact, improves the spectral efficiency of the system.

- A periodic solution can be constructed with a predefined signal duration.

- Using cyclic extension, the processing window at the receiver is as large as the data bearing part of the signal, unlike the vanishing signal for which the broadened window (due to the chromatic dispersion) is to be processed. The reason is that a periodic in
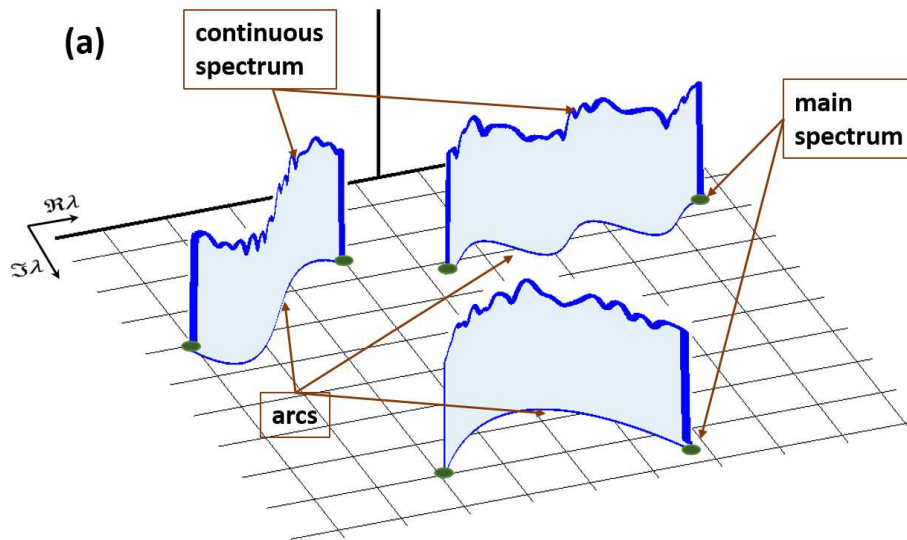
Fig. 3.3 Nonlinear spectrum of a finite-gap signal where green dots represent the main spectrum and segments of the continuous spectrum are shown.

time solution to the NLSE is periodic at different distances from the transmitter with the same period, and all the information of the signal is contained in one period of it. This, particularly in wideband communication, can lead to a great computational complexity reduction, see Fig. 3.4.

- By providing a seamless transmission and keeping the signal power fluctuation low, the hardware implementation costs will decrease.

- The computational complexity of the inverse transformation stage for a finite-gap signal can be significantly smaller than the vanishing boundary counterpart. The best inverse transformation algorithm for a vanishing signal is the one reported in [73] with $O(N\log^2 N)$ flops while as will be explained in Subsection 2.4.2, the computational complexity of constructing a periodic signal by solving an RHP scales only linearly with the number of time samples. In our method, calculations are done for each time sample independently which makes it possible to parallelise the calculations and decrease the consumed time drastically.

From the functional analysis point of view and in terms of the NS, there are a few differences between the conventional and periodic NFT. Both spectrums consist of a continuous and a discrete part. The discrete part comprises a finite number of isolated complex numbers which for the focusing NLSE are in complex conjugate pairs. The continuous spectrums are where the main difference shows itself. Thanks to the fast decay of the signal in the conventional NFT, the real line is the continuous spectrum. The location of the continuous spectrum is
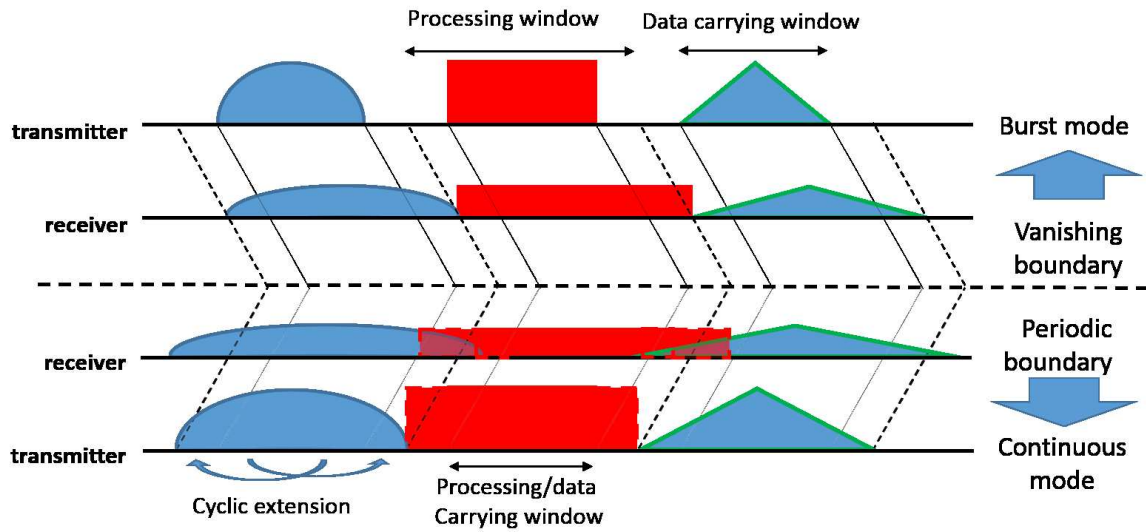
Fig. 3.4 Using cyclic extension, only the original data-bearing part of the signal requires to be processed at the receiver in PNFT.

independent of the location of the eigenvalues in the upper half plane. A finite-gap solution can have multiple segments in its continuous spectrum whose endpoints are the eigenvalues in the discrete spectrum, see Figs. 3.2 and 3.3. As pointed out before, more segments in the continuous spectrum does not mean more degrees of freedom but rather a different configuration of spectral components.

3.4 Periodic NFT

In a communication system, a proper signal with desirable communication properties needs to have at least one (real) degree of freedom to carry data. Keeping everything at this minimum level of requirement, the inverse transformation stage can be reduced to some particular cases where the calculations are straightforward. In this subsection we propose a few approaches to construct a periodic signal and modulate a parameter (invariant or with linear evolution along the fibre). This descriptions here are brief but for the cases for which some simulation results will be presented, more explanations can be found to some length in the next section and appendices.

3.4.1 Analytical formula

The fastest way to construct a periodic signal given its NS is when there is an explicit analytical expression relating the signal in the time domain to its NS through elementary
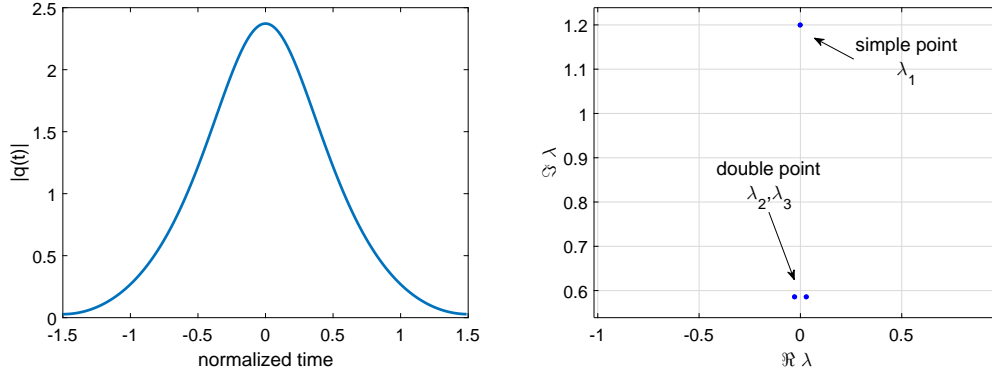
Fig. 3.5 The two-phase signal in Eq. (3.1) with $\lambda_1 = 1.2\,i$ (see the explanations in the text) and the time period $T_0 = 3$ defining the remaining values $\lambda_{2,3}$ (left). The corresponding main spectrum is shown in the right panel.

functions. Such an expression exist only for a few simple and even trivial signals such as a plane wave, a monotonic signal, etc. However, another simple periodic signal which provides one real parameter to modulate after determining the signal duration can be made as below [114]

$$q(t,z) = A \frac{\cosh\left(\phi z - i\sigma\right) + B\cos\left(\xi t - \alpha\right)}{\cosh\phi z + B\cos\left(\xi t - \alpha\right)} e^{iNz}, \tag{3.1}$$

where the parameters are calculated through the following relations

$$A = \Im\lambda_1, \quad N = -4\Re\lambda_1^2 - 2\Im\lambda_1^2, \quad \alpha = \pi,$$

$$B = \frac{\left(|\lambda_3 - \lambda_1| - |\lambda_3 - \lambda_1^*|\right)^2}{|\lambda_3 - \lambda_3^*||\lambda_1 - \lambda_1^*|},$$

$$\phi = -4\Im\left[\left(\lambda_3^* + \Re\lambda_1\right)\sqrt{\left(\lambda_3^* - \lambda_1\right)\left(\lambda_3^* - \lambda_1^*\right)}\right],$$

$$\sigma = -2\Im\ln\left[\frac{\sqrt{\lambda_3^* - \lambda_1^*} - \sqrt{\lambda_3^* - \lambda_1}}{\sqrt{\lambda_3^* - \lambda_1^*} + \sqrt{\lambda_3^* - \lambda_1}}\right],$$

$$\xi = -2\Re\sqrt{\left(\lambda_3^* - \lambda_1\right)\left(\lambda_3^* - \lambda_1^*\right)}, \tag{3.2}$$

where $\Re$ and $\Im$ are real and imaginary part of the argument, respectively. The main spectrum of this signal consists of three points (in the upper half plane) where two of them approach each other and make an almost degenerate point. A degenerate point does not determine the shape or behaviour of the signal but in the case of perturbation can split up into two non-degenerate ones. The new non-degenerate eigenvalues now can change the signal. This
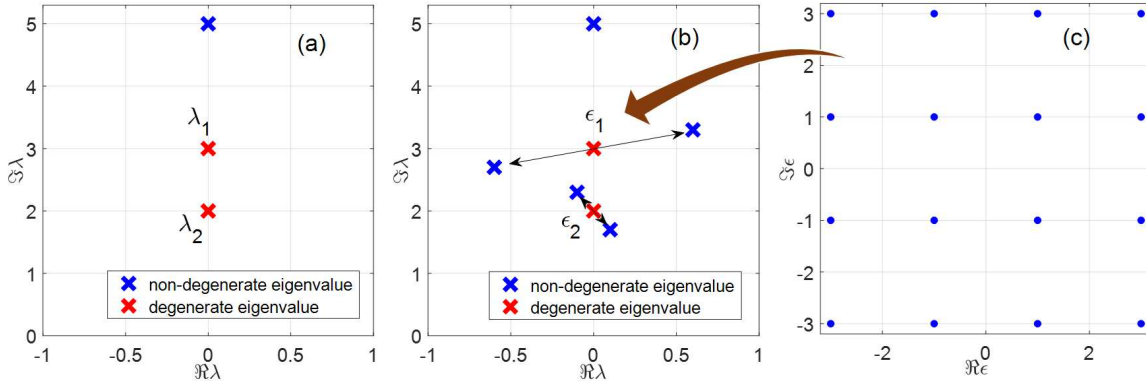
Fig. 3.6 a) The main spectrum of a plane wave with one simple eigenvalue (blue cross) and two degenerate (red cross) ones, b) splitting up the degenerate eigenvalues into two non-degenerate ones, and c) a QAM constellation from which $\varepsilon_{1,2}$ can be drawn.

is in fact, an explanation for the emergence of rogue waves [35, 43, 61]. Later on, we will use this separation to transfer data, see Subsection 3.4.2.

After making sure the signal period is determined, there is only one real parameter to map the data on, $\Im\lambda_1 = -i\lambda_1$ (or $\Im\lambda_3$). An example of such a signal with its NS (main spectrum) is shown in Fig. 3.5. Since this signal can only provide one real degree of freedom, the minimum distance between constellation points is relatively small, leading to a high BER [MK4]. Another limitation of this approach is the lack of control over the signal power.

3.4.2   Perturbed plane wave

The problem of the method explained in Subsection 3.4.1 is that there is not enough degrees of freedom. As mentioned in the previous subsection, more degrees of freedom emerge when a degenerate (double) point splits into two non-degenerate (single) ones. So, what we need is a signal with a degenerate point in its main spectrum and a proper perturbation. The most simple solution to the NLSE is the plane wave with amplitude A in a time window of length T_0. Such a signal has a simple main spectrum consisting of a simple eigenvalue at $\lambda = Ai$ and some double eigenvalues at

$$\lambda_n = \sqrt{\left(\frac{\pi n}{T_0}\right)^2 - A^2}, n < \frac{AT_0}{\pi}, n = 1, 2, \dots . \tag{3.3}$$

Let assume that the signal has two purely imaginary degenerate eigenvalues, $\lambda_{1,2}$ shown in Fig. 3.6a. Introducing a perturbation, each of these two eigenvalues split up into two non-degenerate points, see Fig. 3.6b. This new signal has two complex degrees of freedom in the aperture between these new points, $\varepsilon_{1,2}$. Therefore, one can choose $\varepsilon_{1,2}$ from a QAM

constellation and transfer data. At the receiver, given only one ε is used at the transmitter, the main spectrum is calculated and ε is obtained.

Now that we have chosen the data bearing ε and hence, the two simple eigenvalues, the next step is to find the proper perturbation leading to this NS, or in other words, to perform the inverse transformation. In that regard, one needs to follow the steps explained in Chapter 2 from the given main spectrum which entails calculating the Riemann matrix, the vector of frequencies and other constants [43]. However, at the limit where ε is small, this procedure can be simplified and we have [43, 61]

$$
\begin{aligned}
&\mathbf{V} \approx -2/\pi \sqrt{A^2 + \boldsymbol{\lambda}'}, \quad \mathbf{U} = -2\boldsymbol{\lambda}' \odot \mathbf{V}, \\
&\mathsf{B}_{jj} = \frac{1}{2} + \frac{i}{\pi} \ln\left(\frac{V_j^2}{\varepsilon_j}\right), \quad \mathsf{B}_{lj} = \frac{i}{2\pi} \ln\left(\frac{1 + \lambda_l'\lambda_j' + 0.25 V_l V_j}{1 + \lambda_l'\lambda_j' - 0.25 V_l V_j}\right), \\
&\mathscr{D} + \mathbf{K} - \mathbf{r} = -1 - \frac{i}{\pi} \ln\left[\boldsymbol{\sigma} \odot (\boldsymbol{\lambda}' - \frac{1}{2}\mathbf{V}) \odot (\boldsymbol{\lambda}' + \frac{1}{2}\mathbf{V})\right], \\
&\mathscr{D} + \mathbf{K} = -1 - \frac{i}{\pi} \ln\left[\boldsymbol{\sigma} \odot (\boldsymbol{\lambda}' + \frac{1}{2}\mathbf{V}) \odot (\boldsymbol{\lambda}' + \frac{1}{2}\mathbf{V})\right]
\end{aligned}
\tag{3.4}
$$

where $\boldsymbol{\lambda}'$ is the vector of degenerate eigenvalues of the plane wave with elements λ_j', $\boldsymbol{\varepsilon}$ is the vector of apertures between new eigenvalues, $\boldsymbol{\sigma}$ is the vector of Riemann sheet indices consisting of ± 1s, V_js are elements of $\mathbf{V}$ and $\odot$ is the element-wise multiplication. In fact, for small modulation amplitudes $\boldsymbol{\varepsilon}$, in the first order in $|\varepsilon_j|$ we have

$$
q(t,0) = A + 2 \sum_j |\varepsilon_j| \cos(V_j t + a_j) + O(\varepsilon^2).
\tag{3.5}
$$

for some phases a_j. This signal is close to a more general family of periodic solutions to the focusing NLSE explained in details in appendix D. The proposed signal can indeed provide us with a 2-dimensional constellation and it also has this potential to render a multi-symbol per signal transmission which helps improve the spectral efficiency [MK5, MK6, MK7]. Another advantage of such an approach is that calculating the parameters is fast and there is no need to perform any contour integration. Furthermore, since there are three points in the main spectrum of the received signal, one can design an equaliser using the additional information in the non-data-carrying points to reduce distortion in the nonlinear Fourier domain [83]. However, to increase the minimum distance between constellation points or increase the size of it, it is necessary to enlarge ε which leads to a rise in the approximation error of Eqs. (3.4). Therefore, the bandwidth, signal power and the system performance are limited, more on this limitation in appendix D and [MK6, MK7].

3.4.3 Simplified algebro-geometric approach

To overcome the limits of choosing the discrete spectrum entailed from the approximation used in Eqs. (3.4), we need to define a basis of holomorphic differentials and canonical cycles on the Riemann surface made from the discrete spectrum and calculate the Riemann spectrum using them. Having the latter, the finite-gap solution can be constructed as the ratio of two Riemann theta functions, see Chapter 2. Some provision should be made to assure the periodicity of the solution which enforces some symmetry in the discrete spectrum in simple configurations [115, 116].

One of the drawbacks of this method (shared with the perturbed plane wave approach of Subsection 3.4.2) is that it requires calculating the computationally expensive Riemann theta function, see appendix B. To avoid that, we can split the pertinent Riemann surface into two coverings with simpler architecture and replace the Riemann theta function with Jacobi elliptic functions, for details see [117] and appendix A. This entails a special form of discrete spectrum with three complex conjugate pairs. For this choice of eigenvalues in the discrete spectrum, this setting provides us with one complex parameter in the discrete spectrum and two real initial phases (as the auxiliary spectrum) to convey data in the fibre. The redundancy in the discrete spectrum makes it possible to introduce some equalisation in the nonlinear Fourier domain to rectify the impact of noise. Here we only consider the complex parameter in the discrete spectrum and attribute a QAM symbol to it. Simulation results and more details can be found in Section 4.2 and Subsection 2.4.1.

Another periodic solution to the NLSE, obtained through the algebro-geometric approach but with the Riemann theta function avoided, is a 1-genus solution derived in [118]. Like [117] and Eq. (A.7), this one also presents a closed-form solution using Jacobi elliptic functions. Since this approach of constructing periodic signals is not generalisable to NS with a higher number of cuts, we will not consider them unless for evaluations or proof-of-concept.

3.4.4 1-cut Riemann-Hilbert problem

The configuration of the proposed system in the previous subsection is computationally favourable but is not expandable in a sense that only one QAM symbol can be mapped onto the NS. A more general approach without any constraints and limitations on the configuration of the discrete spectrum is to solve an associate Riemann Hilbert problem numerically. A set of complex conjugate pairs of eigenvalues (and initial phases as the auxiliary spectrum) are given based on which some cuts in the complex plane and jump matrices are defined, see Subsection. 2.4.2. As the simplest non-trivial example, here we consider a 1-cut spectrum giving rise to a 1-gap solution to the NLSE [MK8]. Some provision should be made to make

this finite-gap solution a periodic one which will be explained later. In this setting, two real parameters are available on which a QAM symbol can be mapped. More details on the calculations and definitions can be found in Subsection. 2.4.2. The simulation results for a communication system based on this approach are presented in Section. 4.1.

3.4.5   Multi-cut Riemann-Hilbert problem

The previous subsection proposed a 1-cut solution able to carry one QAM symbol per signal. A natural generalisation of this approach is to use more cuts. Unlike the algebro-geometric approach in which adding another cut leads to an exponential increase in the computational complexity of the transmitter, in using an RHP as the inverse transformation stage, the numerical burden does not change. The only concern is to keep the accuracy, which depends on the number of spectral points defining the cuts, at an acceptable level.

Like other cases, special care should be taken to make the signal periodic. In a multi-cut solution, this entails numerically solving a system of linear equations to have a set of commensurable frequencies, i.e. C_fs in Eqs. 2.42. This puts some limitations on the location of the eigenvalues in the complex plane. In this thesis and the simulations of Chapter 4, we do not consider a multi-cut solution.

Concluding what has been said above, there are a few configurations for applying NFT in fibre-optic communication. So far, in most of these settings, the signal is considered to decay fast with time. Impressive as the results of such a setting are, periodic signals can be advantageous concerning some communication-related characteristics of the signal such as computational complexity of the transmitter and the size of the processing window at the receiver. Like the case for the conventional NFT, PNFT comes in various settings and forms for a communication system. In this chapter, some of these settings are explained but to fully understand such a system, we need to know what the NFT is. This is the subject of the next chapter.

Chapter 4

Simulation results

In this section, simulation results for two systems with signal (2.41) in subsection 2.4.2 and (A.7) in subsection 2.4.1 in a fibre link with ideal Raman amplification and in a link with lumped amplification (using EDFA) are shown. The block diagram of the communication system is depicted in Fig. 4.1. The chosen fibre characteristics are those of a standard single mode fibre: $\alpha = 0.2$ dB/km, $\beta_2 = -20$ ps^2/km and $\gamma = 1.3$ /W/km, and the span length of 80 km is considered. For the links with Raman amplification and EDFA the noise power spectral density, N_{ASE}^R and N_{ASE}^E respectively, are given by the expressions [12]:

$$N_{ASE}^R = \alpha L h \nu_s K_T, \qquad N_{ASE}^E = (e^{\alpha L} - 1) h \nu_s n_{sp}, \qquad (4.1)$$

where L is the fibre length, $h\nu_s$ is the photon energy, $n_{sp} \approx 1$ and $K_T \approx 1.13$ are the amplification parameters. In the simulations, when the lumped amplification (with EDFA) is used, it is necessary to adopt a path-average model for the fibre link to take into account the impact of periodic loss and amplification in the framework of NFT (PNFT). Using such a model, we apply the adjustment explained in [MK10] to optimise the location of amplifiers to improve the performance of an NFT-based communication system. To overcome the inter-symbol interference (ISI) caused by the chromatic dispersion-induced signal broadening, we append the signal with cyclic extension in time domain, Fig. 4.2. Each signal, carrying one QAM symbol, is extended for the value greater than the channel memory calculated from the signal bandwidth $\Delta \nu$ [119]:

$$\mu \approx 2\pi L |\beta_2| \Delta \nu. \qquad (4.2)$$
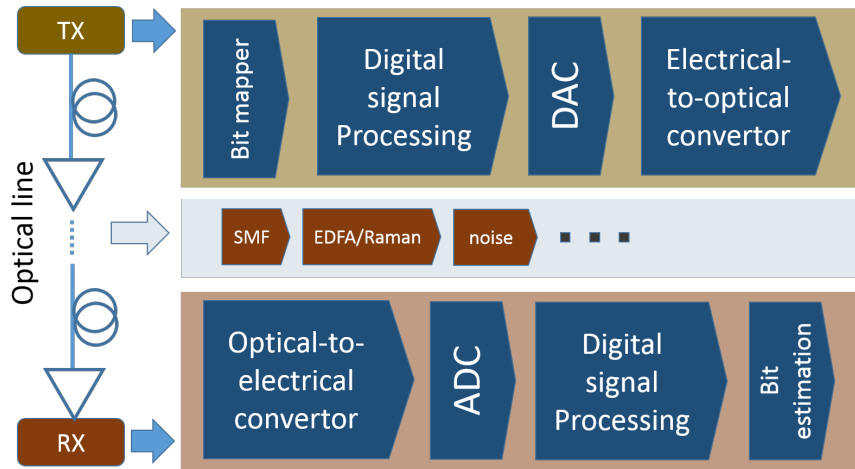
Fig. 4.1 The schematic of a communications system with the DSP processing modules at transmitter and receiver. In particular, for our research the DSP at the transmitter side includes the RHP solution or the reduced algebro-geometric procedure, while at the receiver side the processing is described in Appendix C is used.

4.1 A communication system based on the RHP with a 1-cut spectrum

The simplest non-trivial example for a finite-gap solution is a signal with four eigenvalues in the main spectrum, $\lambda_{0,1}$ and their complex conjugates. A 1-genus solution can provide enough degrees of freedom to first of all, impose periodicity on the signal, and then have control over the time duration (period) of it. In this section, we first present the procedure of constructing a 1-genus solution following the steps of Subsection 2.4.2. After that, the numerical errors coming from the direct and inverse transformation is discussed, and based on these results, the approach to modulate the NS is explained. Using such a signal, a communication system is advised and its performance is evaluated via quality factor, BER and achievable MI.

4.1.1 Constructing the signal

A 1-genus spectrum, with a main spectrum shown in Fig. 4.3, consists of four eigenvalues. Since we only seek solutions to the focusing NLSE, these eigenvalues are two complex conjugate pairs. We consider the cuts as the vertical lines connecting conjugate pairs and define two jump matrices (2.40) as
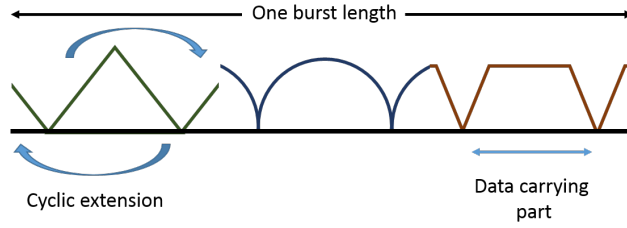
Fig. 4.2 Adding cyclic extension.
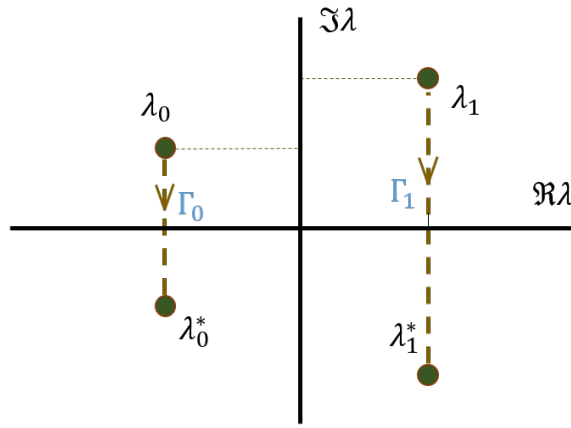
Fig. 4.3 The NS of a 1-gap solution and the defined oriented cuts.

$$\mathbf{J}_0 = \begin{bmatrix} 0 & i \\ i & 0 \end{bmatrix}, \quad \mathbf{J}_1(t,z) = \begin{bmatrix} 0 & ie^{-i(C_1^f t + C_1^g z + \phi_1)} \\ ie^{i(C_1^f t + C_1^g z + \phi_1)} & 0 \end{bmatrix}, \tag{4.3}$$

where C_1^f and C_1^g are obtained from Eq. (2.42) and Eq. (2.43) and ϕ_1 is a free parameter which can also be used to carry data but is set to zero here. The finite-genus solutions are quasi-periodic in t but not, in general, periodic. In order to arrive at periodic NLSE solutions, the spectral data $\{\lambda_j, \lambda_j^*\}_{j=0}^{\mathcal{N}}$ have to satisfy a system of transcendental equations ensuring that all the frequencies C_j^f, $j = 1, \ldots, \mathcal{N}$ supplemented by f_0, see (2.41) and (2.42), are commensurable [44].

For our simple 1-genus case, $\mathcal{N} = 1$, the problem of ensuring periodicity is greatly simplified: it is sufficient to ensure that $f_0 = 0$ in Eq. (2.41), which, in turn, can be done by simultaneously shifting all the spectral data points $\{\lambda_j\}_{j=0}^{\mathcal{N}}$ along the real axis. This a direct result of setting $f_0 = 0$ using Eq. (2.44) and finding C_j^fs using Eqs. (2.42). Thus a preliminary step in the construction of a genus-1 solution consists in the adjustment of the

main spectrum: given $\{\hat{\lambda}_j\}_{j=0}^1$, the real-valued shift is computed as follows:

$$\hat{f}_0 = \frac{\int_{\hat{\Gamma}_1} \frac{\xi d\xi}{\hat{w}(\xi)}}{\int_{\hat{\Gamma}_1} \frac{d\xi}{\hat{w}(\xi)}} - \frac{1}{2}\sum_{j=0}^1 (\hat{\lambda}_j + \hat{\lambda}_j^*) \tag{4.4}$$

with $\hat{w}(\xi) = \hat{w}_+(\xi)$, where $\hat{w}_+(\xi)$ is the limiting value from the $(+)$ side of $\hat{\Gamma}_1$ (according to the orientation shown in Fig. 4.3) of the function $\hat{w}(\lambda) = \sqrt{\prod_{j=0}^1 (\lambda - \hat{\lambda}_j)(\lambda - \hat{\lambda}_j^*)}$ defined with the cuts $\hat{\Gamma}_{0,1}$ along the arcs $(\hat{\lambda}_{0,1}, \hat{\lambda}_{0,1}^*)$, where the branch is fixed by the condition $\hat{w}(\lambda) \sim \lambda^2$ as $\lambda \to \infty$. Then the new points λ_j, corresponding to a periodic genus-1 solution with $f_0 = 0$ (see (2.41)), are defined by: $\lambda_j = \hat{\lambda}_j + \hat{f}_0$. Now, using `RHSolve` to find a matrix-valued function **M** in the RHP (2.39) analytic on $\mathbb{C}\setminus\Gamma$ where $\Gamma = \{\Gamma_0 \cup \Gamma_1\}$ and by taking into account the asymptotic behaviour of **M**, we can find $\mathbf{M}_1$ where

$$\mathbf{M}(t,z,\lambda) = \mathbf{I} + \mathbf{M}_1(t,z)\lambda^{-1} + O\left(\lambda^{-2}\right) \text{ as } \lambda \to \infty.$$

The solution is then retrieved easily from

$$q(t,z) = 2i(\mathbf{M}_1)_{1,2}(t,z).$$

4.1.2 Numerical accuracy of the direct and inverse transformation

There are two sources of numerical error in the PNFT formalism with different dependence on signal and algorithm characteristics; inverse transformation which here shows itself in calculating integrals and solving the RHP, and the direct transformation which in our work is performed by an Ablowitz-Ladik algorithm. While the former can be controlled via changing the spectral resolution ($\Delta\lambda$) as the step size of the points defining the contours, the latter is directly related to the number of signal samples in the time domain. To show this, the back-to-back (B2B) error of the system is calculated for different number of points in the spectral domain and time domain and is shown in Fig. 4.4. In this figure, the chosen eigenvalues are $\pm 1.4 + 0.4i$ before their real part being shifted to make a periodic solution. Error is defined as the sum of the distances of expected points and the numerically calculated ones.

4.1.3 Choosing eigenvalues

In this setting, there are four parameters among which two are used to set the period of the signal and the other two are the real degrees of freedom. In this subsection, we discuss
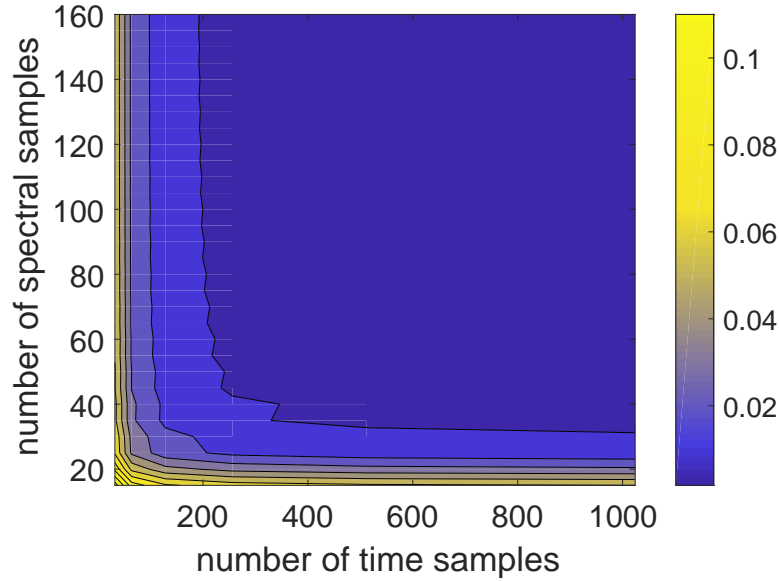
Fig. 4.4 The numerical error in a B2B scenario as a function of the number of time samples, N, and the number of spectral samples, n.

which two of these to use to modulate data. In choosing the eigenvalues we consider a few caveats; first, the numerical errors and the impact of the ASE noise depend on the location of the points. Second, as we intend to control the signal power and signal duration, some constraints should be taken into account.

The signal bandwidth and power depend on the location of the eigenvalues as is shown in Fig. 4.5. From this figure one can conclude that the real and imaginary parts of the eigenvalues determine the signal bandwidth and power, respectively. Therefore, since the numerical errors depend on the location of the eigenvalues (see Fig. 4.6), the system is likely to deliver different performances for different signal powers and bandwidths. For two cases where $\Im\lambda_0 = \Im\lambda_1$ and $\Im\lambda_0 = 0.7$, the numerical error against $\Im\lambda_1$ and $\Delta\Re(\lambda_0 - \lambda_1)$ is shown in Fig. 4.6. The imaginary part of the eigenvalues (directly related to the signal power) has the dominant role in changing the numerical errors. In Fig. 4.6b, and where the difference between the real parts are small, it seems like the error depends on the real part of the eigenvalues as well. However, this can be explained by noting that at small $\Delta\Re(\lambda_0 - \lambda_1)$ the signal period becomes larger and the time resolution drops, hence, the numerical accuracy deteriorates. Therefore, as long as the $\Delta\Re(\lambda_0 - \lambda_1)$ or N are large enough, it is the imaginary parts of the eigenvalues who determine the signal power and the numerical error. On top of these, the one-to-one relation between the NS and the signal implies that the signal power is only determined by the location of the eigenvalues. Therefore, to have a communication system with various signal powers (to find the optimum launch power), those two parameters

Fig. 4.5 a) signal power (a.u. logarithmic scale), and b) signal bandwidth (a.u. logarithmic scale) verses the difference between the real parts of the eigenvalues and the imaginary part of the eigenvalues when $\Im\lambda_0 = \Im\lambda_1$, and c) signal power (a.u. logarithmic scale), and d) signal bandwidth (a.u. logarithmic scale) verses the difference between the real parts of the eigenvalues and the imaginary part of the eigenvalues when $\Im\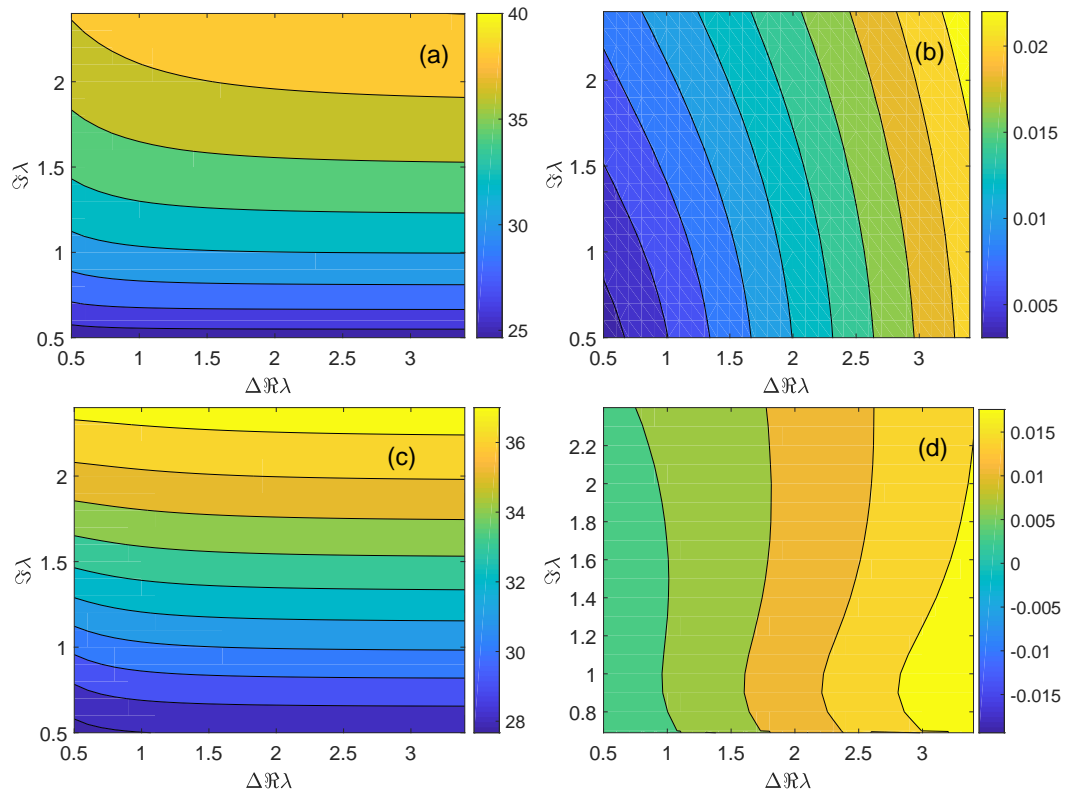lambda_0 = 0.7$. $\Delta\Re\lambda = |\Re\lambda_1 - \Re\lambda_0|$ and $\Im\lambda$ in the vertical axis is $\Im\lambda_1$.
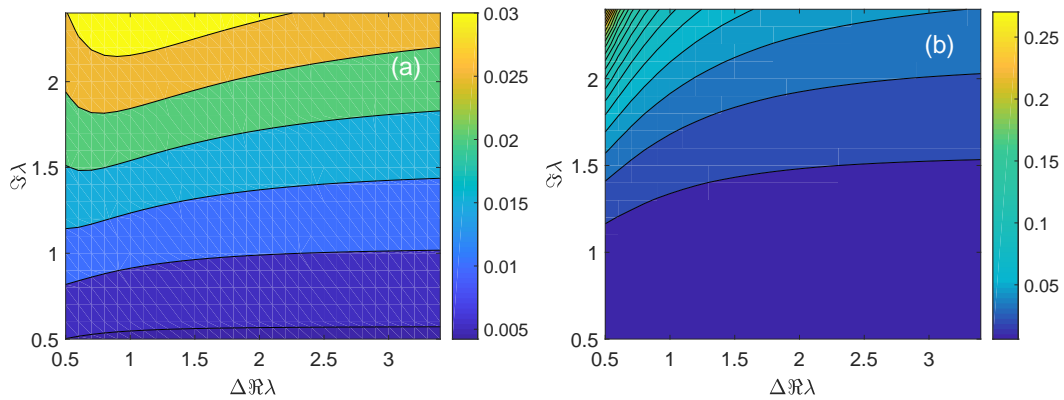
Fig. 4.6 The numerical error as the absolute difference between the expected and calculated eigenvalues, in a B2B scenario showing the influence of the imaginary parts of the eigenvalues (signal power) on the performance when a) $\Im\lambda_0 = \Im\lambda_1$, and b) $\Im\lambda_0 = 0.7$. $\Delta\Re\lambda = |\Re\lambda_1 - \Re\lambda_0|$ and $\Im\lambda$ in the vertical axis is $\Im\lambda_1$

should be chosen to carry data that make it possible to change the signal power while keeping other signal characteristics fixed. The best choice seems to be the imaginary parts of the eigenvalues.

A complex QAM symbol, drawn randomly according to the data, makes two imaginary parts of the eigenvalues. Based on these imaginary parts and taking into account the signal period (and bandwidth), the real parts of the eigenvalues are determined. The imaginary part of the points plays an insignificant role in determining the signal period, hence, keeping the signal period for different imaginary parts of the eigenvalues leads to almost identical real parts.

An advantage of choosing the imaginary parts of the eigenvalues to map the QAM symbols on is that the constellation made in this way has a special structure. Thanks to the dependence of the signal power to the imaginary part of the eigenvalues, the bottom left point in the constellation attributes to a signal with the lowest power. As we move from this point to the right or up, the signal power increases. Since the fibre link contains some noise-producing components such as amplifiers, there is a lower bound on the signal power below which the receiver can not distinguish a data-carrying eigenvalue from a spurious one coming from noise. Therefore, To increase the minimum distance between the constellation points (in order to decrease the BER), one can only add points with signals with higher powers. Whether this expansion of the constellation leads to a better performance needs to be investigated for the numerical errors and other imperfections of the system have a nonlinear relation with the signal power as well. At the receiver, the main spectrum of the signal is calculated which consists of two eigenvalues, only to recover the QAM symbol made by the

imaginary parts of the calculated eigenvalues. These two eigenvalues have different real parts (in this example the same value with opposite signs) and easily discernible.

4.1.4   Transmission simulation results

In our simulations, the symbols are transmitted in "bursts" of $4M$ samples, where M is the size of the constellation. The burst is formed as follows: several signals, modulated using random data, are cyclically extended and put together. At the receiver, a simple phase rotation of the constellation is used to reverse the residual impact of ISI when the broadening is slightly larger than the cyclic extension. Fig. 4.7c depicts the Q^2-factor calculated from the error vector magnitude (EVM) for four systems with different constellation sizes in a 880 km link. The Q^2-factor is averaged over the number of symbols in each burst and over 2^8 runs. The symbol rate is 0.8 GSym/s; it can be increased by increasing the signal bandwidth (changing the real part of the eigenvalues). Fig. 4.7 shows that there is an optimum power at which the Q^2-factor is maximum. One reason for a decline in the system performance at higher powers is the dependence of numerical accuracy on power, as is evident from Fig. 4.6. Increasing the sampling rate and the accuracy of the arcs discretisation can improve the performance. This is shown, for a system with oversampling factors $8 - 64$, which are much smaller than the one used to obtain the results in Fig. 4.7, and for a 2 Gsym/s communication up to 1000 km in Fig. 4.8. As can be seen in Fig. 4.8, the improvement obtained from increasing the number of samples diminishes for larger figures which conforms to the results shown in Fig. 4.4.

Had the governing system been an integrable one, changing the fibre parameters, the Kerr nonlinearity parameter, γ, among them, would not have changed. However, due to the imperfections of the NLSE model coming from a periodic loss and gain and also the impact of ASE noise in disturbing the integrability, one can still expect the system performance to deteriorate for higher nonlinearity. This is shown in Fig. 4.9. In Fig. 4.9 increasing γ for a 4QAM system with a data-rate of 0.8 GSym/s in a 880 km link (also shown in Fig. 4.7) leads to a slight reduction in the maximum achievable Q^2-factor. The received constellations at optimum power are shown in Fig. 4.7 a, b, d, and e. As explained before, the axes of these scatter plots are the imaginary parts of the two eigenvalues in the discrete (main) spectrum of the received signal, $\Im\lambda_0$ and $\Im\lambda_1$.

Fig. 4.10c portrays the dependency of the Q^2-factor on the link length and the impact of the particular amplification type: ideal Raman and EDFA. The close-to-ideal Raman amplification can be realised with a reasonable degree of accuracy through the second-order Raman pump [120]. In this figure, the signal power was set to -5 dBm, and the symbol rate is 1 GSym/s. The received constellation is depicted at distances $z = 580$ km and $z = 1120$ km.
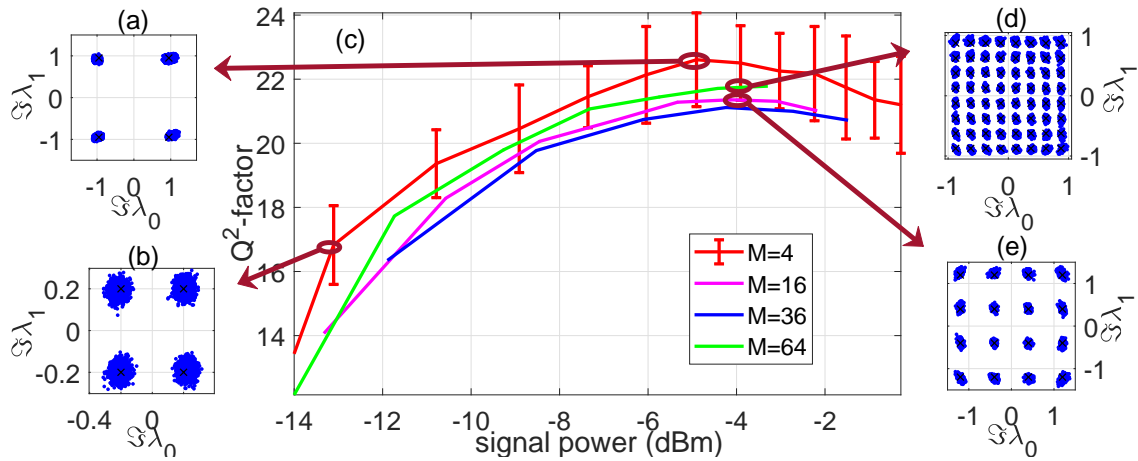
Fig. 4.7 a) The 4-QAM receiver constellation at the optimum power, b) the 4-QAM receiver constellation at power $P = -13.1$ dBm, c) Q^2-factor for a 0.8 Gsym/s signal in a 880 km link with EDFA and ASE noise for various sizes of constellation, d) The 64-QAM, and e) the 16-QAM receiver constellation at the optimum power where the signal bandwidth is $BW = 4.8$ GHz.
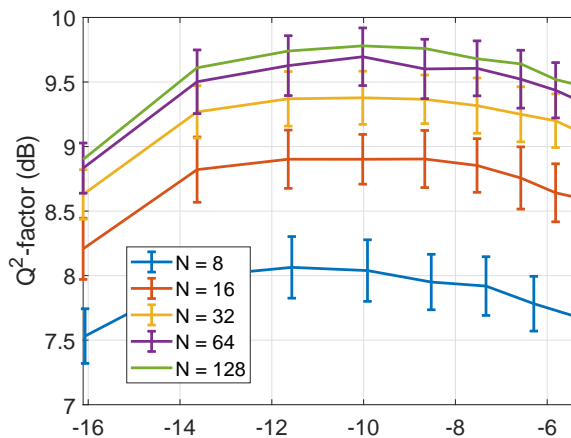
Fig. 4.8 The impact of changing the number of time samples, N, in the overall performance of a 2 Gsym/s system in a 1000 km link, showing that it is possible to improve the efficiency by increasing the oversampling ratio at the expense of higher computational complexity.
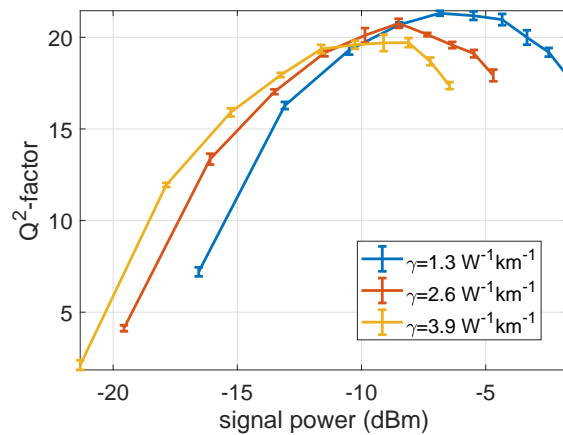
Fig. 4.9 The impact of changing the nonlinearity, γ in the overall performance of a 0.8 Gsym/s system in a 880 km link. This graph shows that although in theory the performance of the NFT-based communication is independent of the link parameters, fibre loss and additive ASE noise influence the integrability of the system and cause the the optimum point to lower as the nonlinearity parameter grows.

We see that the system performance deteriorates quickly at long distances due to the ISI caused by the limited cyclic prefix duration. The performance can be improved by enlarging the duration of cyclic prefix.

Another important object in communication systems' design is the probability density function (PDF) of the received symbols. Finding the PDF of the received symbols given the transmitted ones is necessary to find the MI, channel capacity, and to design optimum coding and detection strategies. Since there is still a lack of a mathematical understanding of the behaviour of the PNFT spectrum quantities under the influence of optical noise [MK11], here we rely on the empirical PDF coming from the histogram of the received symbols. For a 1024-QAM signal, a 2D histogram of the received QAM symbols is plotted in Fig. 4.11 by using 2^9 transmissions of $4*1024$ symbols. The almost circular shapes in that figure indicate that the received distribution is close to the circular Gaussian one where the real and imaginary parts are almost independent. However, as it commonly occurs in other communication systems based on the NFT [24], the characteristics of this Gaussian PDF differ for symbols with different signal power. This can be seen in Figs. 4.11b and c where the histogram of the small- and large-power parts of the constellation are shown. From this figure, an increase in the standard deviation is apparent for the symbols (constellation points) attributed to higher powers. These results are in agreement with the earlier ones reported in [MK11] for a PNFT system with different processing type. This observation suggests a
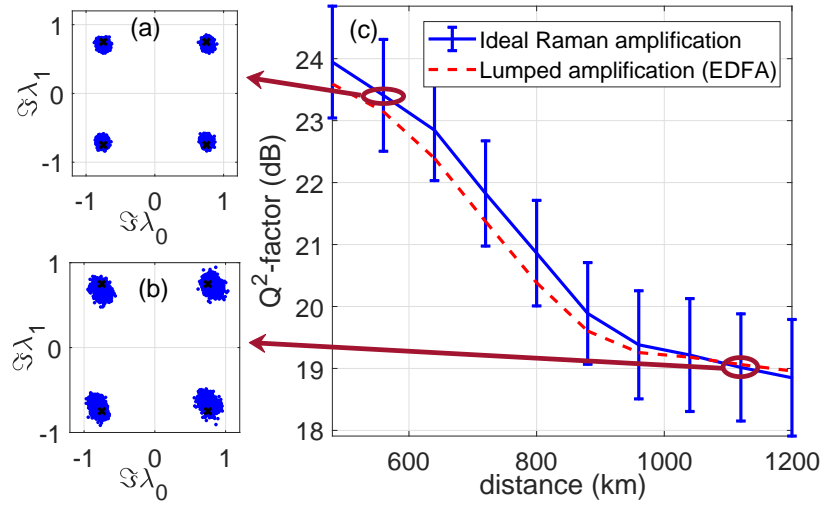
Fig. 4.10 a) The received constellation at 580 km, b) the received constellation at 1120 km, and c) Q^2-factor for a 4-QAM 1 Gsym/s signal with -5 dBm power against distance. We used ideal Raman amplification (blue) and EDFA (red), $L_{span} = 80$ km, adding ASE noise.

Gaussian mixture model for the received points $\hat{\lambda}$, the PDF of which we can write down as

$$P(\hat{\lambda}) = \sum_{\lambda \in \Lambda} p_\lambda N(\hat{\lambda}; \lambda, \sigma_\lambda^2), \tag{4.5}$$

where Λ is the set of points in the constellation, p_λ is a probability function over Λ, and $N(\hat{\lambda}; \lambda, \sigma_\lambda^2)$ denotes a multivariate normal Gaussian distribution for the complex random variable $\hat{\lambda}$ with mean λ and a diagonal covariance matrix $\sigma_\lambda^2 I_2$.

One of the most important metrics of a communication system performance is the MI of the transmitted and received symbols, here λ and $\hat{\lambda}$, respectively. Fig. 4.12 demonstrates the behaviour of the achievable MI as a functions of the link length. This figure, when compared with other discrete NFT spectrum communications systems such as eigenvalue and norming constants-based communications [82], indicates the potential of the PNFT-based systems in rendering a high spectral efficiency.

4.2 A communication system based on the algebro-geometric approach

The algebro-geometric approach, explained in Subsection 2.4.1, suffers from the high computational complexity of evaluating the multi-dimensional Riemann theta function (2.30), see appendix B. In this section, an approach to reduce the complexity is suggested while more details are left to appendix A.
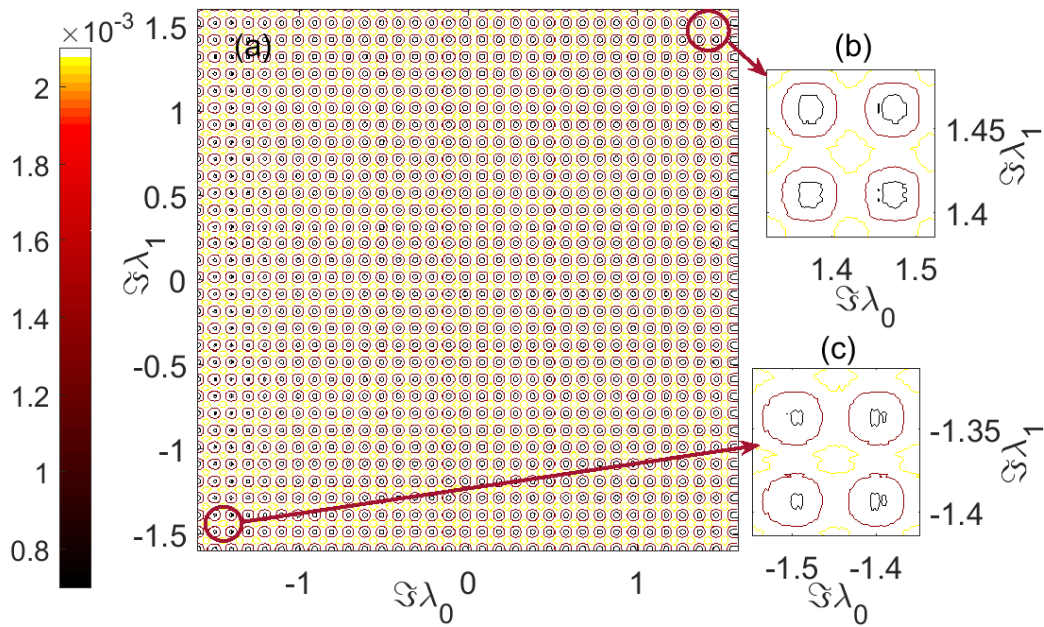
Fig. 4.11 a) A 2D histogram of the received constellation of a 1024-QAM system at distance $z = 680$ km and signal power $P = -5$ dBm, and a close up for two parts of the constellation attributed to b) the highest and c) the lowest signal power.
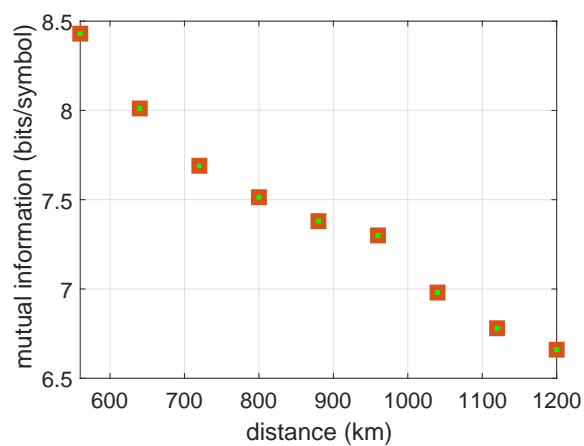
Fig. 4.12 The achievable mutual information versus the link length.
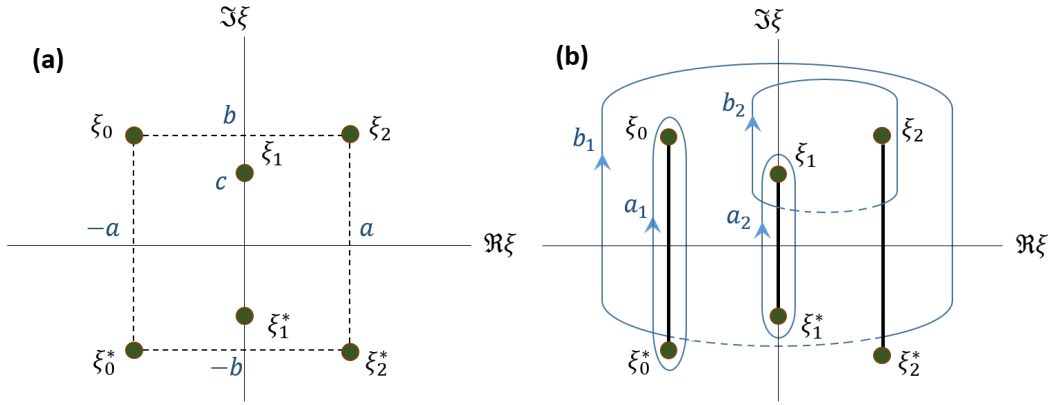
Fig. 4.13 A Riemann surface of genus 2 with three points of auxiliary spectrum.

4.2.1 Constructing the signal

For some especial cases of the NS it is possible to circumvent evaluating the Riemann theta function and instead calculate simple Jacobi elliptic series. The 2-cut spectrum is shown in Fig. 4.13 which consists of three eigenvalues $\{\xi_0, \xi_1, \xi_2\} = \{-a+bi, ci, a+bi\}$ and their complex conjugates. To construct the signal with this NS we need to calculate the pertinent contour integrals explained in Chapter 2 on a basis for canonical cycles which are shown in Fig. 4.13b. Detail of the calculation and the way one can circumvent evaluating the computationally heavy Riemann theta function is elucidated in appendix A. There are three free parameters, a, b and c. The symmetry in the spectrum guarantees periodicity and the signal period is mainly determined by the real parts of the points in the main spectrum. Although changing the imaginary parts can only slightly vary the period, we numerically find the best value for c to set the period of the signal to the exact predetermined value. For a QAM symbol, ξ_2 and consequently ξ_0 is modulated and c is calculated so that the signal period is the predetermined value. This is numerically done by integrating and calculating the frequency $\frac{2\pi}{A_-}$ in (A.5).

The procedure of constructing the burst at the receiver is similar to the one explained in Subsection 4.1. At the receiver, the NS is calculated and a and b are retrieved.

4.2.2 Numerical accuracy of the direct and inverse transformation

The numerical accuracy of performing the inverse PNFT (as explained above) and direct PNFT [49] depends on the number of time samples, signal power, and the particular location of eigenvalues. The B2B error without any random noise shows the dependence of the numerical accuracy on the location of eigenvalues, Fig. 4.14. This error is defined as the Euclidean distance between the transmitted and received eigenvalue. Simulation results show

that the B2B error and the error at the receiver after a noisy transmission have similar patterns with regard to their dependence on the eigenvalues location, which yet again, verifies that the main contributor to the overall error is the numerical one for the PNFT.

As for the signal in Section 4.1, here, a Gaussian mixture model (4.5) of the channel is considered, where the standard deviation, σ_λ, is estimated from the received points. As mentioned before, σ_λ has the same pattern as the B2B error shown in Fig. 4.14, which in turn, depicts a considerable variation between different points. This in fact, suggests that we can apply a non-uniform probability distribution for the transmitted symbols, in which the constellation points that contribute more to the overall error are used less frequently. Note that, there is a trade-off here; exclusion of the eigenvalues with high contribution to EVM leads to a better Q^2-factor but reduces the MI. Hence, keeping the constellation size, M, and the main spectrum, Λ, fixed, we optimise P_λ in (4.5) to have the maximum MI, $I(\hat{\lambda}, \lambda)$. This is numerically done for each signal power and link length.

4.2.3   Transmission simulation results

In the first set of simulations, entailed from the chosen eigenvalue set, the signal power is $P = -2.7$ dBm. According to Fig. 4.15, P can be controlled through changing the location of eigenvalues, for example by increasing $\Im\lambda$ while keeping the signal bandwidth fixed. Considering the signal power (Fig. 4.15 in arbitrary units for different locations of the eigenvalues) along with the B2B error (Fig. 4.14), one can realise that the B2B error does not directly depend on the signal power. Therefore, the average launch power does not vary with uniform or non-uniform symbol allocation if the distribution is determined with respect to the B2B error. According to each symbol, a periodic signal is produced following the steps in [117] and appendix A, and cyclically extended to the size of chromatic dispersion memory. The burst of symbols then is formed by packing several signals and sent to the link with lumped amplification and ASE noise.

At the receiver, the main spectrum of the signal is calculated by the PNFT [49] and the transmitted data is retrieved. A simple blind phase estimation is used to equalise some distortions which are mainly coming from signal broadening and insufficient cyclic prefix. The length of cyclic prefix is fixed to the signal broadening after 1000 km. An example of the receiver constellation of size $M = 64$ at $z = 1120$ km with signal power $P = -2.72$ dBm is shown in Fig. 4.17 in which the dependence of the noise variance on the location of the eigenvalue is evident. The significant difference in the contribution of each eigenvalue in the overall BER suggests implementing the probability shaping technique. Fig. 4.16 shows the Q^2-factor calculated from the EVM and the BER (directly calculated from counting the mismatches between the transmitter and receiver symbol streams) against different
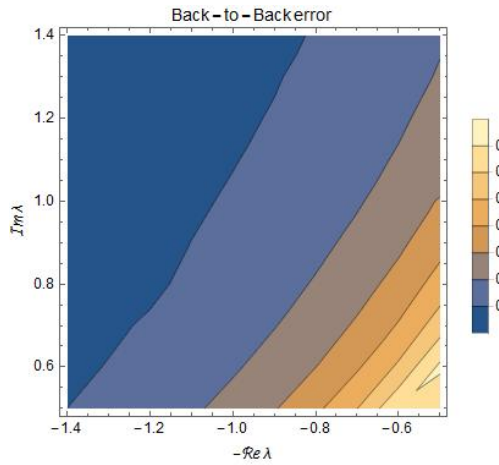
Fig. 4.14 B2B error as the average of the absolute difference between the expected and calculated eigenvalues, for different locations of the eigenvalue with $\Re\lambda = a$, $\Im\lambda = b$ and a, b defined in Fig. 4.13.
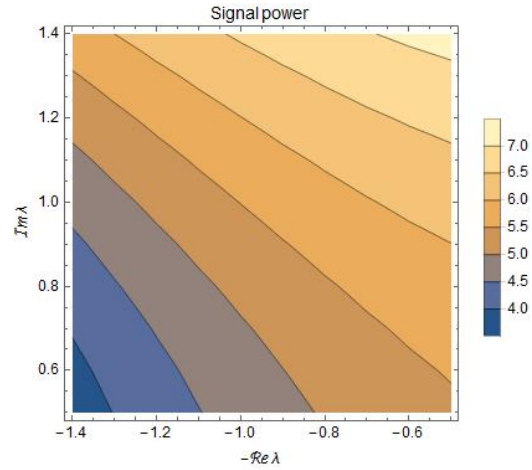
Fig. 4.15 Signal power for different locations of the eigenvalue with $\Re\lambda=a$, $\Im\lambda=b$ and a, b defined in Fig. 4.13.
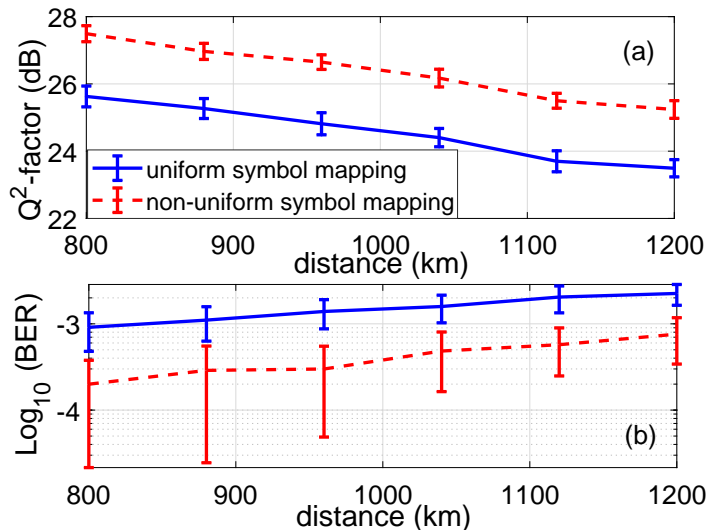
Fig. 4.16 a) the Q^2-factor calculated from the EVM, and b) directly calculated BER against distance for 64-QAM with uniform and non-uniform transmitter symbol probability with average $P = -2.72$ dBm signal power.
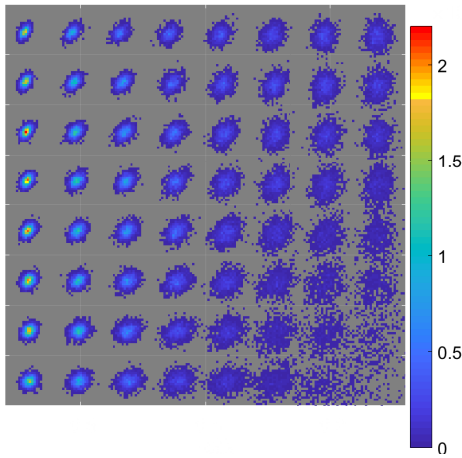
Fig. 4.17 The received constellation at $z = 1120$ km for a 64-QAM signal with power $P = -2.72$ dBm.
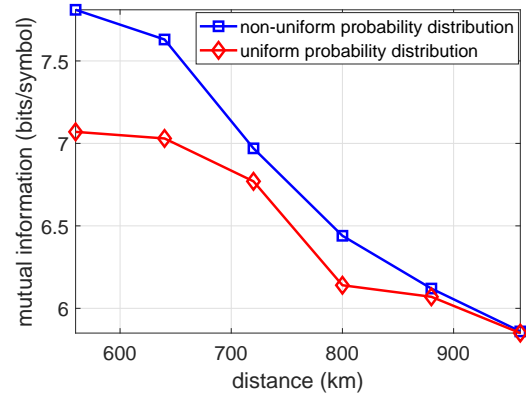
Fig. 4.18 Achievable mutual information versus distance for a signal with average power of $P = -2.72$ dBm with uniform and non-uniform probability distribution of the transmitted symbols.

propagation distances. From this figure, one can compare the results when a uniform and non-uniform distribution for the transmitted symbols is considered. These results are calculated for 200 transmissions of symbol bursts, each having the length $12 \times M$, where M is the size of constellation. As it can be seen in Fig. 4.16, a considerable improvement of 2 dB in the Q^2-factor can be gained by the probabilistic shaping of constellation. However, a more informative figure is the maximum achievable error-free MI or spectral efficiency for various link lengths. Thanks to the used exact inverse PNFT, a full control over the signal power and time duration makes it possible to optimise the signal in terms of its parameters, and to find the maximum MI. The achievable MI in bits per symbol for a discrete-modulation NFT system with one eigenvalue is presented in Fig. 4.18. It is worth noting that these results are to be compared with other discrete NFT communication systems such as eigenvalue communication in which the throughput of the system is smaller when compared to a continuous spectrum modulation [82].

In this chapter, a general communication based on the PNFT, whose foundation is laid in previous chapters, has been implemented for two simple but non-trivial cases. Simulation results for these two PNFT-based communication systems are shown and the system performance for different signal powers, distance and number of samples is illustrated. Combining PNFT with other methods of overcoming fibre distortions such as probabilistic shaping, communication-related measures of the system are investigated and the results are depicted. From what presented, one can conclude that the PNFT can increase the MI and decrease the computational complexity of an NFT-based communication system. Although the simulation results show the competence of a PNFT system, it still suffers from a set of drawbacks such

as small time-bandwidth product and small number of symbols per signal. The letter can be resolved using the whole NS (and not only the main spectrum) to carry data and also by using higher order main spectrum.

Chapter 5

Discussion, future works and conclusion

Fibre-optic communication forms the backbone of the global data network and is under the pressure of carrying more data on a daily basis to the extent that a capacity crunch is predicted to happen in the near future. More than any time, it is necessary to investigate new methods of transferring information to use the current network of fibres to its fullest. Over the past decades many approached have been taken to increase data-rate; WDM, SDM, PDM, etc. all with their up and downsides. Many DSP-based solutions have been tried to overcome signal impairments caused by fibre, primarily the new phenomenon, Kerr nonlinearity. Nonlinearity is what distinguishes the fibre channel from the widely-used linear ones such as wireless and cooper. What had been designed to mitigate the detrimental impacts of the linear channel needs to be revisited to accommodate to the new fibre channel. This, of course, is not an easy task and requires considering the physics behind the fibre distortions, governed by the celebrated NLSE. Furthermore, with a new insight, in which this nonlinearity and other channel effects are not perceived as detrimental effects but some system parameters, it is possible to design communication systems tailored to the characteristics of the medium.

Soliton communication was the first attempt to design a communication system based on the traits of the fibre channel. In a soliton communication, a signal which retains its form periodically is used to transfer data. The concept of a soliton-based system can be generalised to a more inclusive set of parameters which show the underlying invariance of the NLSE. This set of parameters is called the nonlinear spectrum in the nonlinear Fourier transform paradigm. Having a trivial evolution in the fibre, the NS can be used to convey data from the transmitter to the receiver as it has been passing through a linear channel. This makes it possible to accommodate various algorithms that are designed over the years for linear channels. In a communication system that uses the NS to transfer data, a signal is constructed from the data-carrying NS. The current available mathematical tools allow us to make up such a signal with some particular boundary conditions; with vanishing boundaries

or quasi-periodic. Using signals with vanishing boundary condition has been the subject to many studies over the mast few years, and its performance has been evaluated experimentally showing its potential to overcome some of the fibre difficulties.

However, using periodic signals can be advantageous in some respects such as the size of the processing window at the receiver, controllable signal duration at the transmitter and smaller computational complexity for the inverse transformation stage. Using NFT, the processing window at the receiver is only of the size of one period of the signal as opposed to the vanishing boundary signals where this window is as large as the broadened signal length. This can make a substantial difference especially in high data-rate communications where the channel memory is large.

Therefore, to investigate the potentials of a fibre-optic communication system based on the PNFT, in this thesis:

- The mathematical foundation of the inverse transformation for a finite-gap solution to the NLSE in an Algebro-geometric approach is explained in a detailed and step-by-step manner,

- Several solutions to construct a periodic signal from a given main spectrum to replace the inverse transformation stage is proposed. At first, a simple system made up by a signal with analytically known NS is suggested. This system provides only a one-dimensional constellation, and thus, has somewhat limited performance. Further, this system is developed into a more advanced case when a two-dimensional constellation is available. This system involves a perturbation of a plane wave and renders one complex degree of freedom for modulation. However, it has also revealed some limitations related to the size of the constellation, bandwidth, and signal power,

- A reduced Algebro-geometric approach to construct a periodic signal with one free complex number in its main spectrum to modulate is proposed. This approach leads to a decrease in the computational complexity of the inverse transformation stage by avoiding numerical evaluation of the Riemann theta function,

- A general Riemann-Hilbert problem-based approach to perform the inverse transformation is adopted to circumvent numerical evaluation of the Riemann theta function. This method is not only an alternative to the previous reduced Algebro-geometric approach but also can be generalised to signals with a higher order main spectrum,

- Numerical routines of calculating the NS of a periodic signal are compared regarding their accuracy and runtime,

- Simulation results have been carried out to investigate the efficiency and performance of the proposed communication systems and find their achievable mutual information by implementing some known algorithms in linear communication systems.

One downside for the periodic NFT is its demanding mathematics and a lack of a generic numerical tool to perform the inverse transformation stage. Using the available numerical routines, a drawback of such a system is still its poor numerical accuracy which entails a large number of temporal samples. Although the computational complexity of the inverse transformation in our proposed PNFT-based system through an RHP scales linearly with the number of samples, $O(N)$, its factor is still significant and entails solving two linear systems of equations. The number of samples in time is limited by the hardware capabilities at the receiver and transmitter and can increase as better analogue-to-digital converters are available. However, more should be done to improve the numerical routines of calculating the NFT especially in high powers where the numerical errors rise fast.

Other limitations of the proposed systems are their small data-rate mainly due to the small number of symbols carried by each produced signal. This number can increase by working with signals whose NS has more than two cuts. This can be achieved in particular by using the RHP approach. One of the difficulties of using the RHP method to construct a signal is the fact that the periodicity should be maintained and the signal period has to be controllable. This is an essential stage in designing a PNFT communication system which can be numerically done by adjusting the location of the main spectrum. To arrive at a more general approach of setting the signal period, more mathematical work should be done. The number of symbols per signal can also be increased by utilising the whole NS and multiplexing the continuous spectrum. Thanks to the general formalism of the RHP-based inverse transformation, the NS can acquire more than one continuous spectrum. This can be used as a nonlinear frequency division multiplexing scheme with each part of the continuous spectrum dedicated to one user. This is left for future investigations.

In addition to the relatively high numerical error of NFT calculations, an NFT-based communication is vulnerable to some fibre impairments that make the underlying nonlinear dynamics of the system a non-integrable one. Fibre loss is one of these problems which provides a periodic gain and loss profile for the signal as it travels through the link. By utilising second-order two-pump Raman amplification this problem can be alleviated, to some extent, but it still adds some model error to the system. Another solution for links with EDFA is to replace the real NLSE, modelling the periodic loss and gain, with a path-averaged lossless NLSE. This solution also still introduces some model error to the calculations. Another problem of this kind is the inevitable ASE noise; noise can not only damage the quality of the received signal, but also makes the system non-integrable. This may lead to

a greater detrimental impact on the system performance showing itself in the form of an enhanced noise.

There are many open questions and future directions for research on using NFT in fibre-optic communication. One missing stage in NFT-based systems is the signal processing in the nonlinear Fourier domain besides the phase rotation in the vanishing NFT and linear back-propagation in the PNFT. Implementing multi-cut solutions can provide the possibility to introduce coding schemes inside the nonlinear Fourier domain or design equalisers at the receiver.

Another important question is about the capacity of the fibre channel. Since NFT is able to solve the NLSE, it may be useful in finding the statistical characteristics of noise and distortion in fibre, which is the first stage of calculating its capacity. Some works have been conducted on this topic, but more should be done.

In conclusion, conventional NFT has shown impressive results in recent years and presented itself as a candidate to solve some of the major difficulties of fibre-optic communication. This method, nevertheless, has its own drawbacks which can, to some extent, be rectified by considering periodic NFT. In this thesis, some PNFT-based systems are proposed, and their performance is investigated through simulations. Based on these simulations, it is made evident that the PNFT has the potential to improve the throughput of an NFT-based fibre-optic communication system. NFT's performance is still, however, far from the best state-of-the-art systems. It seems that more time and research is needed in designing the numerical methods to carry out the NFT calculations and to understand the characteristics of noise in the nonlinear Fourier domain.

References

[1] E. Agrell, M. Karlsson, A. Chraplyvy, D. Richardson, P. Krummrich, P. Winzer, K. Roberts, J. Fischer, S. Savory, B. Eggleton, et al. Roadmap of optical communications. *Journal of Optics*, 18(6):063002, 2016.

[2] R. Mears, L. Reekie, I. Jauncey, and D. Payne. Low-noise erbium-doped fibre amplifier operating at 1.54 μm. *Electronics Letters*, 23(19):1026–1028, 1987.

[3] C. Fludger, T. Duthel, D. Van den Borne, C. Schulien, E. Schmidt, T. Wuth, J. Geyer, E. De Man, G. Khoe, and H. de Waardt. Coherent equalization and polmux-rz-dqpsk for robust 100-ge transmission. *Journal of lightwave technology*, 26(1):64–72, 2008.

[4] P. Winzer. High-spectral-efficiency optical modulation formats. *Journal of Lightwave Technology*, 30(24):3824–3835, 2012.

[5] P. Winzer, D. Neilson, and A. Chraplyvy. Fiber-optic transmission and networking: the previous 20 and the next 20 years. *Optics express*, 26(18):24190–24239, 2018.

[6] S. Hranilovic and F. Kschischang. Optical intensity-modulated direct detection channels: signal space and lattice codes. *IEEE Transactions on Information Theory*, 49(6): 1385–1399, 2003.

[7] B. Zhu, T. Taunay, M. Fishteyn, X. Liu, S. Chandrasekhar, M. Yan, J. Fini, E. Monberg, and F. Dimarcello. 112-tb/s space-division multiplexed dwdm transmission with 14-b/s/hz aggregate spectral efficiency over a 76.8-km seven-core fiber. *Optics Express*, 19(17):16665–16671, 2011.

[8] K. Saitoh and S. Matsuo. Multicore fiber technology. *Journal of Lightwave Technology*, 34(1):55–66, 2016.

[9] R. Ryf, S. Randel, A. Gnauck, C. Bolle, A. Sierra, S. Mumtaz, M. Esmaeelpour, E. Burrows, R. Essiambre, P. Winzer, et al. Mode-division multiplexing over 96 km of few-mode fiber using coherent 6×6 mimo processing. *Journal of Lightwave technology*, 30(4):521–531, 2012.

[10] D. Soma, Y. Wakayama, S. Beppu, S. Sumita, T. Tsuritani, T. Hayashi, T. Nagashima, M. Suzuki, H. Takahashi, K. Igarashi, et al. 10.16 peta-bit/s dense sdm/wdm transmission over low-dmd 6-mode 19-core fibre across c+ l band. In *Optical Communication (ECOC), 2017 European Conference on*, pages 1–3. IEEE, 2017.

[11] P. Mitra and J. Stark. Nonlinear limits to the information capacity of optical fibre communications. *Nature*, 411(6841):1027, 2001.

[12] R. Essiambre, G. Kramer, P. Winzer, G. Foschini, and B. Goebel. Capacity limits of optical fiber networks. *Journal of Lightwave Technology*, 28(4):662–701, 2010.

[13] G. Agrawal. *Nonlinear fiber optics*. Springer, 2000.

[14] R. Dar and P. Winzer. Nonlinear interference mitigation: Methods and potential gain. *Journal of Lightwave Technology*, 35(4):903–930, 2017.

[15] E. Ip and J. Kahn. Compensation of dispersion and nonlinear impairments using digital backpropagation. *Journal of Lightwave Technology*, 26(20):3416–3425, 2008.

[16] J. Cartledge, F. Guiomar, . Kschischang, G. Liga, and M. Yankov. Digital signal processing for fiber nonlinearities. *Optics express*, 25(3):1916–1936, 2017.

[17] P. Poggiolini. The gn model of non-linear propagation in uncompensated coherent optical systems. *Journal of Lightwave Technology*, 30(24):3857–3879, 2012.

[18] E. Temprana, E. Myslivets, L. Liu, V. Ataie, A. Wiberg, B. Kuo, N. Alic, and S. Radic. Two-fold transmission reach enhancement enabled by transmitter-side digital back-propagation and optical frequency comb-derived information carriers. *Optics express*, 23(16):20774–20783, 2015.

[19] M. Al-Khateeb, M. McCarthy, C. Sánchez, and A. Ellis. Nonlinearity compensation using optical phase conjugation deployed in discretely amplified transmission systems. *Optics express*, 26(18):23945–23959, 2018.

[20] K. Solis-Trapala, M. Pelusi, H. Tan, T. Inoue, and S. Namiki. Optimized wdm transmission impairment mitigation by multiple phase conjugations. *Journal of Lightwave Technology*, 34(2):431–440, 2016.

[21] A. Ellis, M. McCarthy, M. Al Khateeb, M. Sorokina, and N. Doran. Performance limits in optical communications due to fiber nonlinearity. *Advances in Optics and Photonics*, 9(3):429–503, 2017.

[22] J. Cai, H. Batshon, M. Mazurczyk, O. Sinkin, D. Wang, M. Paskov, W. Patterson, C. Davidson, P. Corbett, G. Wolter, et al. 70.4 tb/s capacity over 7,600 km in c+l band using coded modulation with hybrid constellation shaping and nonlinearity compensation. In *Optical Fiber Communication Conference*, pages Th5B–2. Optical Society of America, 2017.

[23] A. Ellis, N. Suibhne, D. Saad, and D. Payne. Communication networks beyond the capacity crunch. *Philosophical Transactions of the Royal Society of London A: Mathematical, Physical and Engineering Sciences*, 374(2062), 2016. ISSN 1364-503X. doi: 10.1098/rsta.2015.0191. URL http://rsta.royalsocietypublishing.org/content/374/2062/20150191.

[24] S. Derevyanko, J. Prilepsky, and S. Turitsyn. Capacity estimates for optical transmission based on the nonlinear fourier transform. *Nature communications*, 7:12710, 2016.

[25] M. Yousefi and X. Yangzhang. Linear and nonlinear frequency-division multiplexing. In *ECOC 2016; 42nd European Conference on Optical Communication; Proceedings of*, pages 1–3. VDE, 2016.

[26] A. Hasegawa. Soliton-based optical communications: An overview. *IEEE Journal of Selected Topics in Quantum Electronics*, 6(6):1161–1172, 2000.

[27] K. Blow and N. Doran. Bandwidth limits of nonlinear (soliton) optical communication systems. *Electronics Letters*, 19(11):429–430, 1983.

[28] M. Yousefi and F. Kschischang. Information transmission using the nonlinear fourier transform, part i: Mathematical tools. *IEEE Transactions on Information Theory*, 60 (7):4312–4328, 2014.

[29] L. Beygi, E. Agrell, P. Johannisson, M. Karlsson, and H. Wymeersch. A discrete-time model for uncompensated single-channel fiber-optical links. *IEEE Transactions on Communications*, 60(11):3440–3450, 2012.

[30] S. Le, V. Aref, and H. Buelow. Nonlinear signal multiplexing for communication beyond the kerr nonlinearity limit. *Nature Photonics*, 11(9):570, 2017.

[31] V. Matveev. 30 years of finite-gap integration theory. *Philosophical Transactions of the Royal Society of London A: Mathematical, Physical and Engineering Sciences*, 366(1867):837–875, 2008.

[32] A. Osborne. Soliton physics and the periodic inverse scattering transform. *Physica D: Nonlinear Phenomena*, 86(1-2):81–89, 1995.

[33] K. Chow, K. Nakkeeran, and B. Malomed. Periodic waves in bimodal optical fibers. *Optics communications*, 219(1-6):251–259, 2003.

[34] A. Osborne, M. Onorato, and M. Serio. The nonlinear dynamics of rogue waves and holes in deep-water gravity wave trains. *Physics Letters A*, 275(5-6):386–393, 2000.

[35] A. Islas and C. Schober. Predicting rogue waves in random oceanic sea states. *Physics of fluids*, 17(3):031701, 2005.

[36] A. Calini and C. Schober. Homoclinic chaos increases the likelihood of rogue wave formation. *Physics Letters A*, 298(5-6):335–349, 2002.

[37] A. Calini and T. Ivey. Finite-gap solutions of the vortex filament equation: isoperiodic deformations. *Journal of Nonlinear Science*, 17(6):527–567, 2007.

[38] . Randoux, P. Suret, and G. El. Inverse scattering transform analysis of rogue waves using local periodization procedure. *Scientific reports*, 6:29238, 2016.

[39] C. Gardner, J. Greene, M. Kruskal, and R. Miura. Method for solving the korteweg-devries equation. *Physical Review Letters*, 19(19):1095, 1967.

[40] P. Lax. Integrals of nonlinear equations of evolution and solitary waves. *Communications on pure and applied mathematics*, 21(5):467–490, 1968.

[41] A. Shabat and V. Zakharov. Exact theory of two-dimensional self-focusing and one-dimensional self-modulation of waves in nonlinear media. *Soviet physics JETP*, 34(1): 62, 1972.

[42] V. Kotlyarov and D. Shepelsky. Planar unmodular baker-akhiezer function for the nonlinear schrödinger equation. *Annals of Mathematical Sciences and Applications*, 2 (2):343–384, 2017.

[43] E. Tracy and H. Chen. Nonlinear self-modulation: An exactly solvable model. *Physical Review A*, 37(3):815, 1988.

[44] E. Belokolos, A. Bobenko, V. Enol'skii, A. Its, and V. Matveev. *Algebro-Geometric Approach to Nonlinear Integrable Equations*. Springer-Verlag, 1994.

[45] A. Bobenko and C. Klein. *Computational approach to Riemann surfaces*. Springer, 2011.

[46] M. Patterson. *Algebro-geometric algorithms for integrable systems*. PhD thesis, 2007.

[47] S. Olver and G. Wechslberger. Rhpackage, a mathematica package for computing solutions to matrix-valued riemann–hilbert problems. 2010. URL http://www.maths. usyd.edu.au/u/olver/projects/RHPackage.html.

[48] S. Olver. A general framework for solving riemann–hilbert problems numerically. *Numerische Mathematik*, 122(2):305–340, 2012.

[49] S. Wahls and V. Poor. Fast numerical nonlinear fourier transforms. *IEEE Transactions on Information Theory*, 61(12):6957–6974, 2015.

[50] M. Yousefi and F. Kschischang. Information transmission using the nonlinear fourier transform, part ii: Numerical methods. *IEEE Transactions on Information Theory*, 60 (7):4329–4345, 2014.

[51] G. Boffetta and A. Osborne. Computation of the direct scattering transform for the nonlinear schrödinger equation. *Journal of Computational Physics*, 102(2):252 – 264, 1992. ISSN 0021-9991. doi: https://doi.org/10.1016/0021-9991(92)90370-E.

[52] A. Vasylchenkova, J. Prilepsky, D. Shepelsky, and A. Chattopadhyay. Direct nonlinear fourier transform algorithms for the computation of solitonic spectra in focusing nonlinear schr\" odinger equation. *arXiv preprint arXiv:1708.01144*, 2017.

[53] C. Olivier, B. Herbst, and M. Molchan. A numerical study of the large-period limit of a zakharov–shabat eigenvalue problem with periodic potentials. *Journal of Physics A: Mathematical and Theoretical*, 45(25):255205, 2012.

[54] B. Deconinck and J. Kutz. Computing spectra of linear operators using the floquet–fourier–hill method. *Journal of Computational Physics*, 219(1):296–321, 2006.

[55] A. Osborne. The random and deterministic dynamics of 'rogue waves' in unidirectional, deep-water wave trains. *Marine structures*, 14(3):275–293, 2001.

[56] C. Swierczewski et al. Abelfunctions: A library for computing with abelian functions, riemann surfaces, and algebraic curves. 2017. URL http://github.com/abelfunctions/abelfunctions.

[57] M. van Hoeij and B. Deconinck. algcurves, a maple library. 2000. URL https://www.math.fsu.edu/~hoeij/lib/algcurves/src/.

[58] B. Deconinck and M. Van Hoeij. Computing riemann matrices of algebraic curves. *Physica D: Nonlinear Phenomena*, 152:28–46, 2001.

[59] C. Kalla and C. Klein. On the numerical evaluation of algebro-geometric solutions to integrable equations. *Nonlinearity*, 25(3):569, 2012.

[60] B. Deconinck, M. Patterson, and C. Swierczewski. Computing the riemann constant vector. *preprint, available online at https://depts. washington. edu/bdecon/papers/pdfs/rcv. pdf*, 2015.

[61] A. Osborne. *Nonlinear Ocean Wave and the Inverse Scattering Transform.* Elsevier, London, 2002.

[62] B. Deconinck, M. Heil, A. Bobenko, M. Van Hoeij, and M. Schmies. Computing riemann theta functions. *Mathematics of Computation*, 73(247):1417–1442, 2004.

[63] T. Trogdon and S. Olver. Numerical inverse scattering for the focusing and defocusing nonlinear schrödinger equations. In *Proc. R. Soc. A*, volume 469, page 20120330. The Royal Society, 2013.

[64] T. Trogdon and S. Olver. *Riemann-Hilbert problems, their numerical solution, and the computation of nonlinear special functions.* Siam, 2016.

[65] D. Kedziora, A. Ankiewicz, and N. Akhmediev. Rogue waves and solitons on a cnoidal background. *The European Physical Journal Special Topics*, 223(1):43–62, Jan 2014. ISSN 1951-6401. doi: 10.1140/epjst/e2014-02083-4. URL https://doi.org/10.1140/epjst/e2014-02083-4.

[66] M. Salle and V. Matveev. Darboux transformations and solitons. 1991.

[67] H. Steudel and R. Meinel. Periodic solutions generated by bäcklund transformations. *Physica D: Nonlinear Phenomena*, 21(1):155–162, 1986. doi: https://doi.org/10.1016/0167-2789(86)90086-2. URL http://www.sciencedirect.com/science/article/pii/0167278986900862.

[68] J. Frauendiener, C. Klein, and V. Shramchenko. Efficient computation of the branching structure of an algebraic curve. *Computational Methods and Function Theory*, 11(2): 527–546, 2012.

[69] J. Yang. *Nonlinear waves in integrable and nonintegrable systems*, volume 16. Siam, 2010.

[70] O. Belai, L. Frumin, E. Podivilov, and D. Shapiro. Efficient numerical method of the fiber bragg grating synthesis. *J. Opt. Soc. Am. B*, 24(7):1451–1457, Jul 2007. doi: 10.1364/JOSAB.24.001451.

[71] L. Frumin, O. Belai, E. Podivilov, and D. Shapiro. Efficient numerical method for solving the direct zakharov–shabat scattering problem. *JOSA B*, 32(2):290–296, 2015.

[72] G. Xiao and K. Yashiro. An efficient algorithm for solving zakharov-shabat inverse scattering problem. *IEEE transactions on antennas and propagation*, 50(6):807–811, 2002.

[73] S. Wahls and V. Vaibhav. Fast inverse nonlinear fourier transforms for fiber bragg grating design and related problems. *arXiv preprint arXiv:1607.01305*, 2016.

[74] A. Hasegawa and T. Nyu. Eigenvalue communication. *Journal of lightwave technology*, 11(3):395–399, 1993.

[75] M. Yousefi and F. Kschischang. Information transmission using the nonlinear fourier transform, part iii: Spectrum modulation. *IEEE Transactions on Information Theory*, 60(7):4346–4369, 2014.

[76] S. Turitsyn, J. Prilepsky, S. Le, S. Wahls, L. Frumin, M. Kamalian, and S. Derevyanko. Nonlinear fourier transform for optical data processing and transmission: advances and perspectives. *Optica*, 4(3):307–322, 2017.

[77] H. Bülow. Experimental demonstration of optical signal detection using nonlinear fourier transform. *Journal of Lightwave Technology*, 33(7):1433–1439, 2015.

[78] S. Civelli, E. Forestieri, and M. Secondini. Decision-feedback detection strategy for nonlinear frequency-division multiplexing. *Optics express*, 26(9):12057–12071, 2018.

[79] S. Le, J. Prilepsky, and S. Turitsyn. Nonlinear inverse synthesis for high spectral efficiency transmission in optical fibers. *Optics express*, 22(22):26720–26741, 2014.

[80] S. Wahls, S. Le, J. Prilepsk, V. Poor, and S. Turitsyn. Digital backpropagation in the nonlinear fourier domain. In *Signal Processing Advances in Wireless Communications (SPAWC), 2015 IEEE 16th International Workshop on*, pages 445–449. IEEE, 2015.

[81] V. Aref. Control and detection of discrete spectral amplitudes in nonlinear fourier spectrum. *arXiv preprint arXiv:1605.06328*, 2016.

[82] H. Bülow, V. Aref, and L. Schmalen. Modulation on discrete nonlinear spectrum: Perturbation sensitivity and achievable rates. *IEEE Photonics Technology Letters*, 30: 423–426, 2018.

[83] T. Gui, T. Chan, C. Lu, A. Lau, and P. Wai. Alternative decoding methods for optical communications based on nonlinear fourier transform. *Journal of Lightwave Technology*, 35(9):1542–1550, 2017.

[84] H. Buelow, V. Aref, and W. Idler. Transmission of waveforms determined by 7 eigenvalues with psk-modulated spectral amplitudes. In *ECOC 2016; 42nd European Conference on Optical Communication; Proceedings of*, pages 1–3. VDE, 2016.

[85] A. Span, V. Aref, H. Bülow, and S. Ten Brink. On time-bandwidth product of multi-soliton pulses. In *Information Theory (ISIT), 2017 IEEE International Symposium on*, pages 61–65. IEEE, 2017.

[86] J. Prilepsky, S. Derevyanko, K. Blow, I. Gabitov, and S. Turitsyn. Nonlinear inverse synthesis and eigenvalue division multiplexing in optical fiber channels. *Physical review letters*, 113(1):013901, 2014.

[87] S. Le, J. Prilepsky, and S. Turitsyn. Nonlinear inverse synthesis technique for optical links with lumped amplification. *Optics express*, 23(7):8317–8328, 2015.

[88] S. Le, I. Philips, J. Prilepsky, P. Harper, A. Ellis, and S. Turitsyn. Demonstration of nonlinear inverse synthesis transmission over transoceanic distances. *Journal of Lightwave Technology*, 34(10):2459–2466, 2016.

[89] I. Tavakkolnia and M. Safari. Capacity analysis of signaling on the continuous spectrum of nonlinear optical fibers. *Journal of Lightwave Technology*, 35(11):2086–2097, 2017.

[90] I. Tavakkolnia and M. Safari. Dispersion pre-compensation for nft-based optical fiber communication systems. In *Lasers and Electro-Optics (CLEO), 2016 Conference on*, pages 1–2. IEEE, 2016.

[91] X. Yangzhang, M. Yousefi, A. Alvarado, D. Lavery, and P. Bayvel. Nonlinear frequency-division multiplexing in the focusing regime. In *Optical Fiber Communication Conference*, pages Tu3D–1. Optical Society of America, 2017.

[92] X. Yangzhang, D. Lavery, P. Bayvel, and M. Yousefi. Impact of perturbations on nonlinear frequency-division multiplexing. *Journal of Lightwave Technology*, 36(2): 485–494, 2018.

[93] S. Wahls. Generation of time-limited signals in the nonlinear fourier domain via b-modulation. In *Proc. Eur. Conf. Opt. Commun., Gothenburg, Sweden*, 2017.

[94] S. Le, K. Schuh, . Buchali, and H. Bülow. 100 gbps b-modulated nonlinear frequency division multiplexed transmission. In *Optical Fiber Communication Conference*, pages W1G–6. Optical Society of America, 2018.

[95] Z. Dong, S. Hari, T. Gui, K. Zhong, M. Yousefi, C. Lu, P-K A. Wai, F Kschischang, and A Lau. Nonlinear frequency division multiplexed transmissions based on nft. *IEEE Photonics Techn. Lett.*, (99), 2015.

[96] I. Tavakkolnia and M. Safari. Signalling over nonlinear fibre-optic channels by utilizing both solitonic and radiative spectra. In *Networks and Communications (EuCNC), 2015 European Conference on*, pages 103–107. IEEE, 2015.

[97] V. Aref, S. Le, and H. Buelow. Demonstration of fully nonlinear spectrum modulated system in the highly nonlinear optical transmission regime. In *ECOC-Post Deadline Paper; 42nd European Conference on Optical Communication; Proceedings of*, pages 1–3. VDE, 2016.

[98] V. Aref, S. Le, and H. Buelow. Modulation over nonlinear fourier spectrum: Continuous and discrete spectrum. *Journal of Lightwave Technology*, 36(6):1289–1295, 2018.

[99] I. Tavakkolnia and M. Safari. Effect of pmd on the continuous spectrum of nonlinear optical fibre. In *Lasers and Electro-Optics Europe & European Quantum Electronics Conference (CLEO/Europe-EQEC, Conference on)*. IEEE, 2017.

[100] S. Manakov. On the theory of two-dimensional stationary self-focusing of electromagnetic waves. *Soviet Physics-JETP*, 38(2):248–253, 1974.

[101] C. Menyuk and B. Marks. Interaction of polarization mode dispersion and nonlinearity in optical fiber transmission systems. *Journal of Lightwave Technology*, 24(7):2806, 2006.

[102] S. Gaiarin, A. Perego, E. da Silva, F. Da Ros, and D. Zibar. Dual-polarization nonlinear fourier transform-based optical communication system. *Optica*, 5(3):263–270, 2018.

[103] O. Wright. The darboux transformation of some manakov systems. *Applied mathematics letters*, 16(5):647–652, 2003.

[104] J. Goossens, M. Yousefi, Y. Jaouën, and H. Hafermann. Polarization-division multiplexing based on the nonlinear fourier transform. *Optics express*, 25(22):26437–26452, 2017.

[105] T. Gui, W. Gemechu, J. Goossens, M. Song, S. Wabnitz, M. Yousefi, H. Hafermann, A. Tao Lau, and Y. Jaouën. Polarization-division-multiplexed nonlinear frequency division multiplexing. In *CLEO: Science and Innovations*, pages STu4C–3. Optical Society of America, 2018.

[106] X. Yangzhang, V. Aref, S. Le, H. Bulow, and P. Bayvel. 400 gbps dual-polarisation non-linear frequency-division multiplexed transmission with b-modulation. *arXiv preprint arXiv:1806.10367*, pages 1–3, 2018.

[107] A. Buchberger, V. Aref, and L. Schmalen. Probabilistic eigenvalue shaping for nonlinear fourier transform transmission. *arXiv preprint arXiv:1712.08467*, 2017.

[108] S. Wahls. Second order statistics of the scattering vector defining the dt nonlinear fourier transform. In *SCC 2017; 11th International ITG Conference on Systems, Communications and Coding; Proceedings of*, pages 1–6. VDE, 2017.

[109] Q. Zhang and T. Chan. Noise models in the nonlinear spectral domain for optical fibre communications. *arXiv preprint arXiv:1702.06226*, 2017.

[110] N. Shevchenko, S. Derevyanko, J. Prilepsky, A. Alvarado, P. Bayvel, and S. Turitsyn. Capacity lower bounds of the noncentral chi-channel with applications to soliton amplitude modulation. *IEEE Transactions on Communications*, 2018. doi: 10.1109/TCOMM.2018.2808286.

[111] P. Kazakopoulos and A. Moustakas. On the soliton spectral efficiency in non-linear optical fibers. In *2016 IEEE International Symposium on Information Theory (ISIT)*, pages 610–614, July 2016. doi: 10.1109/ISIT.2016.7541371.

[112] P. Kazakopoulos and A. Moustakas. Nonlinear schrödinger equation with random gaussian input: Distribution of inverse scattering data and eigenvalues. *Phys. Rev. E*, 78:016603, Jul 2008. doi: 10.1103/PhysRevE.78.016603. URL https://link.aps.org/doi/10.1103/PhysRevE.78.016603.

[113] S. Derevyanko. Appearance of bound states in random potentials with applications to soliton theory. *Physical Review E*, 84(1):016601, 2011.

[114] M. Bertola and P. Giavedoni. A degeneration of two-phase solutions of the focusing nonlinear schrödinger equation via riemann-hilbert problems. *Journal of Mathematical Physics*, 56(6):061507, 2015.

[115] A. Smirnov. Solution of a nonlinear schrödinger equation in the form of two-phase freak waves. *Theoretical and Mathematical Physics*, 173(1):1403–1416, 2012.

[116] A. Smirnov, E. Semenova, V. Zinger, and N. Zinger. On a periodic solution of the focusing nonlinear schrödinger equation. *arXiv preprint arXiv:1407.7974*, 2014.

[117] A. Smirnov. Periodic two-phase "rogue waves". *Mathematical Notes*, 94(5-6):897–907, 2013.

[118] A. Kamchatnov. New approach to periodic solutions of integrable equations and nonlinear theory of modulational instability. *Physics Reports*, 286:199–270, 1997.

[119] E. Agrell, A. Alvarado, G. Durisi, and M. Karlsson. Capacity of a nonlinear optical channel with finite memory. *Journal of Lightwave Technology*, 32(16):2862–2876, 2014.

[120] J. Ania-Castanón, T. Ellingham, R Ibbotson, X Chen, L. Zhang, and S. Turitsyn. Ultralong raman fiber lasers as virtually lossless optical media. *Physical review letters*, 96(2):023902, 2006.

[121] Y. Ma and M. Ablowitz. The periodic cubic schrödinger equation. *Studies in Applied Mathematics*, 65(2):113–158, 1981.

[122] A. Its and V. Kotljarov. Explicit formulas for solutions of schrödinger nonlinear equation. *Dopovidi Akademii Nauk Ukrainskoi RSR Seriya A-Fiziko-Matematichni ta Technichni Nauki*, (11):965–968, 1976.

Appendix A

Algebro-geometric approach for a special nonlinear spectrum

Suppose we have a 2-genus signal with the NS of the kind shown in Fig. 4.13a which is a spectrum with three complex conjugate pairs of eigenvalues, $\{\zeta_0, \zeta_1, \zeta_2\}$, where $\zeta_2 = -\zeta_0^* = a + bi$ and $\zeta_1 = ci$ with $a, b, c > 0$. The associate Riemann surface, (2.24), is determined by:

$$\Gamma : \omega^2 = \left(\zeta^2 + c^2\right)\left(\zeta^4 + 2(b^2 - a^2)\zeta^2 + (a^2 + b^2)^2\right). \tag{A.1}$$

A basis of normalised holomorphic differentials are defined as

$$d\nu_j = \frac{C_{j1}\zeta + C_{j2}}{\omega}d\zeta \tag{A.2}$$

on this surface where the basis of cycles is shown in Fig. 4.13b. This structure of the main spectrum makes the Riemann matrix of the surface (2.24) as

$$\mathsf{B} = \begin{bmatrix} 2i\mathfrak{b}_1 & -0.5 + i\mathfrak{b}_1 \\ -0.5 + i\mathfrak{b}_1 & i\mathfrak{b}_2 \end{bmatrix} \tag{A.3}$$

where $\mathfrak{b}_{1,2}$ will be defined later. A Riemann theta function with this Riemann matrix can be read as a product of some one-dimensional Riemann theta functions as below

$$\begin{aligned} \Theta(u_1, u_2; \mathsf{B}) &= \vartheta_3(u_1 - 2u_2; 2 + 4i\mathfrak{b}_2 - 2i\mathfrak{b}_1) \times \vartheta_3(u_1; 2i\mathfrak{b}_1) \\ &\quad + \vartheta_1(u_1 - 2u_2; 2 + 4i\mathfrak{b}_2 - 2i\mathfrak{b}_1) \times \vartheta_1(u_1; 2i\mathfrak{b}_1), \end{aligned} \tag{A.4}$$

where

$$\vartheta_3(u; \mathfrak{b}) = 1 + 2\sum_{m=1}^{\infty} e^{\pi i \mathfrak{b} m^2} \cos 2m\pi u, \quad \vartheta_1(u; \mathfrak{b}) = 2\sum_{m=1}^{\infty} (-1)^m e^{\pi i \mathfrak{b}(m+0.5)^2} \sin(2m+1)\pi u,$$

are the Jacobi elliptic functions. Using two covering mappings with respect to two involutions:

$$\tau : (\omega, \zeta) \to (-\omega, -\zeta), \quad \tau_0 : (\omega, \zeta) \to (-\omega, \zeta)$$

we can calculate $\mathfrak{b}_{1,2}$, $\mathbf{V}$ and $\mathbf{U}$ in (2.28) and the coefficients of the normalised holomorphic differentials (A.2).The latter is

$$C = \begin{bmatrix} -\frac{i}{A_+} & 0 \\ -\frac{i}{2A_+} & -\frac{i}{A_-} \end{bmatrix},$$

$$A_+ = \int_{-\infty}^{-c^2} \frac{dt}{\sqrt{-(t+c^2)(t^2 + 2(b^2 - a^2)t + (a^2 + b^2)^2)}},$$

$$A_- = \int_{-c^2}^{0} \frac{dt}{\sqrt{-t(t+c^2)(t^2 + 2(b^2 - a^2)t + (a^2 + b^2)^2)}}.$$

Note that $C_{12} = 0$ which makes the frequencies (i.e. the elements of $\mathbf{V}$) commensurable and the signal periodic. The elements of the Riemann matrix (A.3) are calculated as follows:

$$\mathfrak{b}_1 = \frac{B_+}{2A_+}, \quad \mathfrak{b}_2 = \frac{B_+}{4A_+} + \frac{B_-}{4A_-}, \quad \mathfrak{b}_+ = \frac{B_+}{A_+}, \quad \mathfrak{b}_- = \frac{B_-}{A_-},$$

$$B_-^1 = \int_{-\infty}^{-c^2} \frac{dt}{\sqrt{t(t+c^2)(t^2 + 2(b^2 - a^2)t + (a^2 + b^2)^2)}},$$

$$B_-^2 = \int_{0}^{\infty} \frac{dt}{\sqrt{t(t+c^2)(t^2 + 2(b^2 - a^2)t + (a^2 + b^2)^2)}},$$

$$B_+ = \int_{-c^2}^{0} \frac{dt}{\sqrt{t(t+c^2)(t^2 + 2(b^2 - a^2)t + (a^2 + b^2)^2)}},$$

$$B_- = B_-^1 + B_-^2.$$

The phases are

$$\Delta_1 = \frac{1}{2} - i\delta_1, \quad \Delta_2 = \frac{1}{2} - i\frac{\delta_1 + \delta_2}{2}, \quad \delta_1 = \frac{B_+}{2A_+}, \quad \delta_2 = \frac{B_-^2 - B_-^1}{2A_-}. \tag{A.5}$$

Two other parameters to define in order to construct the solution (2.36), $\mathbf{r}$ and A_0 are calculated as

$$A_0^2 = e^{\pi i + D\delta_2 + \frac{F}{2}},$$

$$D = \int_{-c^2}^{0} \frac{t\,dt}{\sqrt{-t(t+c^2)(t^2+2(b^2-a^2)t+(a^2+b^2)^2)}},$$

$$F = \log r - \int_{c^2}^{r} \frac{t\,dt}{\sqrt{t(t-c^2)(t^2-2(b^2-a^2)t+(a^2+b^2)^2)}}$$

$$+ \int_{c^2}^{r} \left(\frac{1}{t} - \frac{t}{\sqrt{t(t-c^2)(t^2-2(b^2-a^2)t+(a^2+b^2)^2)}} \right) dt \qquad (A.6)$$

$$- \int_{0}^{r} \frac{t\,dt}{\sqrt{t(t+c^2)(t^2+2(b^2-a^2)t+(a^2+b^2)^2)}}$$

$$+ \int_{r}^{\infty} \left(\frac{1}{t} - \frac{t}{\sqrt{t(t+c^2)(t^2+2(b^2-a^2)t+(a^2+b^2)^2)}} \right) dt,$$

where r is a free parameter. Finally, the solution (2.36) is

$$q(t,z) = \frac{\vartheta_4(u_1;i\mathfrak{b}_+)\vartheta_4(u_2;i\mathfrak{b}_-) - \vartheta_2(u_1;i\mathfrak{b}_+)\vartheta_2(u_2;i\mathfrak{b}_-)}{\vartheta_4(u_5;i\mathfrak{b}_+)\vartheta_4(u_6;i\mathfrak{b}_-) - \vartheta_2(u_5;i\mathfrak{b}_+)\vartheta_2(u_6;i\mathfrak{b}_-)}$$
$$\times \frac{\vartheta_4(u_3;i\mathfrak{b}_+)\vartheta_4(u_4;i\mathfrak{b}_-) - \vartheta_2(u_3;i\mathfrak{b}_+)\vartheta_2(u_4;i\mathfrak{b}_-)}{\vartheta_4(u_7;i\mathfrak{b}_+)\vartheta_4(u_8;i\mathfrak{b}_-) - \vartheta_2(u_7;i\mathfrak{b}_+)\vartheta_2(u_8;i\mathfrak{b}_-)} \qquad (A.7)$$

with

$$u_1 = \frac{2}{A_+}t + Z_1 - i\delta_1, \quad u_2 = \frac{4}{A_-}z + Z_1 - 2Z_2 + i\delta_2, \quad u_3 = \frac{2}{A_+}t + Z_1 + i\delta_1,$$

$$u_4 = \frac{4}{A_-}z + Z_1 - 2Z_2 - i\delta_2, \quad u_5 = Z_1 - i\delta_1, \quad u_6 = Z_1 - 2Z_2 + i\delta_2,$$

$$u_7 = \frac{2}{A_+}t + Z_1 - 0.5, \quad u_8 = \frac{4}{A_-}z + Z_1 - 2Z_2 + 0.5,$$

where $Z_{1,2}$ are arbitrary numbers playing the role of the auxiliary spectrum.

Appendix B

Numerical calculation of the Riemann theta function

In this appendix we argue how the numerical computational complexity of evaluating the Riemann theta function can be reduced. To numerically calculate the Riemann theta function of dimension $\mathcal{N}$ the space of permutations of $\mathcal{N}$-dimensional vectors, $\mathbf{l}$ in (2.30) should be truncated. Let assume elements of $\mathbf{l}$ are smaller than M_1, hence [61]

$$\Theta(u_1,\ldots,u_{\mathcal{N}}) = \sum_{l_1=-M_1}^{M_1} \sum_{l_2=-M_1}^{M_1} \cdots \sum_{l_{\mathcal{N}}=-M_1}^{M_1} \exp\left\{\pi i(B\mathbf{l},\mathbf{l}) + 2\pi i(\mathbf{l},\mathbf{u})\right\}, \tag{B.1}$$

where $\mathbf{l} = [l_1, l_2, \cdots, l_{\mathcal{N}}]$. Therefore, the number of exponential terms to add amounts to $(2M_1+1)^{\mathcal{N}}$ which grows very fast. Although for low $\mathcal{N}$ one can reduce the necessary terms using some trigonometric relations, the growth is still substantial. One can read (B.1) as a single summation over an ordering parameter n as below (when $M_1 \to \infty$)

$$\Theta(u_1,\ldots,u_{\mathcal{N}}) = \sum_{n=0}^{\infty} \exp\left\{2\pi i(\mathbf{l}_n,\mathbf{u})\right\} \exp\left\{\pi i(B\mathbf{l}_n,\mathbf{l}_n)\right\} = \sum_{n=0}^{\infty} q_n \exp\left\{2\pi i(\mathbf{l}_n,\mathbf{u})\right\},$$
$$q_n = \exp\left\{\pi i(B\mathbf{l}_n,\mathbf{l}_n)\right\}. \tag{B.2}$$

In the final representation of the solution to the NLSE, Riemann theta function appears as in Eq. (2.36) in which the dependence on time is in the form of some modes with frequencies in $\mathbf{V}$. We assume that we only need to calculate $q(t,z)$ at a particular z. When working with periodic signals, the frequencies are commensurable, hence, all multiples of a fundamental frequency $\Delta\omega$. Consequently, the time-dependent part of $(\mathbf{l}_n,\mathbf{u})$ is an integer multiple, c_n, of

$\Delta\omega$ depending on $\mathbf{l}_n$. So, the summation in (B.2) can be turn into another one as

$$\Theta(u_1,\ldots,u_{\mathcal{N}}) = \sum_{n=0} \theta_n \exp\{2\pi i c_n \Delta\omega t\}, \tag{B.3}$$

$$\theta_n = \sum_{\substack{\text{all } l \text{ where } c_l = n}}^{\infty} q_l, \tag{B.4}$$

where θ_n is the sum of all q_ns attributed to c_n. In this way, calculating the Riemann theta function is computing a Fourier series (B.3) with coefficients coming from another Fourier series (B.4). These coefficients can be used for all subsequent calculations, hence, a huge reduction in the computational complexity [61]. Furthermore, regarding the amplitude of the terms in the summation, one can consider ignoring some parts of the grid for some computational gain at the expense of losing accuracy. This, if done correctly, can speed up the calculations even further [61, 62]. To a grid of integers in the interval $(-M_1, M_1)$ and when the theta function only needs to be realised at $z = 0$, i.e. the transmitter site, the computational complexity of the first equation in (B.3) for N samples in time is

$$O(N\mathcal{N}(2M_1+1)^{\mathcal{N}}\log(2M_1+1), \tag{B.5}$$

which grows exponentially with the number of cuts. This growth matters specially in a multi-cut spectrum case. Despite all attempts to decrease the computational burden; time and memory consumption, calculating the Riemann theta function to an arbitrary level of accuracy is still not affordable.

Appendix C

Numerical routines of finding the nonlinear spectrum

For a periodic signal, the first step of finding the NS is to calculate the monodromy matrix defined in Chapter 2.3. From this matrix, the NS is defined in two senses; Ma and Ablowitz definition [121], and Kotlyarov and Its [122]. In this work, we consider the latter in which the NS consists of the following components:

$$\begin{aligned} \textit{Main spectrum}: & \quad \lambda_1, \lambda_2, \cdots, \lambda_{\mathscr{N}} \in \mathbb{C}, \\ \textit{Auxiliary spectrum}: & \quad \mu_1(t,z), \mu_2(t,z), \cdots, \mu_{\mathscr{N}}(t,z), \end{aligned} \tag{C.1}$$

plus a set of numbers $\sigma_j \in \{\pm 1\}$ determining the cover of the Riemann sheet on which $\mu_j(t,z)$ lies. Assuming Eqs. (2.22), it is easy to realise that the auxiliary spectrum can be found as the zeros of the off-diagonal elements of the monodromy matrix. The main spectrum, on the other hand, is a set of simple endpoints of the continuous spectrum at which the trace of the monodromy matrix, called the *discriminant*, Δ, is ± 2.

Solving the Zakharov-Shabat equation in (2.4) is to solve the following equation at each λ [MK5]:

$$\frac{d}{dt}\mathbf{A} = \mathbf{P} \times \mathbf{A}, \quad \text{with} \quad \mathbf{P} = \begin{bmatrix} -i\lambda & -q \\ -q^* & i\lambda \end{bmatrix}, \quad \text{and} \quad \mathbf{A}(t_0; \lambda) = \mathbf{I}. \tag{C.2}$$

Then, the monodromy matrix is $\mathbf{A}(t_0 + T; \lambda)$. To make the difference equation, time is defined as points, $t_0, t_1, \cdots, t_{N-1} = t_0 + T$ where $\Delta t = t_i - t_{i-1}$. Starting from $i = 0$, we iteratively calculate $\mathbf{A}(t_{i+1}; \lambda)$. Different approximations lead to different numerical routines. Here we compare four numerical approaches: *Ablowitz-Ladik*, *layer-peeling* (*Bofetta-Osborne*), and *spectral*.

- **Layer-peeling**: A general solution to Eq. (C.2) is in a form of an exponential function. One can write the solution at the end of each segment as: $\mathbf{A}(t_{i+1}; \lambda) = U(q_n)\mathbf{A}(t_i; \lambda)$ where

$$U(q_n) = \exp\left(\Delta t \begin{bmatrix} -i\lambda & q_n \\ -q_n^* & i\lambda \end{bmatrix}\right) = \begin{pmatrix} \cos k\Delta t - \frac{i\lambda}{k}\sin k\Delta t & \frac{q_n}{k}\sin k\Delta t \\ -\frac{q_n^*}{k}\sin k\Delta t & \cos k\Delta t + \frac{i\lambda}{k}\sin k\Delta t \end{pmatrix}$$

where $q_n = q(t_n)$ and $k^2 = |q_n|^2 + \lambda^2$ is assumed to be constant over the interval $[n\Delta t, (n+1)\Delta t]$. At the end of one period the monodromy matrix is then approximately given by the expression [61, MK5]

$$\mathbf{A}(t_0 + T; \lambda) = \prod_{n=0}^{N} U(q_n)\mathbf{A}(t_0; \lambda) = \prod_{n=0}^{N} U(q_n). \tag{C.3}$$

The main spectrum is then calculated as the zeros of $\mathrm{Tr}\,\mathbf{A}(t_0 + T; \lambda) \pm 2$.

- **Ablowitz-Ladik**: A simple approximation for the time derivative in Eq. (C.2) is:

$$\frac{\mathbf{A}(t_n + \Delta t; \lambda) - \mathbf{A}(t_n; \lambda)}{\Delta t} = \frac{\mathbf{P}(q_{n+1})\mathbf{A}(t_n + \Delta t; \lambda) - \mathbf{P}(q_n)\mathbf{A}(t_n; \lambda)}{2}, \tag{C.4}$$

with the solution

$$\mathbf{A}(t_n + \Delta t; \lambda) = \left(\mathbf{I} - \frac{\Delta t}{2}\mathbf{P}(q_{n+1})\right)^{-1}\left(\mathbf{I} + \frac{\Delta t}{2}\mathbf{P}(q_n)\right)\mathbf{A}(t_n; \lambda), \tag{C.5}$$

which yields

$$\mathbf{A}(t_0 + T; \lambda) = \prod_{n=0}^{N}\left(\mathbf{I} - \frac{\Delta t}{2}\mathbf{P}(q_{n+1})\right)^{-1}\left(\mathbf{I} + \frac{\Delta t}{2}\mathbf{P}(q_n)\right). \tag{C.6}$$

By using the approximation $\omega = e^{\pm i\Delta t\lambda} = 1 \pm i\Delta t\lambda$ in the definition of $\mathbf{P}$:

$$\mathbf{P}(q_n) = \frac{1}{\sqrt{1 - \Delta t^2|q(t_n,z)|^2}}\begin{bmatrix} \omega & -\Delta t q(t_n, z) \\ \Delta t q^*(t_i, z) & \omega^{-1} \end{bmatrix}, \tag{C.7}$$

it is possible to multiply $\mathbf{P}$ by ω and collect terms to utilise a fast polynomial arithmetic in which the monodromy matrix, $\mathbf{A}(t_0 + T; \lambda)$ is

$$\mathbf{A}(t_0 + T; \omega) = \frac{\mathbf{S}(\omega)}{\omega^N},$$

$$\mathbf{S}(\omega) = \prod_{i=0}^{N-1} \frac{1}{\sqrt{1 - \Delta t^2 |q(t_i, z)|^2}} \begin{bmatrix} \omega^2 & -\omega \Delta t q(t_i, z) \\ \omega \Delta t q^*(t_i, z) & 1 \end{bmatrix}, \qquad (\text{C.8})$$

for all ω. To find the auxiliary spectrum the zeros of $\mathbf{S}_{1,2}(\omega)$ and for the main spectrum the zeros of $\mathsf{Tr}\,\mathbf{S}(\omega) \pm 2\omega^N$ should be found with any appropriate algorithm. Here we find the eigenvalues of the companion matrix associated to these polynomials to this aim.

- **Spectral**: For a linear differential equation of Eq. (C.2) type where P is a periodic matrix with period T, the fundamental matrix has a special structure, $\mathbf{A}(t; \omega) = \hat{\mathbf{A}}(t; \omega)e^{Rt}$ where R is a constant matrix and $\hat{\mathbf{A}}(t; \omega) = \hat{\mathbf{A}}(t + T; \omega)$. Introducing the new eigenfunctions

$$\mathbf{A}_1(t; \omega) = e^{i\mu t}\hat{\mathbf{A}}_1(t; \omega), \qquad \mathbf{A}_2(t; \omega) = e^{-i\mu t}\hat{\mathbf{A}}_2(t; \omega), \qquad (\text{C.9})$$

where $\mu \in [0, \frac{2\pi}{T}]$, Eq. (C.2) turn into the following eigenvalue problem:

$$\begin{bmatrix} i(\partial_t - \mu) & -iq(t, z) \\ -iq^*(t, z) & -i(\partial_t - \mu) \end{bmatrix} \begin{bmatrix} \hat{\mathbf{A}}_1(t; \omega) \\ \hat{\mathbf{A}}_2(t; \omega) \end{bmatrix} = \lambda \begin{bmatrix} \hat{\mathbf{A}}_1(t; \omega) \\ \hat{\mathbf{A}}_2(t; \omega) \end{bmatrix}. \qquad (\text{C.10})$$

If solved for $\mu = 0$, periodic, and $\mu = \pi/T$, anti-periodic eigenfunctions, Eq. (C.10) gives the main spectrum of the signal. Since the signal is assumed to be periodic, substituting the periodic functions with their Fourier series:

$$\hat{\mathbf{A}}_1(t; \omega) = \sum_{n=-N}^{N} a_n^1 e^{inkt}, \quad \hat{\mathbf{A}}_2(t; \omega) = \sum_{n=-N}^{N} a_n^2 e^{inkt}, \quad q(t, z) = \sum_{n=-N}^{N} q_n^1 e^{inkt},$$

where $k = \frac{2\pi}{T}$ yields

$$\begin{bmatrix} -D & -iQ \\ -iQ^\dagger & D \end{bmatrix} \begin{bmatrix} A_1 \\ A_2 \end{bmatrix} = \lambda \begin{bmatrix} A_1 \\ A_2 \end{bmatrix}, \qquad (\text{C.11})$$
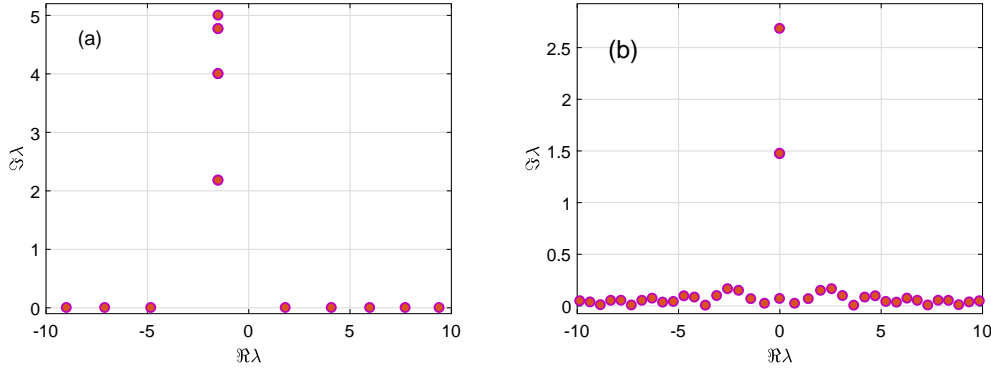
Fig. C.1 a) The main spectrum of a plane wave with $\mu = 3$ and $q_0 = 5$, and b) a rectangular pulse train with $T_1 = 2$, $A = 3$ and $T = 2\pi$.

with

$$D = k diag(-N, -N+1, \cdots, N-1, N) + \mu \mathbf{I}_{2N+1} \tag{C.12}$$

$$A_1 = \left[a_{-N}^1, a_{-N+1}^1, \cdots, a_{N-1}^1, a_N^1\right]^T, \quad A_2 = \left[a_{-N}^2, a_{-N+1}^2, \cdots, a_{N-1}^2, a_N^2\right]^T,$$

and Q is a matrix with $Q_{i,j} = q_{i-j}$ for $i + N > j$ and zero elsewhere.

These three algorithms are compared in terms of their accuracy and normalised time spent to calculate the main spectrum of a plane wave and a rectangular pulse train. The main spectrum of a plane wave, $q(t,z) = q_0 e^{i\mu t}$, is analytically known to a collection of the points:

$$\lambda_j^{\pm} = -\frac{\mu}{2} \pm i\sqrt{|q_0|^2 - \frac{j^2}{4}}. \tag{C.13}$$

The main spectrum for a plane wave with $\mu = 3$ and $q_0 = 5$ is shown in Fig. C.1a. The main spectrum of a rectangular pulse train with period T, amplitude A, and duty cycle of T_1/T is a collection of the zeros of $M_{rec}(\lambda) \pm 2$ where

$$M_{rec} = \begin{bmatrix} e^{-i\lambda(T-T_1)}\left(\cosh kT_1 + i\frac{kT_1}{k}\sinh kT_1\right) & \frac{AT_1}{k}\sinh kT_1 \\ \frac{A^*T_1}{k}\sinh kT_1 & e^{i\lambda(T-T_1)}\left(\cosh kT_1 - i\frac{kT_1}{k}\sinh kT_1\right) \end{bmatrix}$$

where $k^2 = -A^2 T_1^2 - \lambda^2$. An example of a main spectrum of a rectangular pulse train with $T_1 = 2$, $A = 3$ and $T = 2\pi$ is shown in Fig. C.1b. The numerical accuracy shown as the error between the theoretical main spectrum and the numerically calculated one and also the normalise runtime per sample is illustrated in Fig. C.2 for a plane wave and in Fig. C.3 for a rectangular pulse train. As can be seen from these figures, the accuracy of the layer-peeling algorithm is better than the other two. However, this performance highly
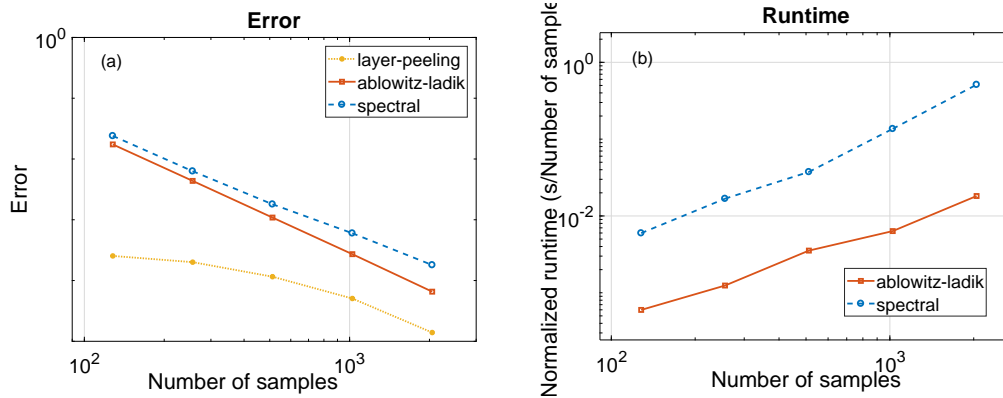
Fig. C.2 a) error in calculating the main spectrum of a plane wave using three algorithms; Ablowitz-Ladik, Spectral and layer-peeling, and b) the normalised runtime (per sample) for the Ablowitz-Ladik and Spectral methods.
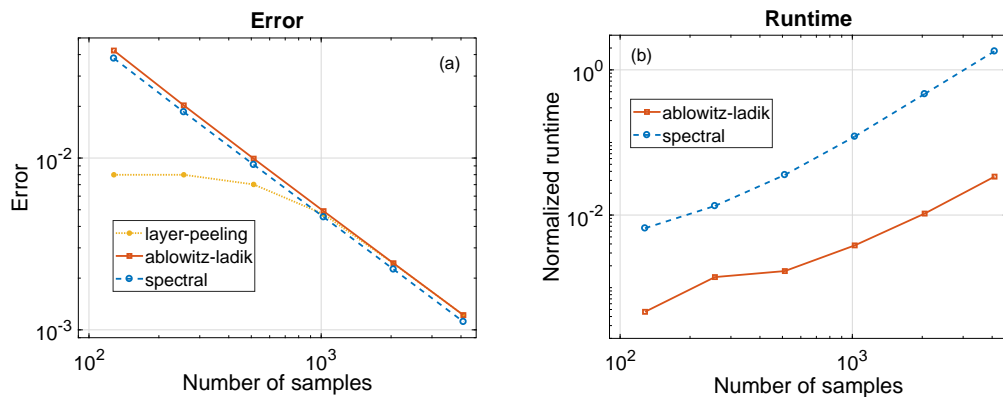

Fig. C.3 a) error in calculating the main spectrum of a rectangular pulse wave using three algorithms; Ablowitz-Ladik, Spectral and layer-peeling, and b) the normalised runtime (per sample) for the Ablowitz-Ladik and Spectral methods.

depends on other parameters such as the area of search for the roots of the functions which is the reason its runtime is not reported here. In general, the layer-peeling method is of the slowest numerical routines which, despite its superior accuracy, seems impractical to use in a real-time application such as a communication system. The spectral method renders good performance at the expense of huge required memory which is the main reason we have avoided it in our calculations. The Ablowitz-Ladik routine on the other hand, shows acceptable accuracy and small runtime and memory consumption, therefore, in all our calculations we use this routine.

Appendix D

A multi-soliton solution as an special case of a finite-gap one

Some particular decaying solutions of the NLSE can be constructed as a limit of a finite-gap solution. Here we describe how to choose the parameters of a finite-gap solution to arrive at a multi-soliton signal. We will also show how to make a multi-phase signal from this multi-soliton one, a signal which is suggested in subsection 3.4.2 to provide a two-dimensional constellation. Let assume that the discrete spectrum consists of $\mathcal{N}+1 = 5$ pairs of complex conjugate eigenvalues $\{E_j, E_j^*\}_{j=0}^{\mathcal{N}}$ (Fig. D.1)a. Take some value $\alpha > 0$ and put [44]

$$E_0 = -E_{\mathcal{N}}^* = -\alpha.$$

Now, let take the limit

$$E_{2j}, E_{2(j+1)} \to \lambda_j, \quad \text{for} \quad j = 1, \cdots, \mathcal{N}, \quad \text{where} \quad \lambda_m \neq \lambda_n \text{ if } n \neq m. \tag{D.1}$$

To have a solution to the focusing NLSE we want $\lambda_{2j-1} = \lambda_{2j}^*$ with $\Im \lambda_j > 0$ (see Fig. D.1b). So, $\mathcal{N}$ should be an even number. The resulted spectrum is shown in Fig. D.1b. Furthermore, by letting $\alpha \to 0$ the spectrum becomes a combination of $\mathcal{N}$ eigenvalues λ_j and $\mathbb{R}$. It is possible to show that $|q(t,z)| \to \alpha$ as $t \to \infty$ [44, Section 4.4]. Now we try to construct the associate solution to this spectrum in the algebro-geometric framework of Chapter 2. The hyperelliptic function (2.24) defining the Riemann surface is

$$\mu = \sqrt{\lambda^2 - \alpha^2} \prod_{j=1}^{\mathcal{N}} (\lambda - \lambda_j), \tag{D.2}$$

and the normalised Abelian differentials of Chapter 2 are

$$\omega_j = \frac{\sum_{k=1}^{\mathcal{N}} c_{jk} \lambda^{\mathcal{N}-k}}{\mu(\lambda)} d\lambda \tag{D.3}$$

where c_{jk} are the normalising factors according to the shown canonical cycles in Fig. D.1c, and can be found to be

$$c_{j1} = -\sqrt{\lambda_j^2 - \alpha^2} \equiv -i\kappa_j, \quad c_{j2} = -c_{j1}\sum_{k \neq j} \lambda_k.$$

In this way, the vectors $\mathbf{V}$ and $\mathbf{U}$ in (2.33) are

$$\mathbf{V}_j = -2i\kappa_j, \quad \mathbf{U}_j = -4i\kappa_j\lambda_j,$$

and the limiting values of the Abelian integrals of the second and third kind are obtained from

$$\Omega_1 = \pm\lambda \mp \alpha^2/2\lambda + o(1), \Omega_2 = \pm(2\lambda^2 - \alpha^2 + o(1)), \Omega_3 = \pm(\log\lambda - \log\alpha/2 + o(1)).$$

In this limit, the constants in (2.36) and (2.35) are $E = 0$, $N_0 = -2\alpha^2$ and $\omega_0 = \alpha^2/4$. The Riemann matrix, B, in (2.27) is calculated by

$$\mathsf{B}_{jk} = 2\log\frac{\gamma_k - \gamma_j}{\gamma_k + \gamma_j}, j > k, \quad \mathsf{B}_{jk} = \mathsf{B}_{kj}, j < k, \quad \text{where} \quad \gamma_j \equiv \frac{\sqrt{\lambda_j^2 - \alpha^2}}{\lambda_j + \alpha},$$

which conveniently approach the limiting values in which $\Re\mathsf{B}_{jj} \to -\infty, j = 1, \cdots, \mathcal{N}$. The last parameter to calculate is the vector $\mathbf{r}$ in (2.36) and (2.35):

$$\mathbf{r}_j = 2\int_{\alpha}^{\infty} \omega_j = -2\frac{\gamma_j - 1}{\gamma_j + 1}.$$

The divisor $\mathscr{D}$ is arbitrary (except for the invariance of them in respect to the branch points, E_j) and contains the auxiliary spectrum; we set it in the form of $\mathscr{D}_j = \frac{1}{2}\mathsf{B}_{jj} + 2\eta_j$. With
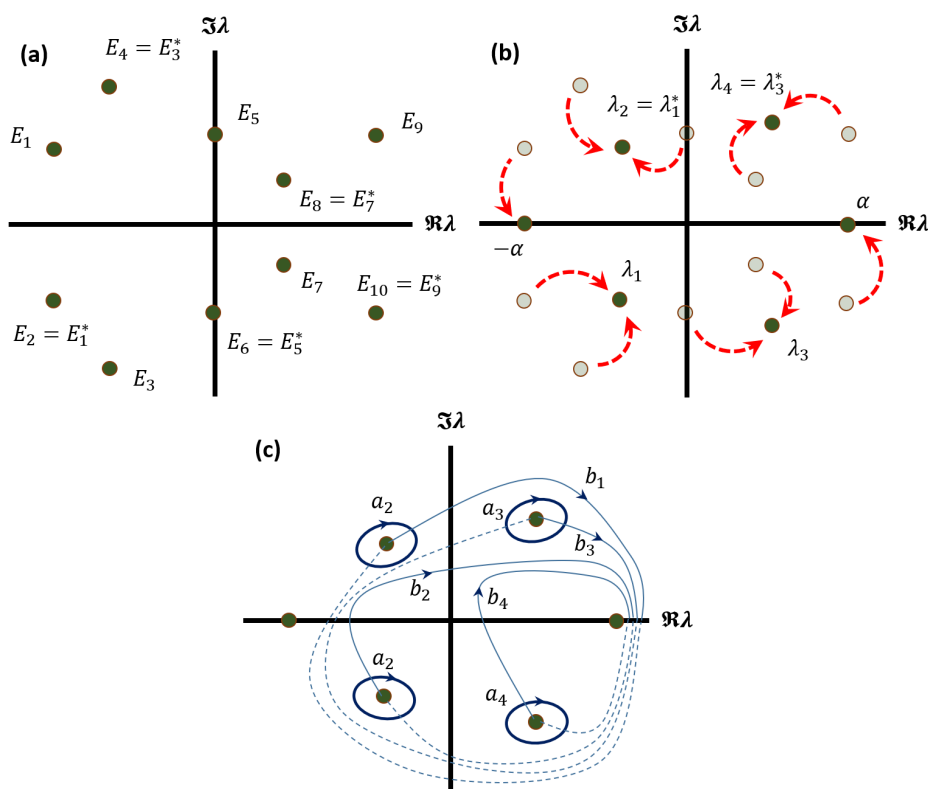
Fig. D.1 a) the main spectrum of a finite-gap solution, b) the result of the limit (D.1), and c) the a- and b-cycles on the new main spectrum.

these parameters in hand, one needs to construct the Riemann theta functions:

$$
\theta_\varsigma(t,z) = \theta\left(i\mathbf{V}t + i\mathbf{U}z - \mathscr{D} - \mathbf{K} + \varsigma\mathbf{r}\right) = \sum_{m_j=0,1} \exp\left\{ \sum_{j>k} \log\left(\frac{\gamma_j - \gamma_k}{\gamma_j + \gamma_k}\right)^{2m_j m_k} \right.
$$
$$
\left. + \sum_j m_j \left(2\kappa_j t + 4\kappa_j\lambda_j z + 2\varsigma \log\frac{\gamma_j - 1}{\gamma_j + 1}\right) - 2\eta_j \right\},
$$

$$\text{(D.4)}$$

where $\varsigma \in \{-1, 0, 1\}$. Then the solution is made through

$$
q(t,z) = A\frac{\theta_{-1}(t,z)}{\theta_0(t,z)} e^{-2i\alpha^2 z}.
\tag{D.5}
$$

A very simple family of smooth in t and z solutions can be made with the following conditions:

$$
\mathscr{N} > 1, \quad \alpha, \phi \in \mathbb{R}, \quad z_{0j}, t_{0j} \in \mathbb{R}, \quad \text{and} \quad 0 < \lambda_j < \alpha \quad \text{for} \quad j = 1, \cdots, \mathscr{N}, \quad \text{(D.6)}
$$

as an $\mathscr{N}$-phase solution:

$$
q_\mathscr{N}(t,z) = \alpha\frac{\theta_1(t,z)}{\theta_0(t,z)} e^{-2i\alpha^2 z - i\phi},
\tag{D.7}
$$

where

$$
\theta_\varsigma(t,z) = \sum_{m_v=0,1} \exp\left\{ \sum_{j>l} \log\left(\frac{\gamma_j - \gamma_l}{\gamma_j + \gamma_l}\right)^2 \left(m_j m_l + m_{\mathscr{N}+j} + m_{\mathscr{N}+l}\right) \right.
$$
$$
+ \sum_{j,l} \log\left(\frac{1 + \gamma_j\gamma_l}{1 - \gamma_j\gamma_l}\right)^2 m_{\mathscr{N}+j} m_l + 2\varsigma\sum_j \log\left(\frac{\gamma_j - 1}{\gamma_j + 1}\right)\left(m_j - m_{\mathscr{N}+j}\right)
$$
$$
- 2\sum_j \eta_j^0 \left(m_j + m_{\mathscr{N}+j}\right) + 2\sum_j \delta_j(z - z_{j0})\left(m_j - m_{\mathscr{N}+j}\right)
$$
$$
\left. + 2i\sum_j \kappa_j(t - t_{0j})\left(m_j + m_{\mathscr{N}+j}\right) \right\},
$$

and where

$$
\kappa_j = \sqrt{\alpha^2 - \lambda_j^2}, \quad \delta_j = 2\lambda_j\sqrt{\alpha^2 - \lambda_j^2}, \quad \gamma_j = i\frac{\kappa_j}{\lambda_j + \alpha},
$$
$$
\eta_j^0 = \frac{1}{2}\sum_{l=1}^{\mathscr{N}} \log\frac{\gamma_j - \gamma_l}{\gamma_j + \gamma_l} + \frac{1}{2}\sum_{l=1}^{\mathscr{N}} \log\frac{1 + \gamma_j\gamma_l}{1 - \gamma_j\gamma_l},
$$

for $\varsigma = 0, 1$. In fact, $q_{\mathcal{N}}(t, z)$ belongs to a family of almost periodic solutions with $3\mathcal{N} + 2$ parameters with the period

$$T = lcm(\frac{\pi}{\kappa_j}).$$

Under the condition

$$\max_{j} \delta_j < 2 \min_{j} \delta_j = 2\delta_0, \tag{D.8}$$

the solution at $z \to \infty$ tends to

$$q_{\mathcal{N}}(t, z) = \alpha \left[1 + \sum_{j=1}^{\mathcal{N}} A_j \cos 2\kappa_j(t - t_{0j}) \exp\left(-2\delta_j z - i\alpha_j\right) + O(\exp(-4\delta_0 z)) \right]$$
$$\times \exp(2i\alpha^2 z - i\phi + i\phi^0),$$

where

$$A_j = -4\frac{\kappa_j}{\alpha} e^{2\delta_j z_{0j}} \prod_{l=1}^{\mathcal{N}} \frac{1 + \gamma_j \gamma_l}{1 - \gamma_j \gamma_l} \prod_{l \neq j} \frac{\gamma_j + \gamma_l}{\gamma_j - \gamma_l}, \quad \alpha_j = \tan^{-1} \frac{\lambda_j}{\kappa_j}, \quad \phi^0 = -2 \sum_{j=1}^{\mathcal{N}} \tan^{-1} \frac{\kappa_j}{\lambda_j}. \tag{D.9}$$

The communication system proposed in Subsection 3.4.2 is, in fact, a close example to this family of solutions when $\mathcal{N} = 1$ and its limited performance has to do with the constraint (D.8) which makes the size of the constellation small. This confined constellation, in turn, leads to limited bandwidths, limited signal powers, and small minimum distance in the constellation.